

Modelling Anomalous Weather Conditions over the Himalaya

by

Ujjwal Tiwari

A thesis submitted in partial fulfillment of the requirements for the degree of

Master of Science

Department of Earth and Atmospheric Sciences

University of Alberta

© Ujjwal Tiwari, 2019

Abstract

The Himalayan weather system is under the influence of both tropical and extratropical factors, and interactions between those factors can result in extreme weather-related disasters. However, due to an existing knowledge gap about the factors contributing to anomalous weather conditions over the Himalaya and very limited resources for weather forecasting, extreme weather prediction over the world's most extreme topography is very challenging. In this thesis, I used the combination of observations, reanalysis data, and mesoscale atmospheric model output to understand the influence of upper-tropospheric atmospheric blocks on anomalous weather conditions over the Himalaya. Furthermore, I evaluated the performance of various cloud-microphysics parameterization schemes and forcing data in the mesoscale atmospheric model to predict extreme precipitation events over the Himalaya. My results suggest that Ural-Siberian blocks are important perturbations to Himalayan weather and are associated with anomalous precipitation. The freezing level drops/rises depending on anomalous cold/warm advection triggered by the block, and this determines the type of precipitation (rain or snow) at different regions.

Sensitivity tests of different cloud microphysics schemes and initial conditions with the WRF mesoscale atmospheric model, which was used to simulate an extreme flood-producing precipitation event on August 2017 over Nepal, showed that the coarse resolution (15 km) simulation with the WRF Single Moment Class 6 (WSM6) scheme forced with ERA-Interim data performed the best, but at high-resolution (3 km) the WRF Double Moment Class 6 (WDM6) scheme forced with ERA-Interim data was closest to observations. The overall performance of coarse resolution simulations was found to be better than the high-resolution simulations that had the cumulus scheme turned off. To further understand the effectiveness of the cumulus parameterization below 5 km resolution, I performed two experiments at 3 km horizontal resolution using the WSM6 and WDM6 microphysics schemes forced with ERA-Interim data. There was an overall improvement in simulated precipitation with the WDM6 microphysics scheme when the cumulus parameterization was on. Thus, my result suggests the importance of keeping the cumulus parameterization on over regions that have steep topographic relief to accurately simulate the quantity of precipitation for such flood-producing events.

Preface

I was responsible for model simulation, data analysis and manuscript preparation. ABG Bush provided computational resources, constructive comments, suggestions and manuscript edits.

Dedication

“The woods are lovely, dark and deep. But I have promises to keep, and miles to go before I sleep.”

Robert Frost

To my mother, wife and son

Acknowledgments

I am grateful to my M.Sc. supervisor Dr. Andrew Bush for his continuous support and guidance throughout my graduate studies. He allowed me to choose the research topic on my own. So, I decided to study anomalous weather events over the Himalaya using both the observations and numerical modeling. He also accepted to be my Ph.D. supervisor, and I am very excited about the coming years. I also acknowledge my graduate committee members (Prof. Paul Myers and Prof. Martin Sharp) and the examination chair (Prof. Gerhard Reuter) for their valuable comments and feedback. Those comments and suggestions helped to improve the quality of this thesis.

I thank Dr. Laura Castro and Dr. Charlene Feucher for their suggestions during thesis formatting and article preparation. They have always been mine, good friends. I also thank friends and colleagues from the Fluid Lab.

My family has always been a great source of inspiration. My mom always wanted me to get a higher education, though she never went to school. My wife, Suprabha, always supported me in every decision we made and stood with me in every difficult situation of life. My son, Utkars, was born last year, and his presence has provided additional motivations and joy in my life.

Contents

1	Introduction	1
1.1	The Hindu Kush Himalaya - From a Climate Change Perspective	1
1.2	Drivers of Himalayan Climate	2
1.2.1	Monsoon	3
1.2.2	Westerly Disturbance	5
1.3	Cause of Extreme Weather Events Over the Himalaya	5
1.4	Modeling Himalayan Weather	6
1.5	Motivation and Objectives	7
2	A Relationship between Ural-Siberian Blocking and Himalayan Weather Anomalies	14
2.1	Abstract	14
2.2	Introduction	15
2.3	Materials and Methods	16
2.3.1	Data	16
2.3.2	Methods	17
2.3.3	Regional modeling of atmospheric conditions over the Himalaya during the blocking events	17
2.4	Results	19
2.4.1	Blocking frequency from ERA-Interim data	19
2.4.2	Case I: Blocking event (9-17 May 2014)	19
2.4.3	Case II: Blocking event (February 1 to February 11, 2012)	28
2.5	Discussion and Conclusion	36
2.5.1	Discussion	36
2.5.2	Conclusion	38
2.6	Acknowledgments	39

3	Sensitivity Tests of Microphysics Schemes in WRF: A Case Study of a Flood-Producing Precipitation Event over Nepal	44
3.1	Abstract	44
3.2	Introduction	45
3.3	Materials and Methods	46
3.3.1	Description of the event	46
3.3.2	Data	47
3.3.3	Model description	48
3.3.4	Description of WRF microphysics schemes	48
3.3.5	Evaluation of model output	50
3.4	Results	52
3.4.1	Sensitivity analysis	52
3.4.2	Influence of cumulus parameterization on high-resolution simulation	55
3.4.3	Convection during the event	58
3.4.4	Moisture flux	58
3.5	Discussion	59
3.6	Conclusions	61
4	Conclusions	73
4.1	Key findings and future research	73
4.1.1	Coarse resolution simulations with WSM6 and WDM6 microphysics schemes perform better than high resolution simulations	73
4.1.2	Cumulus parametrization is essential for highly convective systems over the Himalaya	74
4.1.3	Ural-Siberian blocks generate Himalayan climate anomalies	74
4.1.4	Differential temperature advection during blocking events determines the type of precipitation at the surface	75
4.2	Thesis Summary	75
	Bibliography	77

List of Tables

2.1	WRF model configuration	19
3.1	WRF model configuration	49
3.2	Best performing simulations over different regions (R1, R2, R3) and domains (D1, D2)	55

List of Figures

1.1	Spatial distribution of precipitation over the HKH and south/south-east Asia during summer (June, July, August, September (JJAS), left panel) and winter (December, January, February (DJF), right panel). Source: APHRODITE data, (Yatagai et al., 2012)	3
2.1	The WRF model domains. (a) The outer domain (D1) with 18Km horizontal grid spacing; the red rectangle shows the location of the inner domain (D2) and (b) the inner domain (D2) with 6 Km horizontal grid spacing. WHN and EHN in D2 refer to Western Himalayan Notch (WHN) and Eastern Himalayan Notch (EHN) respectively. Shading in both (a) and (b) indicates modeled elevation above sea level (m, asl).	18
2.2	(a) Average blocking frequency from 1985 to 2015 over 45 ⁰ E to 75 ⁰ E according to the season, and (b) number of blocking events per year from 1985 to 2015 centered between 55 ⁰ E and 70 ⁰ E.	20
2.3	Daily 200 hPa geopotential height anomalies (shaded, m), geopotential height (contour, hectometer) and anomalous horizontal wind (vector, m/s) on (a) May 10, (b) May 11, (c) May 12, and (d) May 13 2014 (Source: ERA-Interim reanalysis).	21
2.4	Daily mean sea level pressure anomalies (shaded, hPa), 850 hPa geopotential height (black contour, m), and 850 hPa anomalous wind (vector, m/s) on (a) May 10, (b) May 11, (c) May 12, and (d) May 13, 2014 (Source: ERA-Interim reanalysis).	22
2.5	Daily PV (PVU) on 350 K isentropic surface on (a) May 11, (b) May 12, 2014. $PV \geq 1$ PVU are contoured (Source: ERA-Interim reanalysis); vertical cross section of daily simulated PV (shaded) and potential temperature (θ , green contour) on (c) May 11, 00:00Z and (d) May 12, 18:00Z along 70 ⁰ E longitude (c and d are plotted from WRF simulations).	23
2.6	(a) WRF rainfall, (b) WRF snowfall, and (c) TRMM precipitation accumulated over 9 - 17 May 2014; (d) MODIS snow cover difference between May 16 and May 9.	24

2.7	(a), (b), (c), (d), and (e) daily accumulated precipitation (shaded, mm), 500 hPa geopotential height (contour, hectometer), 700 hPa wind (vector, m/s) from WRF simulations; (f), (g), (h), (i), and (j) precipitable water (shaded, mm), vertically integrated moisture flux (vector indicating direction and contour indicating magnitude, $\text{kgm}^{-1}\text{s}^{-1}$) computed from WRF simulations, and; (k), (l), (m), (n) and (o) ERA-Interim surface evaporation (m of water) for May 10, 11, 12, 14, and 14 respectively.	26
2.8	700 hPa average temperature advection ($^{\circ}\text{C}/\text{h}$), geopotential height (m), and wind (barbs, full barb = 10m/s) for (a) May 11 and (b) May 12 (Source: WRF simulations).	27
2.9	Skew-T log-P diagram for Shreenagar station on (a) 00Z May 12, 2014 and (b) 00Z May 13, 2014 (Source: University of Wyoming).	27
2.10	Skew-T log-P diagram for Dibrugarh station on (a) 00Z May 12, 2014 and (b) 00Z May 13, 2014 (Source: University of Wyoming).	28
2.11	Cross section of daily accumulated precipitation (rain, snow and mixed precipitation), average freezing level and elevation along the red lines ((a) CRS1 and (b) CRS2) shown in Fig. 2.8b on May 12, 2014 (Source: WRF simulations).	29
2.12	Daily 200 hPa geopotential height anomalies (shaded, m), geopotential height (contour, hectometer) and anomalous horizontal wind (vector, m/s) on (a) Feb 03, (b) Feb 04, (c) Feb 05, (d) Feb 06, (e) Feb 07, and (f) Feb 08, 2012 (Source: ERA-Interim reanalysis).	30
2.13	Daily mean sea level pressure anomalies (shaded, hPa), 850 hPa geopotential height (contour, m) and 850 hPa anomalous wind (vector, m/s) on (a) February 03, (b) February 04, (c) February 05, (d) February 06, (e) February 07, and (f) February 08, 2012 (Source: ERA-Interim reanalysis).	31
2.14	Daily PV (PVU) on 350 K isentropic surface on (a) February 04, (b) February 07, (c) February 08, 2012, $\text{PV} \geq 1$ PVU are contoured (Source: ERA-Interim reanalysis); vertical cross section of simulated PV (shaded) and potential temperature (θ , green contour) on (d) February 04, 12:00Z, (e) February 07, 18:00Z, and (f) February 08, 12:00Z, (d and e across 700E longitude, and f across 800E longitude, d, e, f are plotted from WRF simulations).	32
2.15	(a) WRF rainfall, (b) WRF snowfall, and (c) TRMM precipitation accumulated over 1-9 February 2012; (d) MODIS snow cover difference between February 10 and February 1. Location of Srinagar upper air station is represented by a black star enclosed within a black circle in (b).	33

2.16	(a), (b), (c), (d), and (e) daily accumulated precipitation (shaded, mm), 500 hPa geopotential height (contour, hectometer), 700 hPa wind (vector, m/s) from WRF simulations; (f), (g), (h), (i), and (j) precipitable water (shaded, mm), vertically integrated moisture flux (vector indicating direction and contour indicating magnitude, $\text{kgm}^{-1}\text{s}^{-1}$) computed from WRF simulations, and (k), (l), (m), (n) and (o) ERA-Interim surface evaporation (m of water) for February 4, 5, 6, 7, and 8 respectively.	34
2.17	700 hPa average temperature advection ($^{\circ}\text{C/h}$), geopotential height (m), and wind (barbs, full barb = 10m/s) for (a) February 7 and (b) February 8 (Source: WRF simulations).	35
2.18	Skew-T log-P diagram for (a) Shreenagar station 03Z Feb 03, 2012 (observations obtained from the University of Wyoming), (b) Gorakhpur station 00Z Feb 08, 2012 (Source: University of Wyoming).	36
2.19	Cross section of daily accumulated precipitation (rain, snow and mixed precipitation), average freezing level and elevation along the red lines ((a) CRS 3, February 4, 2012 and (b) CRS 4, February 8, 2012) shown in Fig. 2.17b (Source: WRF simulations).	37
3.1	Synoptic atmospheric conditions during the flooding event. (a) sea level pressure (hPa, shaded) and 850 hPa wind (m/s, vector), (b) 500 hPa geopotential height (m, shaded) and 500 hPa wind (m/s, vector), and (c) 200 hPa geopotential height (m, shaded) and 200 hPa wind (m/s, vector).	47
3.2	Total accumulated precipitation from 11-16 August 2017. (a) Station observations, and (b) Global Precipitation Measurement (GPM) precipitation data	47
3.3	WRF domains (a) Outer domain (D1, 15km) and (b) Inner domain(D2, 3km). Topography is shaded in both domains.	49
3.4	WRF simulated precipitation over D1 using (a) Goddard, (b) Lin, (c) Milbrandt, (d) Morrison, (e) Thompson, (f) WDM6 and (g) WSM6 schemes forced with NCEP data; (h) Goddard, (i) Lin, (j) Milbrandt, (k) Morrison, (l) Thompson, (m) WDM6, and (n) WSM6 schemes forced with ERA-Interim data; (o) station observation and (p) GPM data. All plots are accumulated precipitation over 11-16 August, 2017.	53
3.5	Same as Fig. 3.4, but for D2	54
3.6	Comparison of the intensities of simulated precipitation with the observations.	54
3.7	Comparison of the intensities of D1 simulations with the observations. (a) Over R1, (b) over R2, and (c) over R3. X and y axes represent standard deviation, blue arc represents correlation coefficient and purple arcs within plots represent centered root mean square deviation/error.	56
3.8	Same as Fig.3.7 but for D2 simulations	57

3.9	Comparison of precipitation intensities between the WDM6-ERA D2 simulation with cumulus scheme on and the observations over R1 and R2.	57
3.10	Skew-T diagram at 00Z, 11 August 2017, (a) Observation taken from Patna station, (b) WDM6 D2 with cumulus parameterization, and (c) WSM6 D1.	58
3.11	Skew-T diagram at 06Z, 11 August 2017, (a) WDM6 D2 with cumulus parameterization, and (b) WSM6 D1.	59
3.12	Average simulated VIMF from the surface to 700 hPa (vector and contour, $\text{kgm}^{-1}\text{s}^{-1}$) and precipitable water (shaded, mm) over 11-16 August using various microphysics options and ERA-Interim forcing.	60

Chapter 1

Introduction

1.1 The Hindu Kush Himalaya - From a Climate Change Perspective

The Hindu Kush Himalaya (HKH) is one of the largest areas containing permanently snow/ice covered areas outside the Polar regions (including Greenland), with an estimated 54,000 glaciers covering an area of $\sim 60,000$ km² (Maharjan et al., 2018). Due to its extremely elevated topography, the HKH controls atmospheric flows around it, thereby affecting the climate of much of the Asian continent. Two main drivers of weather around the HKH are the monsoon system and the westerly disturbances during summer and winter, respectively. Together they control almost the entire hydrological budget over the Himalayan region. According to Bookhagen and Burbank (2010), all the catchments east of the Sutluj River in the western Himalaya receive 70% of their total annual precipitation during the summer monsoon.

The impacts of climate change in the HKH region are noticeable. Surface temperature over the HKH region shows an increasing trend. Although the increasing trend is not uniform throughout the HKH region (Ren et al. (2017); Singh et al. (2015)), the average rate of temperature increase over the HKH region over the past century has been $+0.104^{\circ}\text{C}/\text{decade}$, with a rate increase that is consistent with the global trend (Wester et al., 2019). Climate change studies over the KHK project an overall temperature warming over the 21st century: climatic projections over the Himalaya using CMIP5 products indicate that, for the Representative Concentration Pathway (RCP) 4.5 and RCP 8.5 scenarios the temperature over the Himalaya is projected to increase by $2.5 \pm 1.5^{\circ}\text{C}$ and $5.5 \pm 1.5^{\circ}\text{C}$ respectively, over the 21st century (van et al., 2011). Furthermore, according to Wester et al. (2019), the overall warming over the northwestern Himalaya and Karakoram will be comparatively higher than over the central and eastern Himalaya, and the Tibetan Plateau.

There are higher uncertainties concerning the precipitation response to climate change over the HKH (Choudhary and Dimri, 2018; Hasson et al., 2013, 2016; Mishra, 2015; Wester et al., 2019). Recent studies indicate

a large interannual variability in precipitation with frequent intense precipitation events (Guhathakurta et al., 2011; Singh et al., 2014; Vellore et al., 2016). These intense precipitation events produce catastrophic disasters in the Himalayan region (e.g. north Pakistan flooding in 2010, north India flooding in 2013, western Nepal flooding in 2014). The projected future change in precipitation patterns over the HKH region is also uncertain. Results of the Coordinated Regional Climate Downscaling Experiment (CORDEX) Regional Climate Models (RCM) indicate that precipitation over the HKH is likely to increase by 4 - 12% and 4 - 25% in the near and long-term respectively; however, the magnitude of precipitation change will vary according to location and season (Wester et al., 2019). One of the critical issues highlighted by Wester et al. (2019) is that the western part of the HKH is projected to be drier, while the Tibetan region is projected to be wetter in the future. In addition, the frequency of intense precipitation events and associated disasters in the HKH is likely to increase in the future (IPCC, 2012).

The cryosphere of the HKH is responding to climate change in an adverse way. Himalayan glaciers are retreating at an unprecedented rate due to surface temperature rise (Wester et al., 2019). Although direct measurements of annual glacier mass balance over the Himalaya are relatively limited, most areas in the Himalaya have experienced glacier retreat in recent years (Bolch et al., 2012). According to Wester et al. (2019), after 2000, the eastern and western Himalaya have experienced the highest rate of mass loss (-0.6 m w.e./yr), the central Himalaya (-0.4 m w.e./yr) and the Hindu Kush (-0.3 m w.e./yr) have experienced moderate mass loss and the Karakoram glaciers have experienced either little change or slight mass gain. These results apply to both clean ice and debris-covered glaciers (Shea et al., 2015; Thompson et al., 2016; Vincent et al., 2016).

A detailed study of the impact of climate change on Himalayan river run-off is lacking and the limited number of cursory studies project an overall increase in the river discharge until mid-century and a gradual decrease thereafter (Immerzeel et al., 2013; Wester et al., 2019). Furthermore, there are projected to be strong seasonal changes in flow volumes, with increased flow volumes projected for the monsoon and post-monsoon seasons and reduced flow volumes projected for the winter and pre-monsoon seasons (Bharati et al., 2014). These projected changes in Himalayan river flow would have a direct impact on regional ecosystems and human societies that rely heavily on fresh water resources of the HKH.

1.2 Drivers of Himalayan Climate

The atmospheric flow around the Himalaya during the winter and spring months is dominated by the westerly winds with an observed descending motion (caused by the mechanical influence of the Tibetan Plateau) along the foothills of the Himalaya over Northern India and Nepal (Sato and Kimura, 2007). This downward motion weakens during summer, as the Jet-stream winds shift north and the low-level monsoon winds progress north-

ward towards the Himalayan foothills, where they are then subject to mechanically forced convection by the Himalayan topography, producing intense precipitation (Park et al., 2012; Sato and Kimura, 2007).

Winter precipitation over the Himalaya is attributed to westerly disturbances. Westerly disturbances are low pressure systems with high moisture content that form in the upper atmosphere but produce local frontal systems near the surface (Dimri and Niyogi, 2013; Dimri et al., 2015). The westerly disturbances carry moisture from distant sources such as the Mediterranean, Black, and Caspian Seas (Dimri et al., 2015). Despite precipitation from the summer monsoon, the western Himalaya receives most of its rainfall during the winter months (Fig. 1.1).

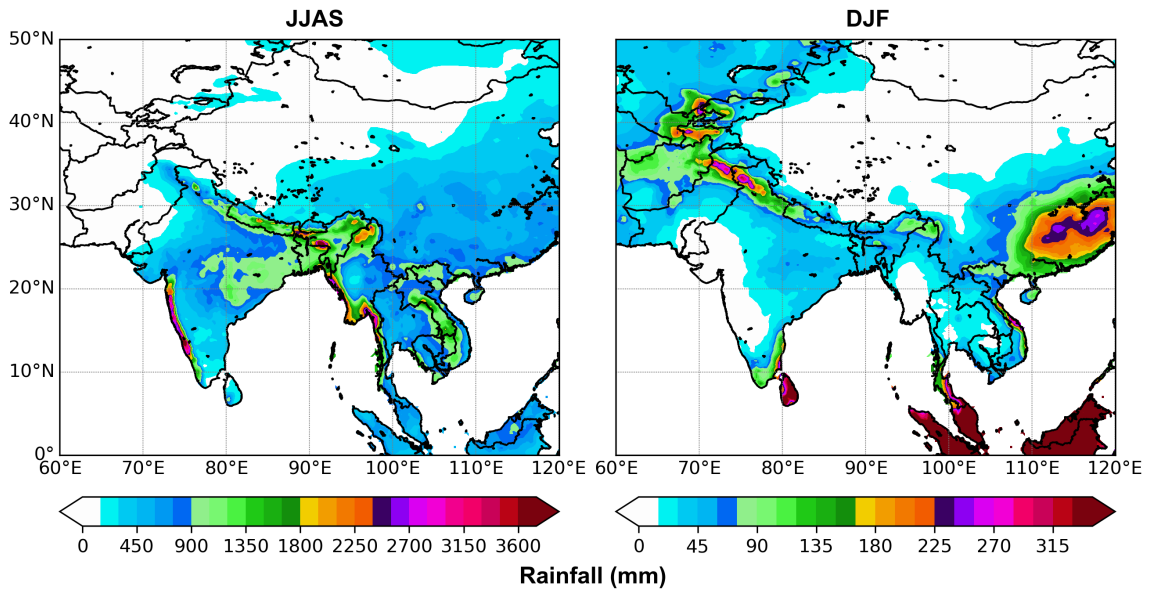


Figure 1.1. Spatial distribution of precipitation over the HKH and south/south-east Asia during summer (June, July, August, September (JJAS), left panel) and winter (December, January, February (DJF), right panel). Source: APHRODITE data, (Yatagai et al., 2012)

The summer monsoon (referred to simply as the monsoon hereafter) and westerly disturbances are discussed in detail in the following subsection.

1.2.1 Monsoon

The monsoon is a significant driver of Himalayan hydrology. Over the central Himalaya, the monsoon contributes to more than 80% of the total annual precipitation, although this number varies spatially from east to west (Bookhagen and Burbank, 2010). The monsoon trough and the monsoon depressions are the main climatological features of the South Asian monsoon. The monsoon trough is a portion of the Intertropical Convergence Zone which shifts northward over South Asia during the summer season. When the monsoon trough is parallel to the Himalayan foothills, it draws a southerly moist flow from the Arabian Sea and the Bay of Bengal and

produces intense precipitation. Monsoon depressions are transient synoptic-scale cyclones that originate over the Bay of Bengal and travel north-westward along the monsoon trough. On average, 3-6 monsoon depressions develop over the Bay of Bengal every summer and each of them last for 4-5 days and produce intense precipitation along their paths (Hunt et al., 2016; Rajeevan et al., 2000).

The summer monsoon usually begins around early June over the eastern Himalaya and typically lasts for more than 4 months, with a retreat from northwest India around mid October (Prasad and Hayashi, 2005). Over the HKH, there are strong spatial and diurnal variations in the amount of precipitation received. The Tibetan Plateau gets rainfall during the afternoon to evening hours, while the Karakoram and south facing slopes get rainfall during the midnight to morning hours (Bhatt and Nakamura, 2005). Likewise, regions north of the Bay of Bengal receive rainfall during the late morning. Furthermore, there is a strong ridge-valley gradient in the intensity of rainfall. Karki et al. (2017) used a numerical model to simulate the atmospheric fields over eastern Nepal for a complete hydrological year and found the ridges and lowlands receive precipitation during the midnight and early hours, while the south facing slopes receive precipitation during the morning hours, which is consistent with the observations.

Convection is one of the important mechanisms for generating intense precipitation over the Himalayan region (Barros and Lang, 2003; Houze Jr. et al., 2007; Shrestha et al., 2015). There is, however, a distinct variation in the type of convection between the western and eastern Himalaya. In particular, convective systems in the western region display strong convective radar echos compared to other regions in the HKH (Medina et al., 2010). Furthermore, according to Medina et al. (2010), the moist low-level flow from the Arabian Sea gains additional sensible heat while traversing over desert land which enhances buoyancy of the air parcel. Thus, the flow that reaches the western Himalayan foothills has high levels of potential instability, and this flow is also capped by a thick layer of dry and warm air aloft coming from the Tibetan Plateau. Once the potentially unstable flow is mechanically lifted by Himalayan peaks, it releases its instability with strong convection and hence intense precipitation.

Conversely, over the eastern Himalaya, convective systems are characterized by broad stratiform radar echoes. These systems are associated with monsoon depressions traveling towards the north-west. According to Medina et al. (2010), the conditionally unstable low-level moist flow reaches the Himalayan foothills and is lifted orographically and releases the instability in the form of narrow-vertical convective cells. These cells merge with each other creating a cold-pool that travels along the Himalayan slopes. As these cells age they spread over a wide area with a broad stratiform signature.

The topography of the central Himalaya is quite unique compared to that of the western and eastern Himalaya. Instead of a consistent rise in elevation like in the western and eastern Himalaya, the central Himalaya consists of a two-tiered topography. The first is the sub-Himalaya (~500 - 700 m above sea level (asl)), and

second tier is a Lesser-Himalaya ($\sim 2,000 - 2,2000$ m asl). Due to this two-tiered topography over the Nepal Himalaya, two peaks of rainfall are observed (Shrestha et al., 2012). The mechanism of precipitation over the Sub-Himalaya is highly convective, while that over the Lesser-Himalaya is broadly stratiform in nature.

1.2.2 Westerly Disturbance

Westerly disturbances (WDs) bring precipitation over the HKH during winter and early spring. The western Himalaya and the Karakoram receive more than half of their total annual precipitation from WDs (Dimri and Mohanty, 2009; Lang and Barros, 2004). In addition, the higher elevations (> 3000 m asl) in the central Himalaya receive more than one third of their annual precipitation during the winter season in the form of snowfall from the WDs (Lang and Barros, 2004). WDs are baroclinic systems Holton (1992); Hunt et al. (2018) arising from the instability of the subtropical Jet stream (Dimri et al., 2015; Hunt et al., 2018). They originate most commonly over the Mediterranean region and grow in amplitude as they travel eastward (Hunt et al., 2018). Although similar in origin, WDs are somewhat different than extratropical cyclones, as they are smaller in extent and develop within the subtropical westerly wind system (Bader et al., 1995). The development of WDs are highly dependent on the presence of the subtropical Jet, regardless of the season, but their impact is quite pronounced during the more baroclinic winter season (Hunt et al., 2018).

1.3 Cause of Extreme Weather Events Over the Himalaya

Extreme precipitation events over the Himalaya during both the summer and winter seasons are the result of interactions between low-level subtropical atmospheric circulations and upper-level extratropical circulations. For example, the 2010 Pakistan flooding and 2013 north India flooding were caused by the interactions between low-level south-westerly monsoon flows and upper-level extratropical circulation anomalies (Hunt et al., 2018; Lau and Kim, 2012; Vellore et al., 2016). Those extreme events were caused by the combination of a southward shift of upper-level extratropical troughs, ridges of high pressure over eastern Siberia and intense Tibetan anti-cyclones; this combination created anomalously low pressures over the foothills of the western Himalaya and brought moisture from both the Bay of Bengal and the Arabian Sea, resulting in intense precipitation (Vellore et al., 2016). Likewise, extreme precipitation events over the western Himalaya during winter are also related to intensification of the Siberian high and its associated southerly wind anomalies (Hunt et al., 2018). These studies indicate that the sub-tropical response to anomalous upper-atmospheric structures from the midlatitudes can produce extreme weather conditions over the HKH.

There is a teleconnection between interannual variability of Himalayan climate and global atmospheric-oceanic oscillations. The teleconnection between the El Niño Southern Oscillation (ENSO) and precipitation

over the HKH is well established (Annamalai et al., 2007; Fan et al., 2017; Jang and Straus, 2012; Joshi and Kar, 2018; Mooley, 1983). In particular, the positive phase of ENSO (El Niño) is related to below normal rainfall over the HKH, while the negative phase (La Niña) is related to above normal rainfall over the HKH. ENSO not only affects the overall intensity and distribution of precipitation, it can also facilitate the occurrence of extreme events. For example, the 2010 north Pakistan flooding event coincided with the occurrence of a strong La Niña in the Pacific (Mujumdar et al., 2012).

1.4 Modeling Himalayan Weather

Due to the extreme topography and distinctly varying weather patterns over small spatial scales, existing weather stations are sparsely located and are not sufficient to adequately study the anomalous weather conditions over the Himalaya (Revadekar et al., 2013). Furthermore, most of the existing weather stations are located at relatively low altitude, so they are not suitable to study high altitude weather events. Alternative methods with which to study high-mountain weather events make use of reanalysis and satellite data products (e.g. Andermann et al. (2011); Bhatt and Nakamura (2005); Shrestha et al. (2015); Xie et al. (2007)). However, the horizontal resolutions of those products are not sufficient to study weather phenomena at a regional or a basin scale.

Mesoscale atmospheric models (MAMs) are better alternatives to generate high-resolution atmospheric fields to study anomalous weather events over the HKH. They dynamically downscale the coarse resolution atmospheric fields from the reanalysis products or general circulation model (GCM) simulations to produce higher resolution output suitable to study mesoscale weather events. These MAMs require a large amount of computational resources, which limit them in terms of simulation duration and/or spatial resolution. Norris et al. (2019) used the Weather Research and Forecasting (WRF) model to downscale the climate of the Himalaya at what was deemed to be a convection permitting grid scale of 6.7 km for three decades, which is among the limited examples of the use of a MAM over a multi-decadal timescale over the HKH. Conversely, the highest spatial resolution in a MAM simulation done to date for the HKH is 500 m over the Langtang catchment in the central Himalaya for 10-day periods during the summer and winter of 2014 (Bonekamp et al., 2018).

In the majority of cases, MAMs are used to study the mesoscale features of extreme weather events and to conduct sensitivity tests of various physical and dynamical schemes to come up with the ideal combination of parametrizations for a given area during a given season (e.g. Chawla et al. (2018); Karki et al. (2017); Orr et al. (2017); Patil and Pradeep Kumar (2016)). Interestingly, every extreme event is unique and a single set of schemes does not necessarily work for other events. This highlights the importance of improving physical parametrizations in MAMs to accurately simulate Himalayan weather.

Furthermore, the ability of MAMs to resolve Himalayan topography is also important for producing realis-

tic simulations. Karki et al. (2017) used the WRF model to simulate the atmospheric variables over the central Himalaya using different resolutions of topographic data and found that use of the high-resolution topography made simulation of the key features of monsoon precipitation more realistic. Moreover, Bonekamp et al. (2018) highlighted the importance of the spatial resolution of the land use data and spin-up time to simulate the precipitation characteristics in the HKH. These studies emphasize the importance of boundary conditions on the quality of simulations in the HKH.

Furthermore, the study of physical parameterizations in MAMs indicate that the cloud microphysics scheme controls the spatial pattern and type of precipitation, while the planetary boundary layer and cumulus schemes control the magnitude of precipitation (Chawla et al., 2018).

Apart from the applications of MAMs presented in the previous paragraphs, output from MAMs is used to provide initial conditions to force glacier and hydrological models. Collier et al. (2013) and Collier and Immerzeel (2015) coupled the WRF model with a glacier mass balance model and simulated the atmospheric fields over the Karakoram and the Langtang basin in the central Himalaya, respectively, over a hydrological year. Their results showed an overall improvement in the simulated atmospheric fields when the atmosphere-glacier models are run in coupled mode, which allows the atmosphere to respond to the changing glacier conditions.

1.5 Motivation and Objectives

The uncertainty associated with weather prediction over the Himalayan region and the existing knowledge gap about factors contributing towards extreme events were the motivations behind this research. Extreme weather events over the Himalaya have been associated with the interaction between the extratropical and subtropical forcing. Extreme flooding in northern Pakistan during the summer of 2010 has been attributed to prolonged blocking events in the upper-troposphere over the Ural-Siberian region (Lau and Kim, 2012). Similarly, Vellore et al. (2016) analyzed the composite of extreme monsoon rainfall events over the western Himalaya and observed the formation of a blocking high over the Ural-Siberian region during those events. The impact of upper-tropospheric blocks on the weather of the entire Himalaya, however, is still unknown. The first objective **O1** of this thesis is to explore a relationship between the Ural-Siberian blocks and Himalayan weather anomalies.

Furthermore, due to the very limited resources for weather forecasting over the HKH, the weather forecasting system in many cases fails to predict the disastrous weather events. Furthermore, experiments involving sensitivity tests of different physical parameterization in the MAMs are limited to the western and eastern Himalaya. Thus, the second objective **O2** of this thesis is to perform sensitivity tests of different cloud microphysics schemes available within the WRF model at high spatial resolution to determine which scheme best

simulates extreme precipitation events over the Nepalese central Himalaya. WRF is a widely used MAM for both numerical weather prediction and atmospheric research. In Nepal, the Department of Hydrology and Meteorology (DHM), Nepal also uses the WRF model to forecast the weather. Thus, using the WRF model in my study will help to compare my results with the microphysics schemes used by the DHM to forecast the weather.

This thesis is organized into four chapters (considering this chapter as Chapter 1). Chapters 2 and 3 are written as independent papers to meet *O1* and *O2* respectively, and Chapter 4 summarizes the findings of the thesis and provides recommendations for future research.

References

- Andermann, C., Bonnet, S., and Gloaguen, R. (2011). Evaluation of precipitation data sets along the Himalayan front. *Geochemistry, Geophysics, Geosystems*, 12(7).
- Annamalai, H., Hamilton, K., and Sperber, K. R. (2007). The south Asian summer monsoon and its relationship with ENSO in the IPCC AR4 simulations. *Journal of Climate*, 20(6):1071–1092.
- Bader, M. J., Forbes, G. S., Grant, J. R., E., L. R. B., and Waters, J. (1995). Images in weather forecasting. Technical report, Cambridge University Press.
- Barros, A. P. and Lang, T. J. (2003). Monitoring the monsoon in the Himalayas: Observations in Central Nepal, June 2001. *Monthly Weather Review*, 131(7):1408–1427.
- Bharati, L., Gurung, P., Jayakody, P., Smakhtin, V., and Bhattarai, U. (2014). The projected impact of climate change on water availability and development in the Koshi basin, Nepal. *Mountain Research and Development*, 34(2):118 – 130 – 13.
- Bhatt, B. C. and Nakamura, K. (2005). Characteristics of monsoon rainfall around the Himalayas revealed by TRMM precipitation radar. *Monthly Weather Review*, 133(1):149–165.
- Bolch, T., Kulkarni, A., Kaab, A., Huggel, C., Paul, F., Cogley, J. G., Frey, H., Kargel, J. S., Fujita, K., Scheel, M., Bajracharya, S., and Stoffel, M. (2012). The state and fate of Himalayan glaciers. *Science*, 336(6079):310–314.
- Bonekamp, P. N. J., Collier, E., and Immerzeel, W. W. (2018). The impact of spatial resolution, landuse and spin-up time on resolving spatial precipitation patterns in the Himalayas. *Journal of Hydrometeorology*.
- Bookhagen, B. and Burbank, D. W. (2010). Toward a complete Himalayan hydrological budget: Spatiotemporal distribution of snowmelt and rainfall and their impact on river discharge. *Journal of Geophysical Research: Earth Surface*, 115(F3).
- Chawla, I., Osuri, K. K., Mujumdar, P. P., and Niyogi, D. (2018). Assessment of the Weather Research and Forecasting (WRF) model for simulation of extreme rainfall events in the upper Ganga Basin. *Hydrology and Earth System Sciences*, 22(2):1095–1117.
- Choudhary, A. and Dimri, A. P. (2018). Assessment of CORDEX-South Asia experiments for monsoonal precipitation over Himalayan region for future climate. *Climate Dynamics*, 50(7):3009–3030.
- Collier, E. and Immerzeel, W. W. (2015). High-resolution modeling of atmospheric dynamics in the Nepalese Himalaya. *Journal of Geophysical Research: Atmospheres*, 120(19):9882–9896.

- Collier, E., Mölg, T., Maussion, F., Scherer, D., Mayer, C., and Bush, A. B. G. (2013). High-resolution interactive modelling of the mountain glacier-atmosphere interface: an application over the Karakoram. *The Cryosphere*, 7(3):779–795.
- Dimri, A. P. and Mohanty, U. C. (2009). Simulation of mesoscale features associated with intense western disturbances over Western Himalayas. *Meteorological Applications*, 16(3):289–308.
- Dimri, A. P. and Niyogi, D. (2013). Regional climate model application at subgrid scale on Indian winter monsoon over the Western Himalayas. *International Journal of Climatology*, 33(9):2185–2205.
- Dimri, A. P., Niyogi, D., Barros, A. P., Ridley, J., Mohanty, U. C., Yasunari, T., and Sikka, D. R. (2015). Western disturbances: A review. *Reviews of Geophysics*, 53(2):225–246.
- Fan, F., Dong, X., Fang, X., Xue, F., Zheng, F., and Zhu, J. (2017). Revisiting the relationship between the South Asian summer monsoon drought and El Niño warming pattern. *Atmospheric Science Letters*, 18(4):175–182.
- Guhathakurta, P., Sreejith, O. P., and Menon, P. A. (2011). Impact of climate change on extreme rainfall events and flood risk in India. *Journal of Earth System Science*, 120(3):359.
- Hasson, S., Lucarini, V., and Pascale, S. (2013). Hydrological cycle over south and southeast Asian river basins as simulated by pcmdi/cmip3 experiments. *Earth System Dynamics*, 4(2):199–217.
- Hasson, S., Pascale, S., Lucarini, V., and Bhner, J. (2016). Seasonal cycle of precipitation over major river basins in south and southeast Asia: A review of the cmip5 climate models data for present climate and future climate projections. *Atmospheric Research*, 180:42 – 63.
- Holton, J. R. (1992). *An Introduction to Dynamical Meteorology*. Academic Press.
- Houze Jr., R. A., Wilton, D. C., and Smull, B. F. (2007). Monsoon convection in the Himalayan region as seen by the TRMM precipitation radar. *Quarterly Journal of the Royal Meteorological Society*, 133(627):1389–1411.
- Hunt, K. M. R., Turner, A. G., Inness, P. M., Parker, D. E., and Levine, R. C. (2016). On the structure and dynamics of Indian monsoon depressions. *Monthly Weather Review*, 144(9):3391–3416.
- Hunt, K. M. R., Turner, A. G., and Shaffrey, L. C. (2018). Extreme daily rainfall in Pakistan and north India: Scale interactions, mechanisms, and precursors. *Monthly Weather Review*, 146(4):1005–1022.
- Immerzeel, W. W., Pellicciotti, F., and Bierkens, M. F. P. (2013). Rising river flows throughout the twenty-first century in two Himalayan glacierized watersheds. *Nature Geoscience*, 6(742).

- IPCC (2012). Managing the risks of extreme events and disasters to advance climate change adaptation. a special report of working group I and II of the Intergovernmental Panel on Climate Change. Technical report, IPCC.
- Jang, Y. and Straus, D. M. (2012). The Indian monsoon circulation response to El niño diabatic heating. *Journal of Climate*, 25(21):7487–7508.
- Joshi, S. and Kar, S. C. (2018). Mechanism of ENSO influence on the south Asian monsoon rainfall in global model simulations. *Theoretical and Applied Climatology*, 131(3):1449–1464.
- Karki, R., Ul-Hasson, S., Gerlitz, L., Schickhoff, U., Scholten, T., and Bøhner, J. (2017). Quantifying the added value of convection-permitting climate simulations in complex terrain: A systematic evaluation of WRF over the Himalayas. *Earth System Dynamics*, 8(3):507–528.
- Lang, T. J. and Barros, A. P. (2004). Winter Storms in the Central Himalayas. *Journal of the Meteorological Society of Japan*, 82(3):829–844.
- Lau, W. K. M. and Kim, K.-M. (2012). The 2010 Pakistan flood and Russian heat wave: Teleconnection of hydrometeorological extremes. *Journal of Hydrometeorology*, 13(1):392–403.
- Maharjan, S., Mool, P., Lizong, W., Xiao, G., Shrestha, F., Shrestha, R., Khanal, N., Bajracharya, S., Joshi, S., Shai, S., and Baral, P. (2018). The status of glacial lakes in the Hindu Kush Himalaya. Technical report, ICIMOD, ICIMOD, Kathmandu.
- Medina, S., Houze, R. A., Kumar, A., and Niyogi, D. (2010). Summer monsoon convection in the Himalayan region: Terrain and land cover effects. *Quarterly Journal of the Royal Meteorological Society*, 136(648):593–616.
- Mishra, V. (2015). Climatic uncertainty in Himalayan water towers. *Journal of Geophysical Research: Atmospheres*, 120(7):2689–2705.
- Mooley, D. A. and Parthasarathy, B. (1983). Indian summer monsoon and El Niño. *pure and applied geophysics*, 121(2):339–352.
- Mujumdar, M., Preethi, B., Sabin, T. P., Ashok, K., Saeed, S., Pai, D. S., and Krishnan, R. (2012). The Asian summer monsoon response to the La Niña event of 2010. *Meteorological Applications*, 19(2):216–225.
- Norris, J., Carvalho, L. M., Jones, C., and Cannon, F. (2019). Deciphering the contrasting climatic trends between the central Himalaya and Karakoram with 36 years of WRF simulations. *Climate Dynamics*, 52(1-2):159–180.

- Orr, A., Listowski, C., Coultet, M., Collier, E., Immerzeel, W., Deb, P., and Bannister, D. (2017). Sensitivity of simulated summer monsoonal precipitation in Langtang Valley, Himalaya, to cloud microphysics schemes in WRF. *Journal of Geophysical Research: Atmospheres*, 122(12):6298–6318.
- Park, H. S., Chiang, J. C., and Bordoni, S. (2012). The mechanical impact of the Tibetan Plateau on the seasonal evolution of the South Asian monsoon. *Journal of Climate*, 25(7):2394–2407.
- Patil, R. and Pradeep Kumar, P. (2016). WRF model sensitivity for simulating intense western disturbances over North West India. *Modeling Earth Systems and Environment*, 2(2):82.
- Prasad, V. S. and Hayashi, T. (2005). Onset and withdrawal of Indian summer monsoon. *Geophysical Research Letters*, 32(L20715).
- Rajeevan, M., De, U. S., and Prasad, R. K. (2000). Decadal variation of sea surface temperatures, cloudiness and monsoon depression in the North Indian Ocean. *Current Science*, 9:283–285.
- Ren, Y.-Y., Ren, G.-Y., Sun, X.-B., Shrestha, A. B., You, Q.-L., Zhan, Y.-J., Rajbhandari, R., Zhang, P.-F., and Wen, K.-M. (2017). Observed changes in surface air temperature and precipitation in the Hindu Kush Himalayan region over the last 100-plus years. *Advances in Climate Change Research*, 8(3):148 – 156. Including special issue on climate change in the Hindu Kush Himalaya.
- Revadekar, J. V., Hameed, S., Collins, D., Manton, M., Sheikh, M., Borgaonkar, H. P., Kothawale, D. R., Adnan, M., Ahmed, A. U., Ashraf, J., Baidya, S., Islam, N., Jayasinghearachchi, D., Manzoor, N., Premalal, K. H. M. S., and Shrestha, M. L. (2013). Impact of altitude and latitude on changes in temperature extremes over South Asia during 1971-2000. *International Journal of Climatology*, 33(1):199–209.
- Sato, T. and Kimura, F. (2007). How does the Tibetan Plateau affect the transition of Indian monsoon rainfall? *Monthly Weather Review*, 135(5):2006–2015.
- Shea, J. M., Immerzeel, W. W., Wagnon, P., Vincent, C., and Bajracharya, S. (2015). Modelling glacier change in the Everest region, Nepal Himalaya. *Cryosphere*, 9(3):1105–1128.
- Shrestha, D., Singh, P., and Nakamura, K. (2012). Spatiotemporal variation of rainfall over the central Himalayan region revealed by TRMM precipitation radar. *Journal of Geophysical Research: Atmospheres*, 117(D22).
- Shrestha, P., Dimri, A. P., Schomburg, A., and Simmer, C. (2015). Improved understanding of an extreme rainfall event at the Himalayan foothills: a case study using COSMO. *Tellus A: Dynamic Meteorology and Oceanography*, 67(1):26031.

- Singh, D., Jain, S. K., and Gupta, R. D. (2015). Trend in observed and projected maximum and minimum temperature over N-W Himalayan basin. *Journal of Mountain Science*, 12(2):417–433.
- Singh, D., Tsiang, M., Rajaratnam, B., and Diffenbaugh, N. S. (2014). Observed changes in extreme wet and dry spells during the south Asian summer monsoon season. *Nature Climate Change*, 4:456–461.
- Thompson, S., Benn, D. I., Mertes, J., and Luckman, A. (2016). Stagnation and mass loss on a Himalayan debris-covered glacier: processes, patterns and rates. *Journal of Glaciology*, 62(233):467485.
- van, Vuuren, D. P., Edmonds, J., Kainuma, M., Riahi, K., Thomson, A., Hibbard, K., Hurtt, G. C., Kram, T., Krey, V., Lamarque, J.-F., Masui, T., Meinshausen, M., Nakicenovic, N., Smith, S. J., and Rose, S. K. (2011). The representative concentration pathways: an overview. *Climatic Change*, 109(1):5.
- Vellore, R. K., Kaplan, M. L., Krishnan, R., Lewis, J. M., Sabade, S., Deshpande, N., Singh, B. B., Madhura, R. K., and Rama Rao, M. V. (2016). Monsoon-extratropical circulation interactions in Himalayan extreme rainfall. *Climate Dynamics*, 46(11-12):3517–3546.
- Vincent, C., Wagnon, P., Shea, J. M., Immerzeel, W. W., Kraaijenbrink, P., Shrestha, D., Soruco, A., Arnaud, Y., Brun, F., Berthier, E., and Sherpa, S. F. (2016). Reduced melt on debris-covered glaciers: Investigations from Changri Nup glacier, Nepal. *Cryosphere*, 10(4):1845–1858.
- Wester, P., A., M., A., M., and A. B., S., editors (2019). *The Hindu kush Himalaya Assessment - Mountains, Climate Change, Sustainability, and People*. Springer Nature, Switzerland AG, Cham.
- Xie, A., Ren, J., Qin, X., and Kang, S. (2007). Reliability of NCEP/NCAR reanalysis data in the Himalayas/Tibetan plateau. *Journal of Geographical Sciences*, 17(4):421–430.
- Yatagai, A., Kamiguchi, K., Arakawa, O., Hamada, A., Yasutomi, N., and Kitoh, A. (2012). Aphrodite: Constructing a long-term daily gridded precipitation dataset for Asia based on a dense network of rain gauges. *Bulletin of the American Meteorological Society*, 93(9):1401–1415.

Chapter 2

A Relationship between Ural-Siberian Blocking and Himalayan Weather Anomalies

Under review in *Earth and Space Science*

U. Tiwari and A.B.G. Bush

2.1 Abstract

Because of their distinctly high elevation, the Himalaya are directly influenced by upper-tropospheric Jet stream winds and circulation anomalies that on many occasions have brought unusual weather patterns to the region. In this study, we establish the dynamical relationship between upper-tropospheric blocks formed over the Ural-Siberian region and anomalous weather patterns over the Himalaya using a combination of reanalysis data and mesoscale atmospheric model simulations. We identify two distinct blocks (an omega (Ω) block and a dipole (Rex) block) using an appropriate blocking index and computed the anomalous atmospheric fields associated with these types of blocks. In both cases, the low-pressure component of the block lies westward of the western Himalaya and the upper-level convergence/divergence of ageostrophic winds along the upstream/downstream portion of the trough creates anomalous positive/negative sea level pressure at the surface. The local sea level pressure is enhanced over the Arabian Peninsula and the Arabian Sea, while downwind over the Himalaya there is a negative pressure anomaly. There is entrainment of high potential vorticity (PV) air that descends and flows equatorward. During the Ω blocking event, the trough remains quasi-stationary over the western Himalayan

notch and its circulation induces moisture transport from the Arabian Sea and the Bay of Bengal leading to strong precipitation events over the western and eastern Himalayan notches. During the dipole blocking event, the trough gradually shifts south-eastward and leads to widespread precipitation over the entire Himalayan arc.

2.2 Introduction

Atmospheric blocking events can bring anomalous and potentially extreme weather patterns to regions immediately around the blocks and to distant downstream regions. These patterns may last for a few days to a few weeks. They are formed by quasi-stationary high and low-pressure systems in the upper troposphere that block the flow of the eastward-moving jet stream, thereby inducing more meridional flow and more north-south exchanges of air masses and energy (Rex, 1950). Poleward advection of warm sub-tropical air typically occurs along the upstream edge of an anticyclonic midlatitude block and equatorward advection of cold polar air occurs along the downstream edge of the block. Together, these anomalous flows can result in such weather extremes as heat waves, cold waves, drought, and flooding. Documented examples of weather anomalies related to atmospheric blocking events are: warm temperature anomalies in western Alaska (Carrera et al., 2004); cold anomalies over the western and southern United States (Casola and Wallace, 2007); cold spells in south-eastern Europe (Brunner et al., 2017); cold anomalies over eastern Asia (Park and An, 2014), and; enhanced precipitation over southeastern Australia (Pook et al., 2013).

The most common regions for the development of blocking events in the Northern Hemisphere are the Euro-Atlantic region, the Pacific Ocean and the Ural-Siberian region over the Eurasian continent ((Barriopedro et al., 2006; Cheung et al., 2013a). In this paper, we focus on Ural-Siberian blocks and their associated weather events in south/south-east Asia and the Himalaya. According to Takaya and Nakamura (2005), the upper tropospheric blocking anticyclone over the Ural-Siberian region is associated with the eastward propagating component of a quasi-stationary Rossby wave train originating from the Euro-Atlantic sector. They further explained that the blocking ridge strengthens the amplitude of the Siberian high leading to cold air outbreaks along the downstream region for extended periods of time.

Blocking episodes over Eurasia are less persistent than over other regions (Tyrlis and Hoskins, 2008), although they are known to cause anomalous weather patterns over south/south-east Asia. For example, severe snowstorms across southern China in January 2008 and a Russian heat wave and Pakistan flooding during summer 2010 have been dynamically linked with an extended blocking episode over the Ural-Siberian region (Lau and Kim, 2012; Zhou et al., 2009).

The study of blocking events may lead to an improved predictive capability for anomalous Himalayan weather. The distinctly high elevations of the Himalayan Mountains control the atmospheric flows across and

around them resulting in dynamical interactions between the orography and, for example, the summer monsoon circulation and westerly wind disturbances (Cannon et al., 2014; Medina et al., 2010). Furthermore, Vellore et al. (2016) established the relationship between extreme summer monsoon precipitation events and anomalous mid-latitude upper-tropospheric circulation including atmospheric blocking events over Eurasia. However, their study is confined to a small region in the western Himalaya and does not explore how blocking influences the weather of the entire Himalayan region in other seasons.

The aim of this study is to ascertain the influence of atmospheric blocks on pan-Himalayan weather. We compute an appropriate blocking index to identify blocking events in the Ural-Siberian region and analyze the synoptic and mesoscale atmospheric conditions over Eurasia and the Himalaya during two typical but contrasting blocking events (an Ω block event and a dipole block event) that occurred in the spring and winter seasons. We use reanalysis data as well as simulated high-resolution atmospheric fields over the Himalaya using a mesoscale atmospheric model in order to ascertain the anomalies generated by these two different types of blocking events.

2.3 Materials and Methods

2.3.1 Data

The atmospheric variables used in the calculation of the blocking indices are from the ERA-Interim reanalysis dataset (Dee et al., 2011). ERA-Interim data are the products of the European Centre for Medium-Range Weather Forecasts (ECMWF). They are available at six hourly temporal resolution, $0.75^{\circ} \times 0.75^{\circ}$ default horizontal resolution (with different user selectable options), and 61 variably spaced vertical levels from the surface to 0.1 hPa. Thus, ERA-Interim geopotential height at 500 hPa pressure level and $2.5^{\circ} \times 2.5^{\circ}$ horizontal resolution is used to calculate the blocking index. For all other calculations ERA-Interim data with default horizontal resolution are used. The ERA-Interim variables considered in this study are geopotential height, horizontal winds (u and v components), temperature, and surface evaporation.

Furthermore, the ERA-Interim reanalysis dataset is used to initialize and force the atmospheric model at its lateral boundaries. The model output precipitation is compared with daily Tropical Rainfall Measuring Mission (TRMM) precipitation data at $0.25^{\circ} \times 0.25^{\circ}$ horizontal resolution (Huffman et al., 2010). Likewise, the spatial extent of the simulated snow cover is compared with MODIS/Terra Snow Cover Daily L3 Global 500m Grid, Version 6 (<http://modis.gsfc.nasa.gov>).

2.3.2 Methods

The index used to detect atmospheric blocking events in this paper is derived from Lejenäs and Økland (1983) and Tibaldi and Molteni (1990). The blocking index includes 500-hPa geopotential height gradients (GHGN and GHGS) computed daily for each longitude as given below:

$$GHGN = \left[\frac{Z(\lambda, \phi_n) - Z(\lambda, \phi_o)}{\phi_n - \phi_o} \right] \quad (2.1)$$

$$GHGS = \left[\frac{Z(\lambda, \phi_o) - Z(\lambda, \phi_s)}{\phi_o - \phi_s} \right] \quad (2.2)$$

where, $\phi_n = 80^0N + \delta$, $\phi_o = 60^0N + \delta$, $\phi_s = 40^0N + \delta$, and $\delta = -7.5, -5, -2.5, 0, 2.5, 5, 7.5$. The use of δ values ranging from -7.5 to 7.5 is due to the seasonal and spatial variations of the locations of blocks over the Ural-Siberian region. Furthermore, reason behind the selection of δ at an interval of 2.5 is due to data resolution.

In the above expression $Z(\lambda, \phi)$ is the 500-hPa geopotential height at longitude λ and latitude ϕ . A given longitude is considered to be blocked if the value of $GHGS > 0$ and $GHGN < -10$ per degree of latitude for at least one value of δ (Barriopedro et al., 2006).

A blocking frequency is defined as the percentage ratio of the number of blocked days to the total number of days over a study period. To be defined as a blocking event, the index must have at least five consecutive points of longitude (12.5^0 for the resolution of the data) blocked (Barriopedro et al., 2006) and the block must persist for at least four consecutive days (Pelly and Hoskins, 2003).

We compute GHGS and GHGN between 1985 and 2015 and identify blocking events upstream of the Himalaya. The blocking events are then classified according to the season and annual number of blocking events. Based on the persistence and the type of upper atmospheric features two blocking events (an omega (Ω) and a dipole (Rex) block) formed after 2000 are selected as case studies to study the anomalous weather conditions over the Himalaya. The reason behind the consideration of events after 2000 is the availability of TRMM and MODIS data which provide better comparison than reanalysis data with the high-resolution numerical simulations.

2.3.3 Regional modeling of atmospheric conditions over the Himalaya during the blocking events

The Weather Research and Forecasting (WRF) Model version 3.8.1 is used to simulate the high-resolution atmospheric fields over the Himalaya during two different types of blocking events (an Ω and a dipole block).

The WRF model is a non-hydrostatic and fully compressible mesoscale atmospheric model. It is configured with two nested domains of 18 and 6 Km horizontal resolutions with both domains having 50 vertical levels. The model top is at 50 hPa and the lowest 11 model levels are below 1 km altitude. The geographical coordinates of the outer domain (D1) and the inner domain (D2) are shown in Fig. 2.1. The locations of the Western Himalayan Notch (WHN) and the Eastern Himalayan Notch (EHN) are indicated in Fig 1b. The WHN is a notch formed by the Hindu Kush Mountains, the Karakoram, and the western Himalaya. Similarly, the EHN is a notch formed by the Eastern Himalaya and the mountains along the Indo-Burma border. In this study we define the Nepal Himalaya as the Central Himalaya. Thus, the region east of Nepal, we define as the Eastern Himalaya, and the region west of Nepal, including the Karakoram and the Hindu Kush, we define as the western Himalaya.

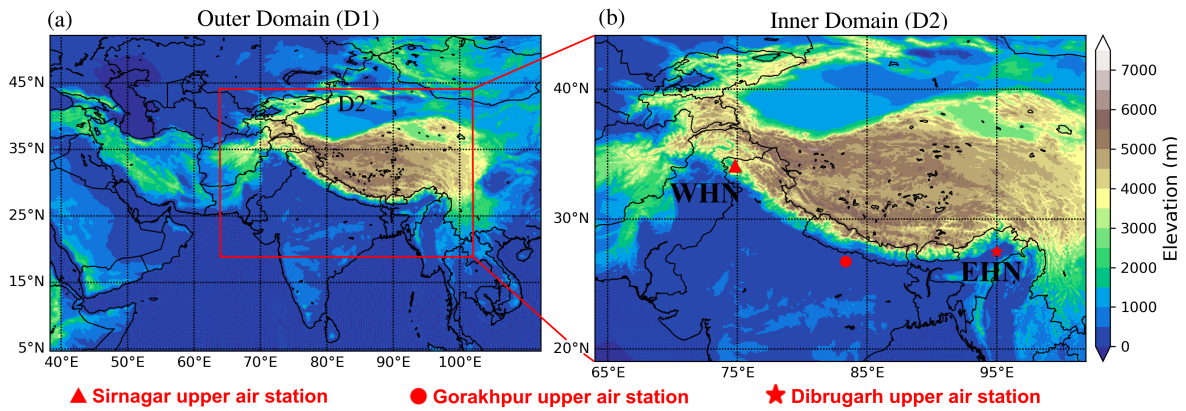


Figure 2.1. The WRF model domains. (a) The outer domain (D1) with 18Km horizontal grid spacing; the red rectangle shows the location of the inner domain (D2) and (b) the inner domain (D2) with 6 Km horizontal grid spacing. WHN and EHN in D2 refer to Western Himalayan Notch (WHN) and Eastern Himalayan Notch (EHN) respectively. Shading in both (a) and (b) indicates modeled elevation above sea level (m, asl).

D1 uses 5 arcmins (~ 9.5 Km) topography and D2 uses 2 arcmins (~ 4 Km) topography with USGS 24-category land use classification. Due to the resolution of the input topography, the model topography slightly underestimates the actual topography (especially around the mountain peaks). WRF is run using 2-way nesting with the physical and dynamical parameters based on previous studies for similar domains (Karki et al., 2017; Norris et al., 2015), as presented in Table 2.1. D1 is forced at its lateral boundaries by ERA-Interim data. Moreover, the WRF model is initialized at 00Z 7 May 2014 (for Case I) and 00Z 31 January 2012 (for case II). The first 24 hours are considered as model spin-up period and are discarded during the analysis. These simulations are carried in Compute Canada Clusters (Graham) and the simulations take 21 hours to complete (including both case I and II).

Table 2.1. WRF model configuration

Domain Configuration	
<i>Horizontal grid spacing</i>	18 and 6 Km
<i>Vertical levels</i>	50
<i>Model top pressure</i>	50-hPa
Model Physics	
<i>Radiation</i>	Community Atmospheric Model
<i>Microphysics</i>	Thompson (Thompson et al., 2008)
<i>Cumulus</i>	Kain-Fritsch (Kain, 2004)
<i>Planetary boundary layer</i>	MYNN level 2.5 (Nakanishi and Niino, 2006, 2009)
<i>Atmospheric surface layer</i>	revised MM5 (Jiménez et al., 2012)
<i>Land surface model</i>	NOAH-MP (Niu et al., 2011; Yang et al., 2011)
Dynamics	
<i>Top boundary condition</i>	Rayleigh damping
<i>Diffusion</i>	Calculated in physical space
Lateral Boundaries	
<i>Forcing</i>	ERA-Interim 0.75 ⁰ X 0.75 ⁰ , 6 hourly

2.4 Results

2.4.1 Blocking frequency from ERA-Interim data

The average blocking frequency over 45⁰E to 75⁰E (from 1985 to 2015) is calculated for spring (March to May), summer (June to August), autumn (September to November) and winter (December to February) seasons. In all seasons, peak blocking frequencies (in terms of percentage ratio of days blocked to the total number of days) are observed between $\sim 55^{\circ}$ E to 70° E longitudes (Fig. 2.2a), after a sharp drop in the blocking frequency through the Euro-Atlantic sector (peak values on far left corner of Fig. 2.2a), which is the typical region for the formation of Ural-Siberian blocks (Cheung et al., 2013a,b). Thus, we focus on atmospheric blocks formed within these longitudes and on their associated downstream impacts on Himalayan weather as demonstrated by two unique cases.

Furthermore, the average number of blocking events in a year is 2.7 with the highest number of blocking events (six) observed in 1996, and zero blocking events in 1997 (Fig. 2.2b). Atmospheric blocking events over the Ural-Siberian region have been shown to be associated with the Arctic Oscillation (AO) and the El Niño Southern Oscillation (ENSO), with fewer events when either AO or ENSO are in their positive phase (Cheung et al., 2012).

2.4.2 Case I: Blocking event (9-17 May 2014)

This section deals with an Ω block formed over the Ural-Siberian region during the spring season of 2014 which persisted for 9 days (9-17 May 2014). The synoptic conditions associated with this Ω block are determined using ERA-Interim reanalysis data and a WRF simulation is used to analyze the anomalous weather conditions over

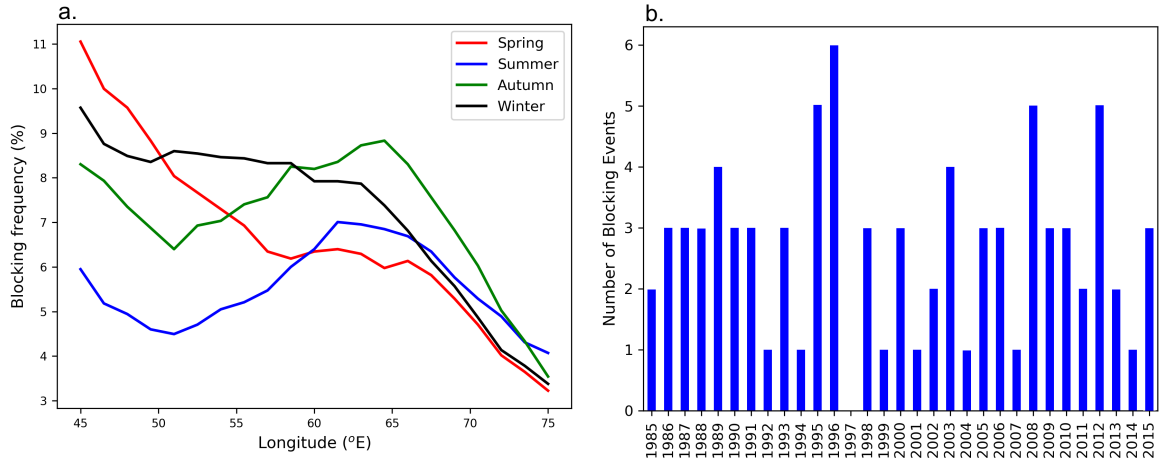


Figure 2.2. (a) Average blocking frequency from 1985 to 2015 over 45°E to 75°E according to the season, and (b) number of blocking events per year from 1985 to 2015 centered between 55°E and 70°E.

the Himalaya and South Asia during this event.

Synoptic conditions

The daily wind and height anomaly fields at the 200 hPa pressure level show the formation of an Ω block over Eurasia (Fig. 2.3). This Ω block is characterized by a high-pressure ridge lying over Eurasia and subtropical troughs at its leading and trailing edges. The trough at the leading edge (western trough) lies over the Mediterranean region, and the trough at the trailing edge (eastern trough) extends from the Arabian Sea to the western Himalaya (lying over Pakistan, eastern Afghanistan, and north-western India, Fig. 2.3). Another prominent feature is the presence of upper-level anti-cyclonic wind anomalies over central Asia. The circulation anomalies associated with the eastern trough imply southward cold advection over the western Himalaya and northward warm advection over the central and eastern Himalaya.

The large-scale forcing associated with the upper atmospheric eastern trough resulted in negative MSLP anomalies over the Himalayan arc that extend up to southern China. Conversely, the MSLP anomalies over South Asia display positive values. Furthermore, the 850 hPa wind field shows cyclonic flows over the Hindu Kush Mountains and anti-cyclonic flows over central India (Fig. 2.4) which couple to generate convergent low-level winds over the WHN.

The isentropic potential vorticity (PV) (on the 350 K surface) displays a reversal of the meridional PV gradient with high PV air circulating anticyclonically equatorward and low PV air moving poleward, an indicator of Rossby wave breaking (RWB) in the region (Postel and Hitchman, 1999) and a feature that is often associated with blocking anticyclones in the mid-latitudes (Pelly and Hoskins, 2003). Due to the entrainment of high PV air of stratospheric origin, the PV values over the western Himalaya are above 4 potential vorticity unit (PVU)

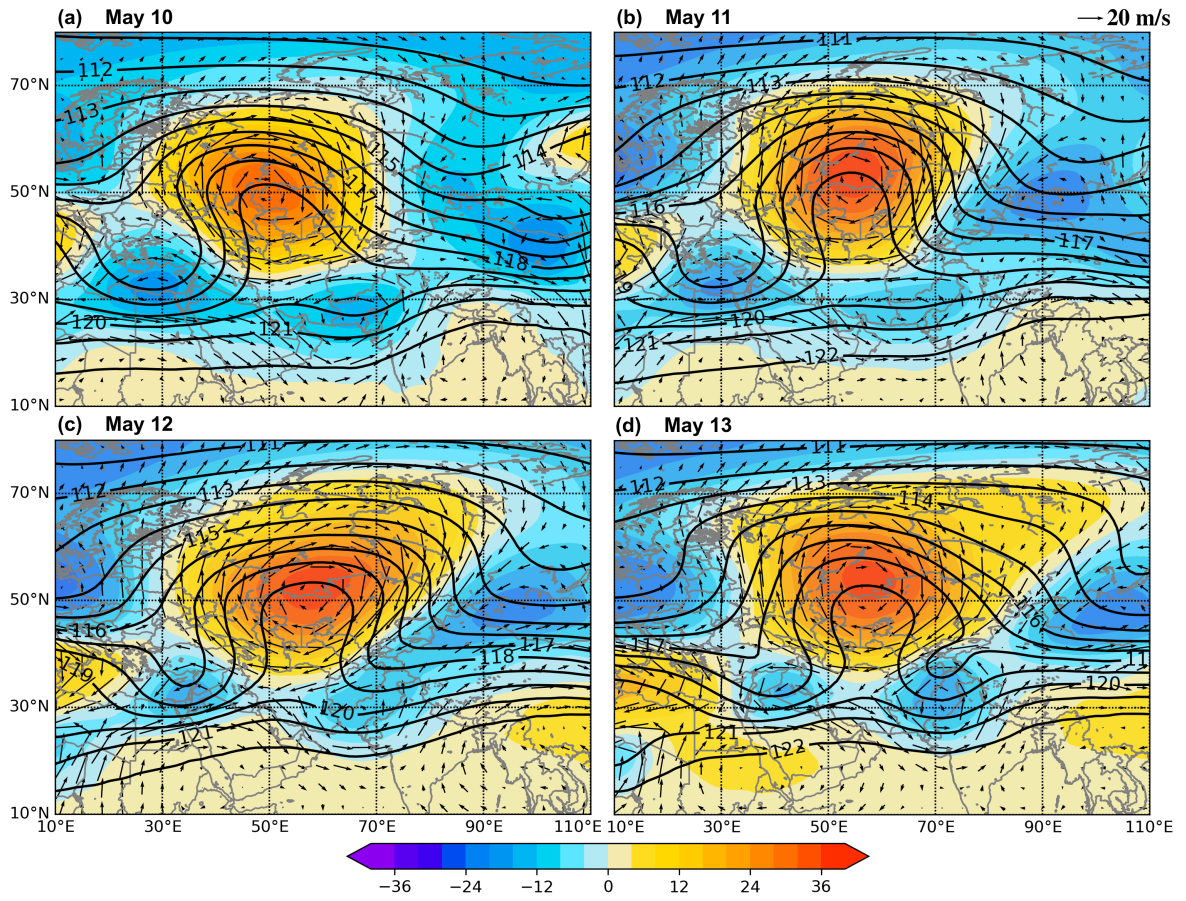


Figure 2.3. Daily 200 hPa geopotential height anomalies (shaded, m), geopotential height (contour, hectometer) and anomalous horizontal wind (vector, m/s) on (a) May 10, (b) May 11, (c) May 12, and (d) May 13 2014 (Source: ERA-Interim reanalysis).

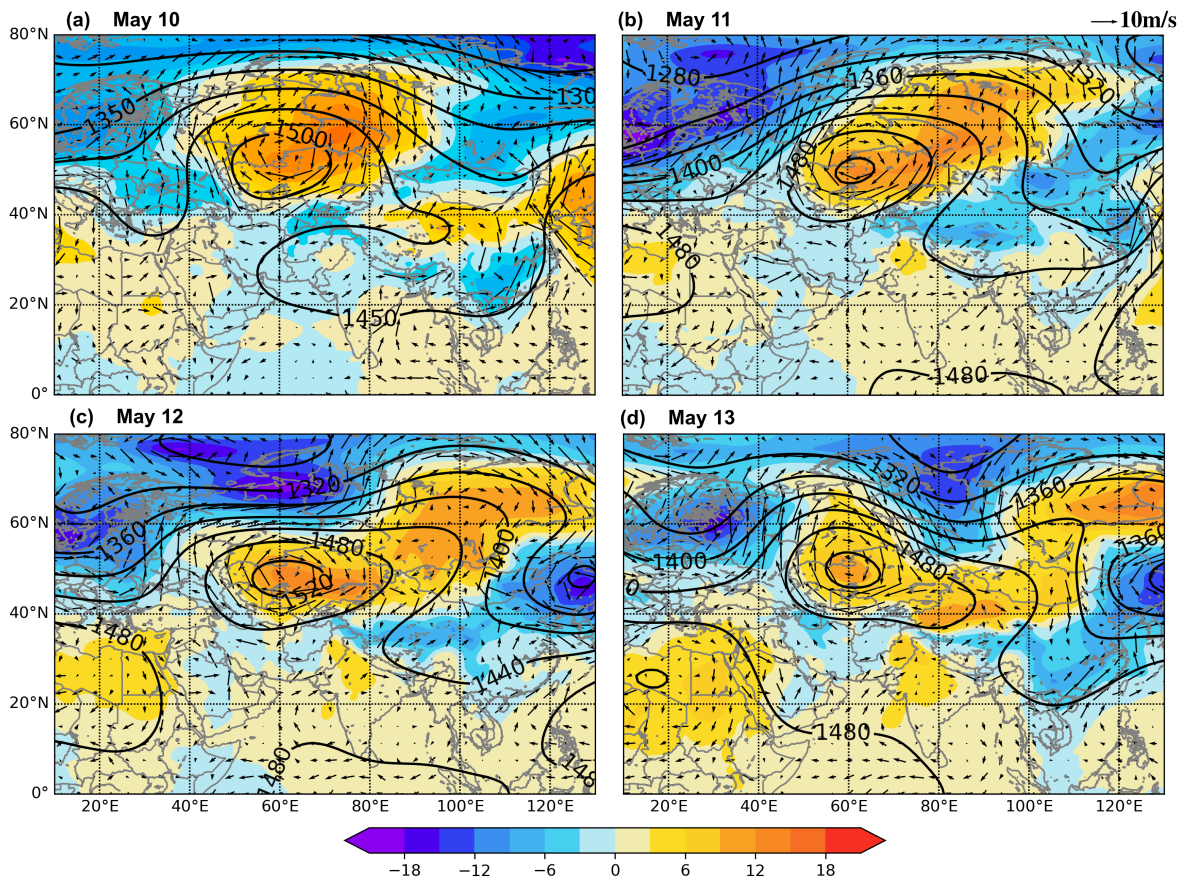


Figure 2.4. Daily mean sea level pressure anomalies (shaded, hPa), 850 hPa geopotential height (black contour, m), and 850 hPa anomalous wind (vector, m/s) on (a) May 10, (b) May 11, (c) May 12, and (d) May 13, 2014 (Source: ERA-Interim reanalysis).

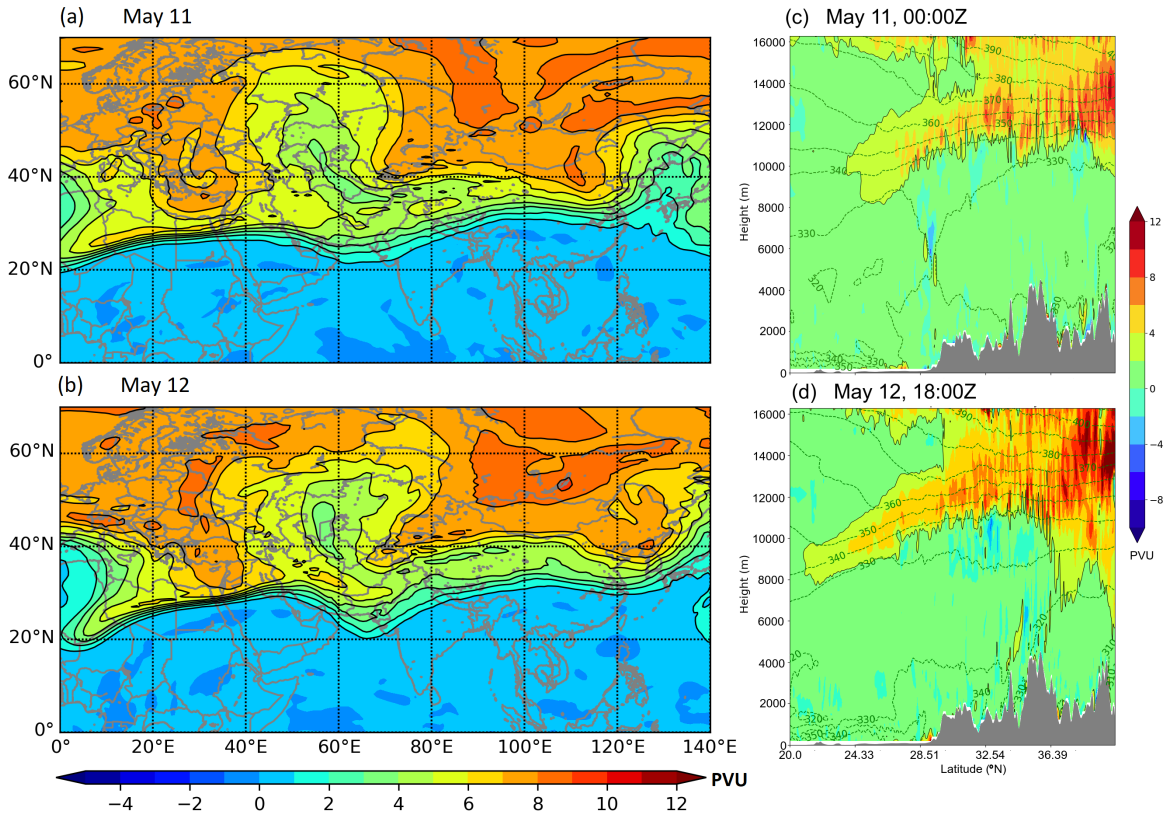


Figure 2.5. Daily PV (PVU) on 350 K isentropic surface on (a) May 11, (b) May 12, 2014. $PV \geq 1$ PVU are contoured (Source: ERA-Interim reanalysis); vertical cross section of daily simulated PV (shaded) and potential temperature (θ , green contour) on (c) May 11, 00:00Z and (d) May 12, 18:00Z along 70°E longitude (c and d are plotted from WRF simulations).

(Figs. 2.5a and b). Furthermore, a tongue of high PV air descends to 4000 m (Fig. 2.5d) illustrating strong tropopause folding over the western Himalaya.

WRF simulation of the atmospheric condition over the Himalaya during an Ω blocking event

WRF simulates high amounts of precipitation near the topographic notches in the western and the eastern Himalaya during this blocking event (Fig. 2.6). There is a distinct variation in the type of precipitation along the topographic gradients. Lower elevations in both the western and eastern Himalaya receive rain, while the higher elevations receive snow (Figs. 2.6a and 2.6b). For model validation, the spatial coverage and the quantity of precipitation simulated by WRF are compared with the TRMM precipitation dataset. The spatial coverage of simulated precipitation is consistent with the TRMM dataset. Simulated peak rainfall, however, is nearly double the magnitude of the observed peak over the higher elevation regions, although the quality of satellite observations is poor along the steep topographic gradients of the Himalaya, while they are more accurate over flat terrain (Andermann et al., 2011). The TRMM dataset has been shown to underestimate the precipitation

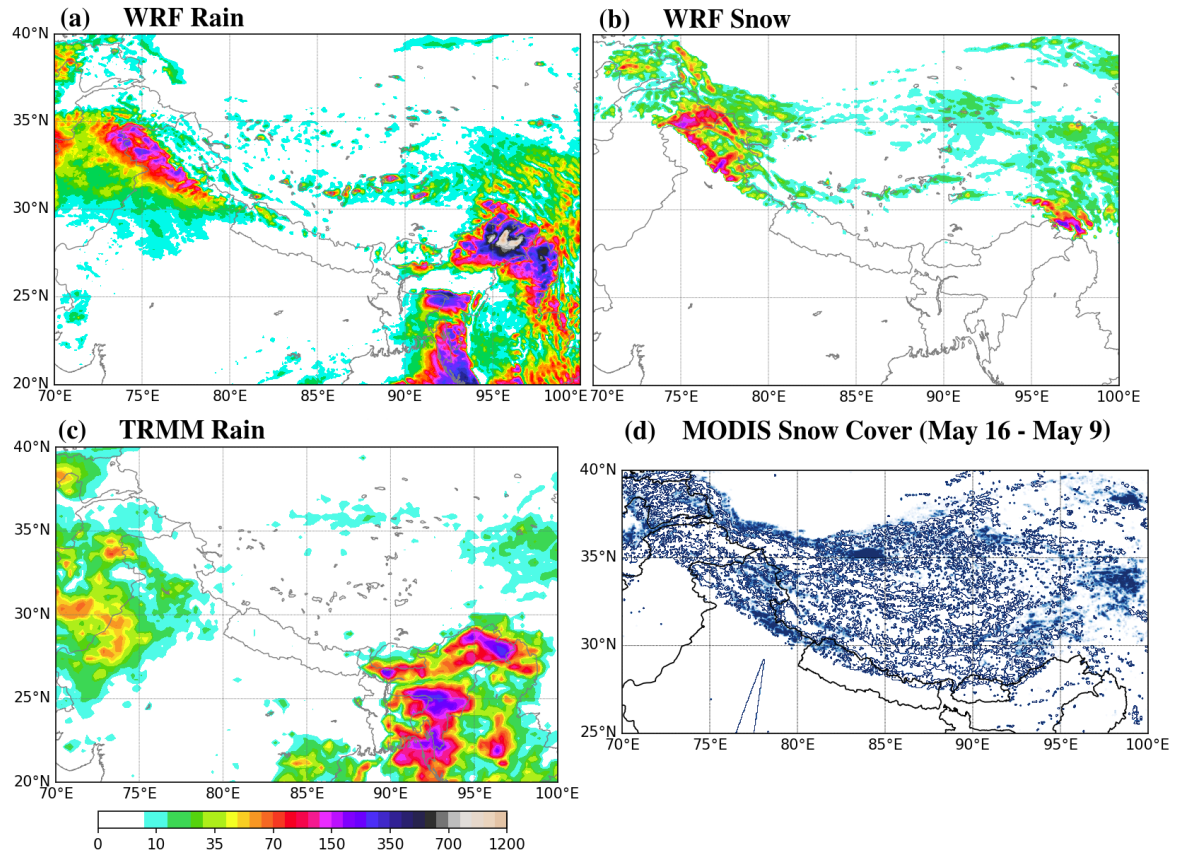


Figure 2.6. (a) WRF rainfall, (b) WRF snowfall, and (c) TRMM precipitation accumulated over 9 - 17 May 2014; (d) MODIS snow cover difference between May 16 and May 9.

magnitude above 3100 m and overestimate it below, with relatively good performance between 1000 - 2000 m elevation over the Himalaya (Bharti and Singh, 2015). TRMM data underestimate solid precipitation, so we compare the model snowfall with the MODIS snow cover product, which provides validation to our simulation, as indicated by an increase in the extent of snow cover over the western Himalaya in the MODIS product during the study period (red boxes Fig. 2.6).

Analysis of daily precipitation during this blocking event reveals strong precipitation over the WHN on May 11, 12, and 13 (Figs. 2.7b, c, and d), while the EHN receives precipitation throughout the blocking event. Strong precipitation over the western Himalaya is induced by winds converging onto the WHN (e.g., Fig. 2.4). The topographic divide of the western Himalaya around 30.5°N and 77°E splits the moisture-laden westerly winds into two components, one of which converges towards the north-western parts of the western Himalaya, while the other flows eastward along the southern margin of the Himalaya bringing precipitation to the EHN.

Higher values (greater than 45 mm) of precipitable water are observed over the region extending from the Bay of Bengal to the eastern Himalaya. Similarly, 30 mm to 40 mm of precipitable water is observed over the WHN on May 10, 11, 12 and 13 (Figs. 2.7f, g, h, and i). To identify the sources of moisture during the blocking

episode, the vertically integrated moisture flux (VIMF) is computed. The horizontal components of mean VIMF are defined as the horizontal moisture flux in the zonal (Q_u) and meridional (Q_v) directions integrated from the surface to 300 hPa pressure level, i.e.,

$$Q_u = \frac{1}{g} \int_{P_u}^{P_s} q u \, dp \quad (2.3)$$

$$Q_v = \frac{1}{g} \int_{P_u}^{P_s} q v \, dp \quad (2.4)$$

where, g is gravitational acceleration, q is specific humidity, u and v are zonal and meridional components of wind, P_s is the surface and P_u is 300 hPa. The magnitude of VIMF is computed as the vector magnitude of Q_u and Q_v .

The VIMF displays strong moisture transport over the EHN from the Bay of Bengal and the Arabian Sea. Similarly, the western Himalaya receives moisture from the Arabian Sea and a possible distal mid-latitude sources (e.g. the Mediterranean and Caspian Seas) facilitated by the cyclonic circulation induced by the block. Thus, cyclones with strong flows across the topography and enough moisture flux lead to strong precipitation along the mountains' topographic gradient (LANG and BARROS, 2004) as demonstrated by the intense simulated precipitation (~ 100 mm per day) over the western Himalaya on May 12 (Figs. 2.7c and h).

The ERA-Interim evaporation data indicate strong evaporation over the tropical water bodies with higher values over the Arabian Sea and the Bay of Bengal during the blocking event (Figs. 2.7k, l, m, n, and o). The spatial plots of moisture flux, evaporation and precipitable water and their comparison show the region extending from the Bay of Bengal to the EHN along the border of Bangladesh, India, and Myanmar exhibits intense evaporation, strong moisture flux, and high precipitable water (Fig. 2.7). Thus, the accumulated precipitation over those regions during the blocking event is also very high.

The 700 hPa temperature advection during this blocking event displays cold advection over the central and western Himalaya (Figs. 2.8a and b). Temperature advection over the Hindu Kush Mountains is, however, positive. The cold/warm advection associated with the block plays an important role in lowering/raising the freezing level. Thus, the cold advection associated with the block lowers the freezing level over the western Himalaya as depicted by radiosonde profiles (Skew-T diagram) obtained from the Srinagar station, India (34.05°N and 74.5°E , Fig. 2.9). The Skew-T diagram further displays the presence of a thick moist layer from the surface to 200 hPa (\sim the height of the tropopause) and indicates a convectively unstable layer with dry mid-tropospheric air lying between moist layers below and above.

Similarly, the Skew-T diagrams from the Dibrugarh station, Assam, India (27.48°N and 95.01°E) on 00Z May 12 and 13 exhibit a thick moist layer from the surface to 550 hPa (Fig. 2.10). Wind barbs indicate the lower tropospheric air (950 to 850 hPa) as coming from the Bay of Bengal, while the winds above are westerly

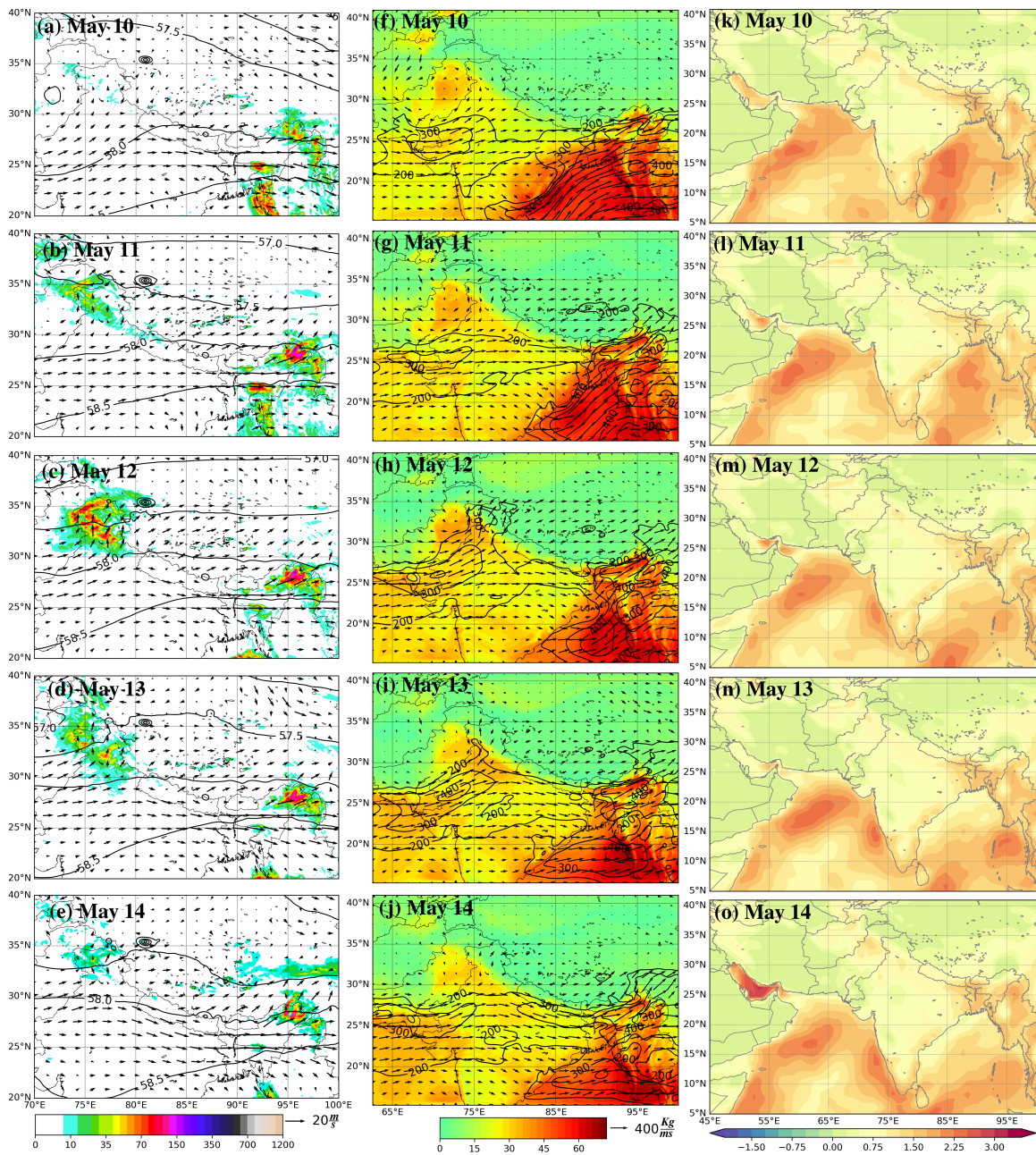


Figure 2.7. (a), (b), (c), (d), and (e) daily accumulated precipitation (shaded, mm), 500 hPa geopotential height (contour, hectometer), 700 hPa wind (vector, m/s) from WRF simulations; (f), (g), (h), (i), and (j) precipitable water (shaded, mm), vertically integrated moisture flux (vector indicating direction and contour indicating magnitude, $\text{kg m}^{-1} \text{s}^{-1}$) computed from WRF simulations, and; (k), (l), (m), (n) and (o) ERA-Interim surface evaporation (m of water) for May 10, 11, 12, 14, and 14 respectively.

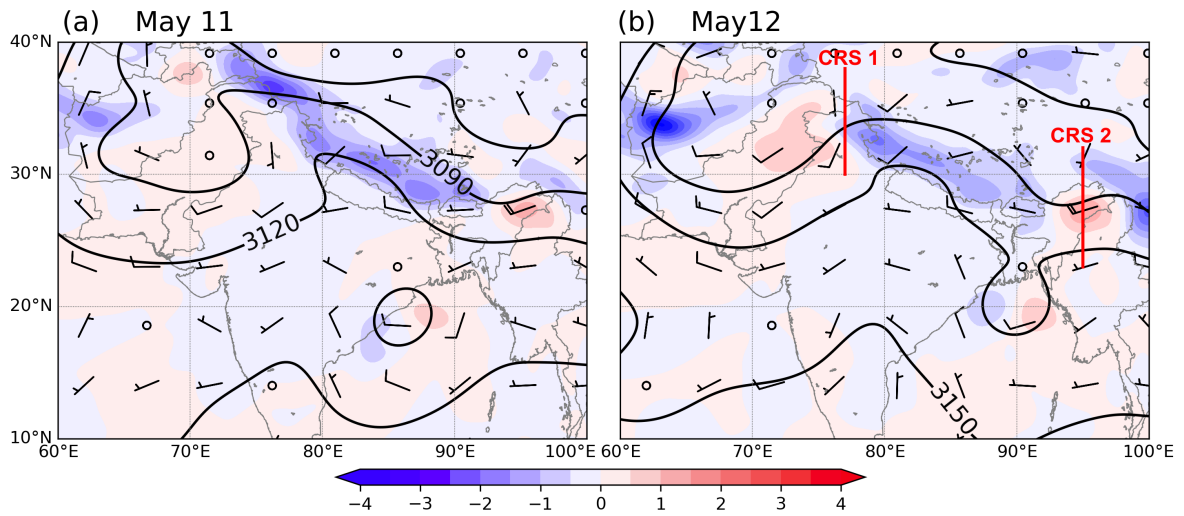


Figure 2.8. 700 hPa average temperature advection ($^{\circ}\text{C}/\text{h}$), geopotential height (m), and wind (barbs, full barb = 10m/s) for (a) May 11 and (b) May 12 (Source: WRF simulations).

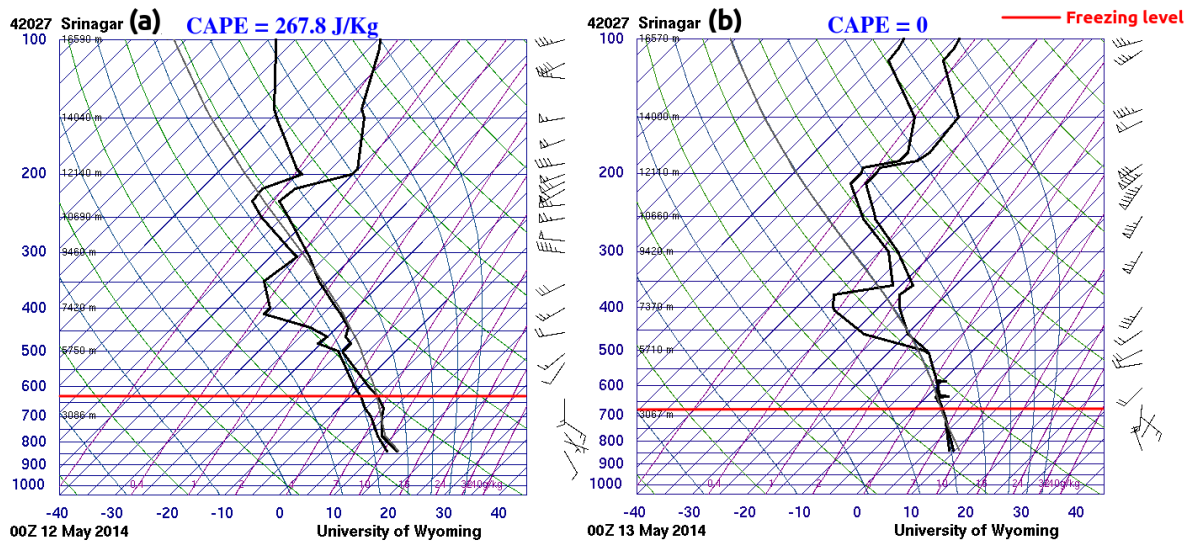


Figure 2.9. Skew-T log-P diagram for Shreenagar station on (a) 00Z May 12, 2014 and (b) 00Z May 13, 2014 (Source: University of Wyoming).

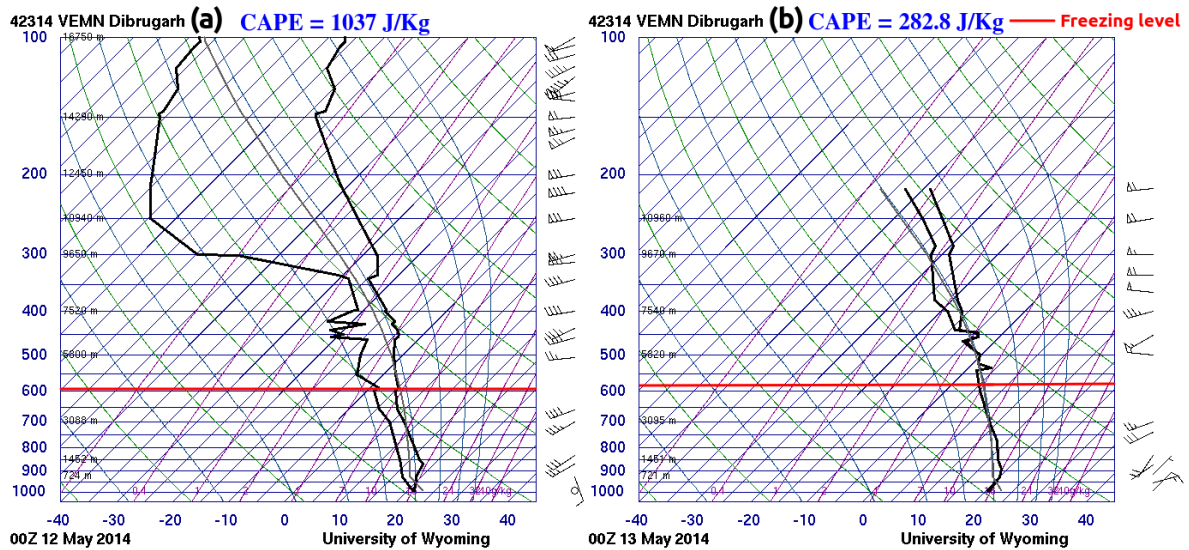


Figure 2.10. Skew-T log-P diagram for Dibrugarh station on (a) 00Z May 12, 2014 and (b) 00Z May 13, 2014 (Source: University of Wyoming).

flowing along the southern margin of the Himalaya. The low-level air flowing from the Bay of Bengal is uplifted by the hills of east India and condenses its moisture in a band of precipitation extending from the Bay of Bengal to the EHN (c.f. Figs. 2.7a, b, c, d, and e).

The height of freezing level being associated with temperature advection plays an important role in determining the type of precipitation falling on the surface. Due to the lower freezing level, solid precipitation is present at an altitude below 2 Km over the western Himalaya (Fig. 2.11a). On the other hand, the eastern Himalaya experiencing warm temperature advection and thus higher freezing level display rainfall even at an elevation above 4 Km (Fig. 2.11b).

2.4.3 Case II: Blocking event (February 1 to February 11, 2012)

Another typical blocking pattern (a dipole (Rex) block) formed over the Ural-Siberian region during the winter of 2012. It lasted for 11 days and produced widespread precipitation over the entire Himalaya.

Synoptic Conditions

The geopotential height anomaly at 200 hPa during this blocking event displays a strong ridge over Eurasia and a trough extending from Kazakhstan to the Arabian Sea, with its zonal extent from the Middle East to the Western Himalaya (Fig. 2.12). Furthermore, the height field also shows the presence of weak ridges on either side of the trough. The anomalous wind field exhibits the transport of mid-latitude air towards the tropics along the upstream portion of the trough and the transport of tropical air towards the mid-latitudes along the

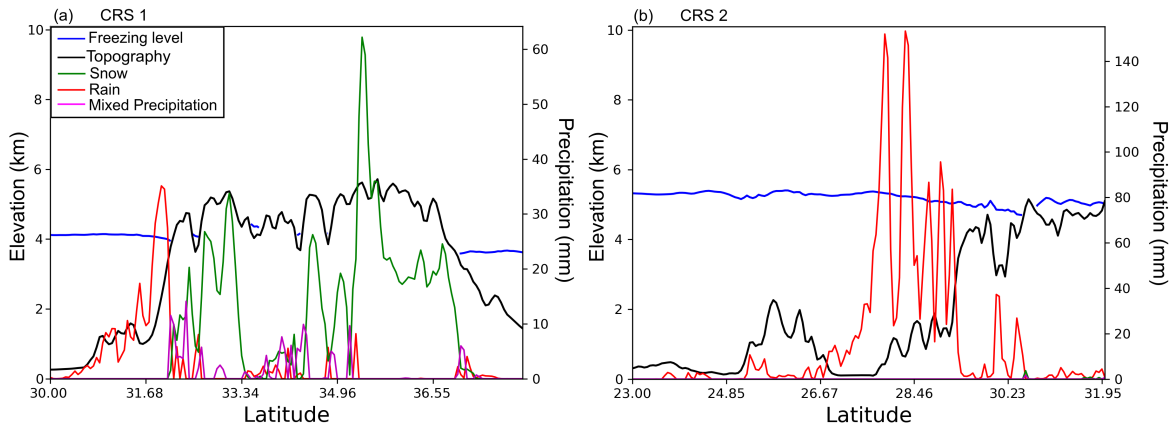


Figure 2.11. Cross section of daily accumulated precipitation (rain, snow and mixed precipitation), average freezing level and elevation along the red lines ((a) CRS1 and (b) CRS2) shown in Fig. 2.8b on May 12, 2014 (Source: WRF simulations).

downstream portion of the trough (Figs. 2.12e and f).

The anomalous MSLP field during the blocking event exhibits positive anomalies over Eurasia with 850 hPa anticyclonic flow (Figs. 2.13a, b, c, and d). A tongue of positive MSLP anomaly extends southward over the Middle East due to the large scale sinking of cold air from mid-latitudes along the upstream portion of the block. There are two regions of negative MSLP anomalies on either side of this tongue: the western anomaly lies over the Mediterranean region, while the eastern anomaly lies over the western Himalaya and the Tian Shan Mountains. Thus, anomalous high pressure on the north-west side (west of Afghanistan) and low pressure on the south-east side (over the Indo-Pakistan border and the western Himalaya) forces the 850 hPa horizontal winds to converge over the WHN. Furthermore, due to anomalously low MSLP over the Himalaya on February 7 and 8, the 850 hPa winds from both the Arabian Sea and the Bay of Bengal converge towards the central Himalaya (Figs. 2.13e and f).

PV on the 350 K isentropic surface displays higher PV air circulating cyclonically towards the tropics (Figs. 2.14a, b, c). Similar to the anomalies associated with the Ω block, the vertical cross-section of PV displays a strong tropopause fold with higher PV air descending to about 5000 m above MSL (Figs. 2.14d, e, and f).

WRF simulation of the atmospheric condition over the Himalaya during the dipole blocking event

The dipole blocking event is marked by strong precipitation over the entire Himalaya. WRF simulates the accumulation of both rain and snow over the southern slopes of the mountains in the Himalayan range (Fig. 2.15a and b). In particular, the higher elevations in the Himalaya receive snowfall while lower elevations receive rainfall, and the magnitude of snowfall is twice the magnitude of rainfall. The spatial distribution of precipitation indicates that the model simulation is consistent with TRMM data (Fig. 2.15a and c).

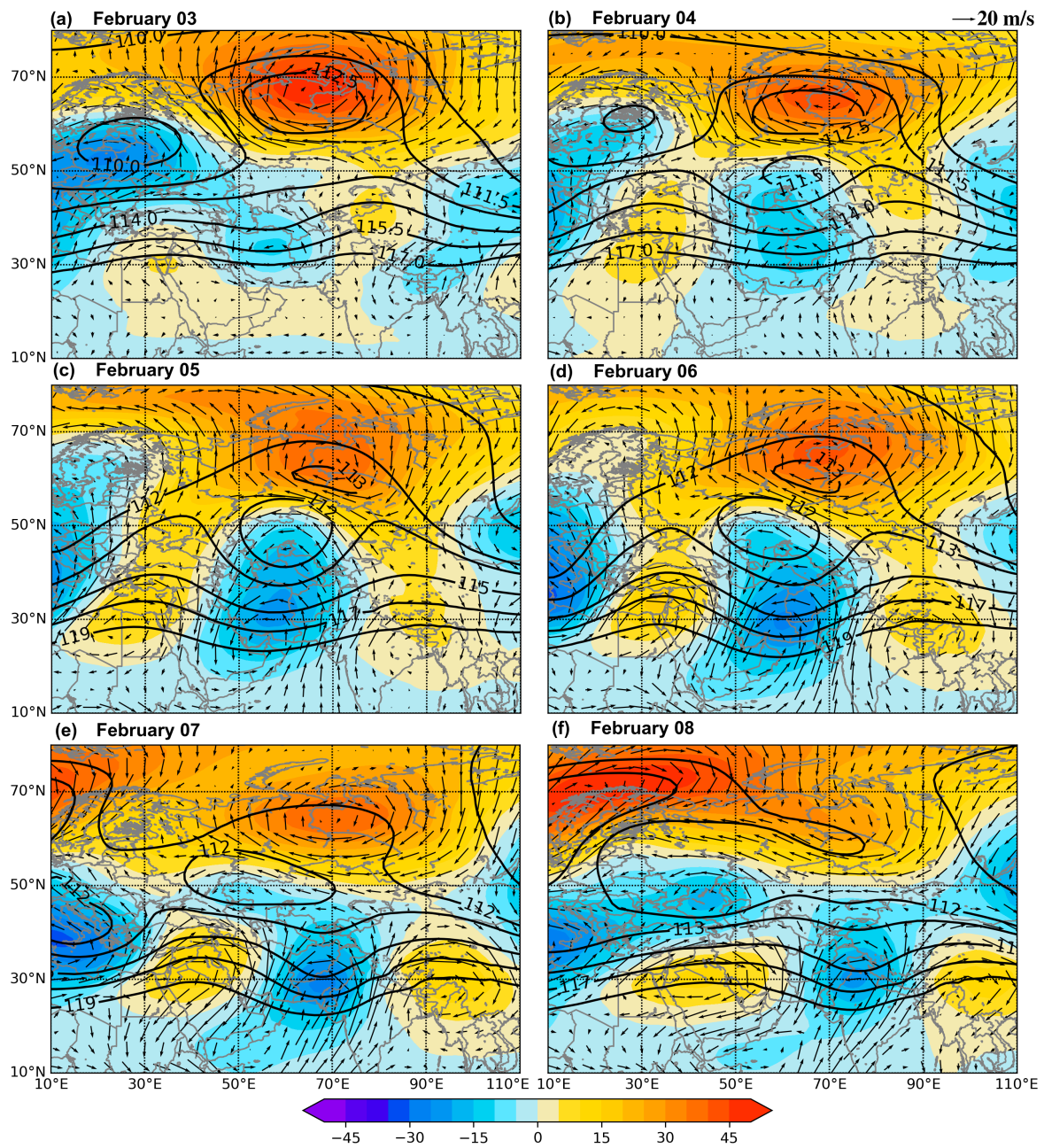


Figure 2.12. Daily 200 hPa geopotential height anomalies (shaded, m), geopotential height (contour, hectometer) and anomalous horizontal wind (vector, m/s) on (a) Feb 03, (b) Feb 04, (c) Feb 05, (d) Feb 06, (e) Feb 07, and (f) Feb 08, 2012 (Source: ERA-Interim reanalysis).

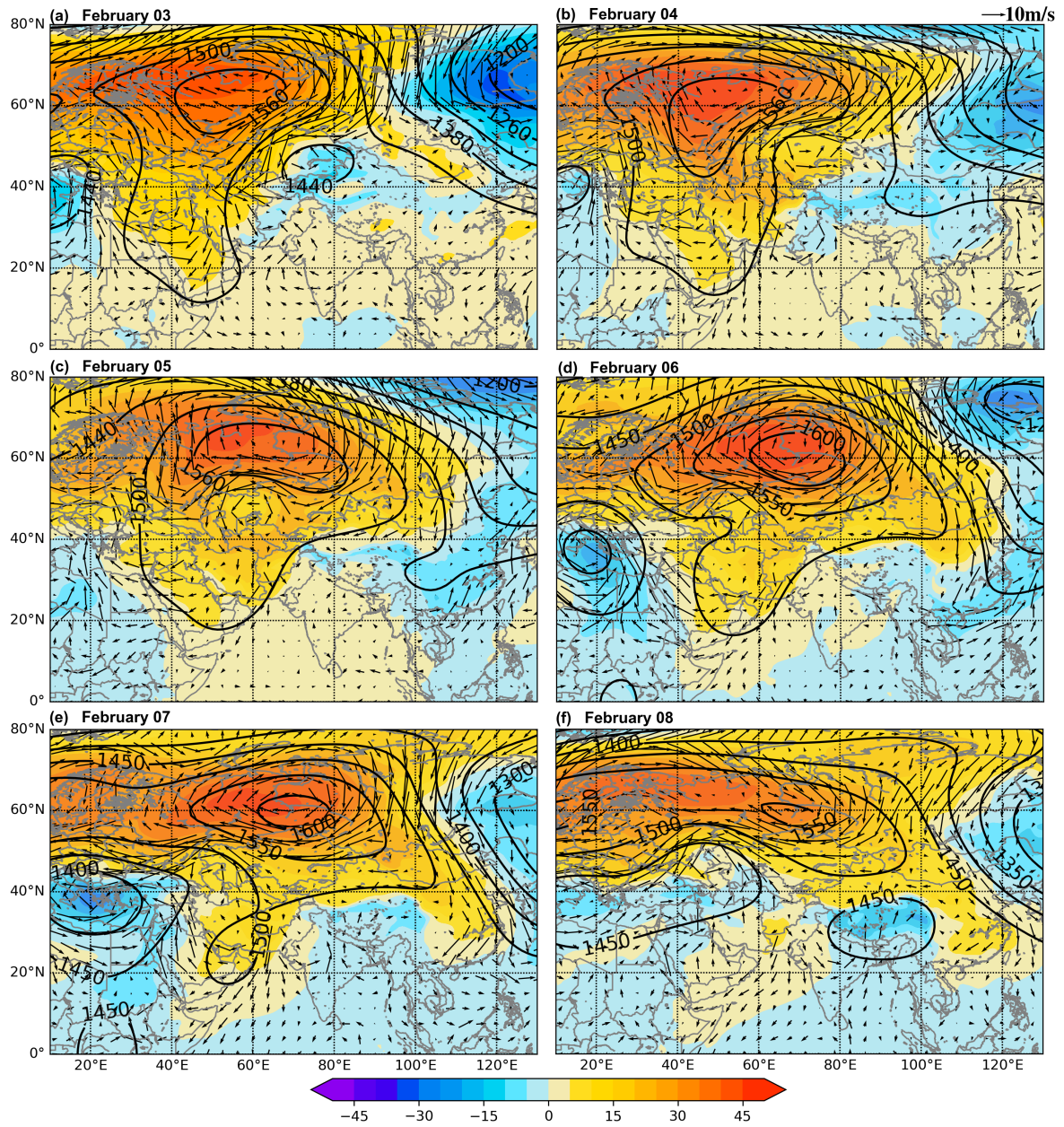


Figure 2.13. Daily mean sea level pressure anomalies (shaded, hPa), 850 hPa geopotential height (contour, m) and 850 hPa anomalous wind (vector, m/s) on (a) February 03, (b) February 04, (c) February 05, (d) February 06, (e) February 07, and (f) February 08, 2012 (Source: ERA-Interim reanalysis).

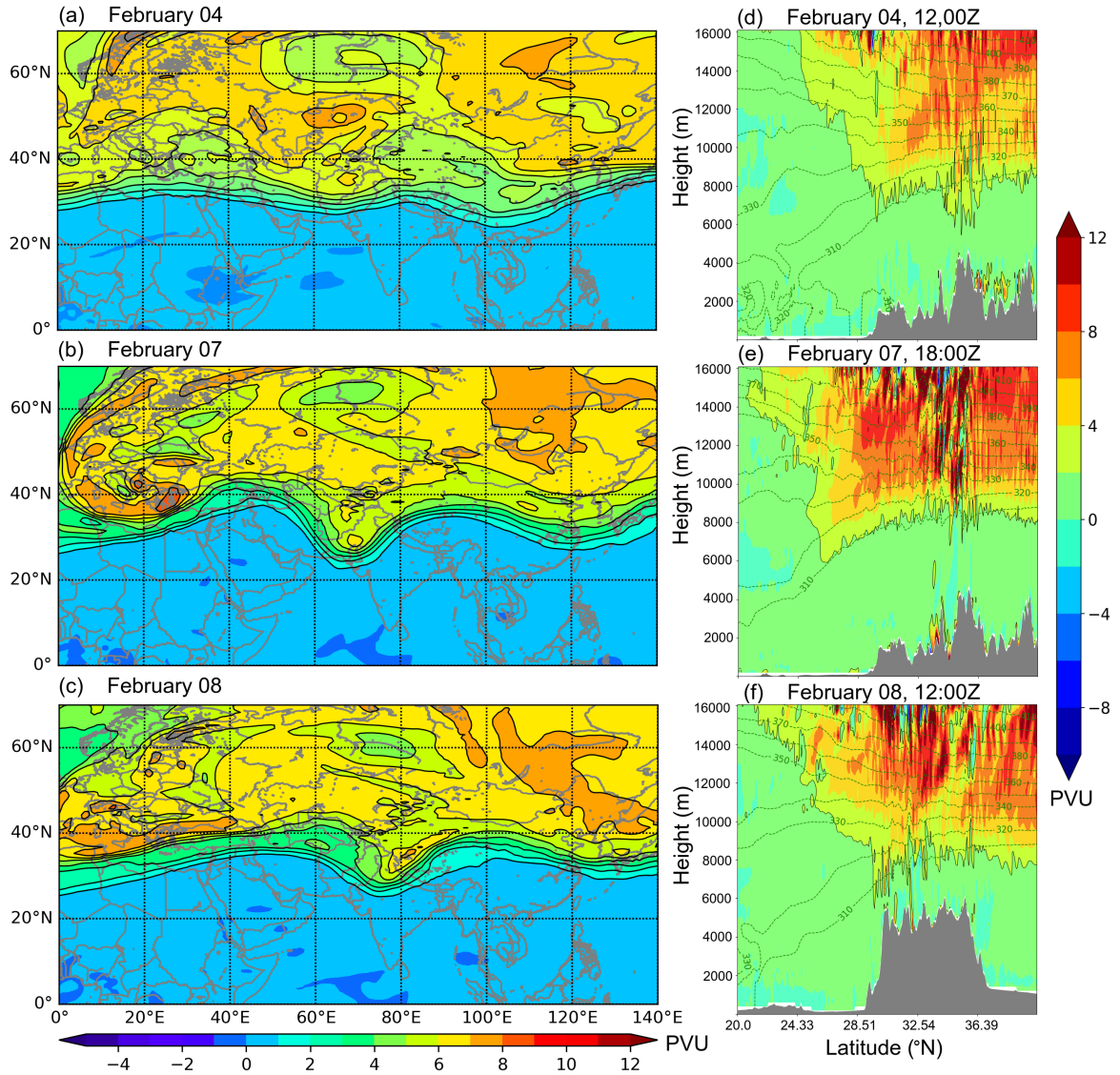


Figure 2.14. Daily PV (PVU) on 350 K isentropic surface on (a) February 04, (b) February 07, (c) February 08, 2012, PV ≥ 1 PVU are contoured (Source: ERA-Interim reanalysis); vertical cross section of simulated PV (shaded) and potential temperature (θ , green contour) on (d) February 04, 12:00Z, (e) February 07, 18:00Z, and (f) February 08, 12:00Z, (d and e across 700E longitude, and f across 800E longitude, d, e, f are plotted from WRF simulations).

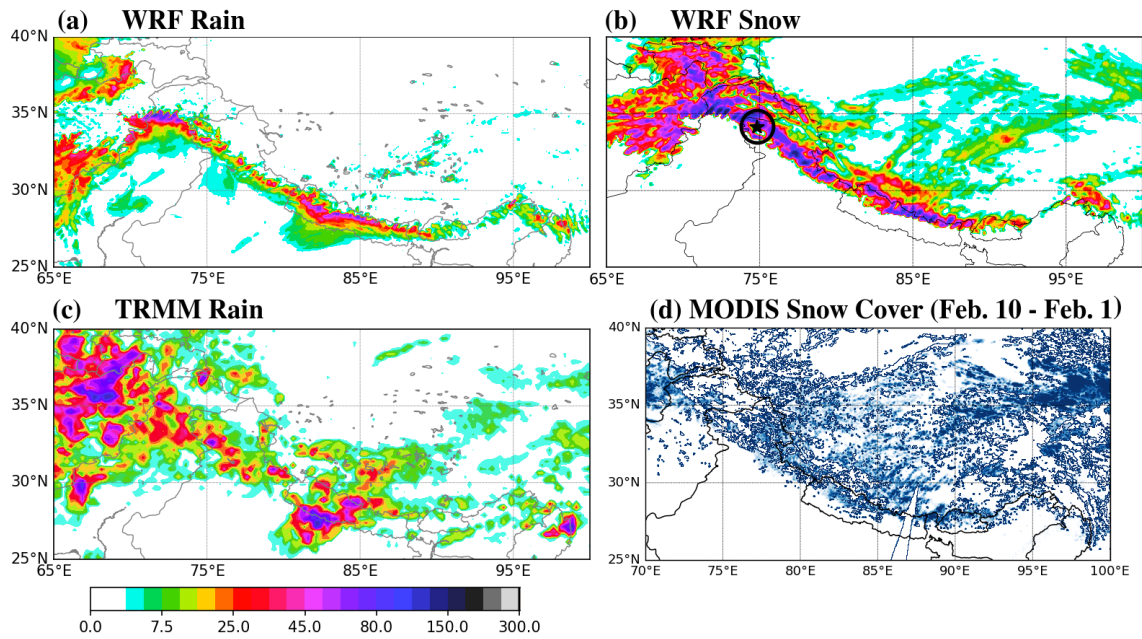


Figure 2.15. (a) WRF rainfall, (b) WRF snowfall, and (c) TRMM precipitation accumulated over 1-9 February 2012; (d) MODIS snow cover difference between February 10 and February 1. Location of Srinagar upper air station is represented by a black star enclosed within a black circle in (b).

The MODIS Terra snow cover product over the Himalaya on February 1 and February 10 displays a considerable increase in snow cover along the Himalayan arc during the simulated time period (Fig. 2.15d). However, MODIS data do not show significant snow cover over the eastern Himalaya close to the border of India, Myanmar, and China. Reasons behind this discrepancy could be a thick cloud cover over that region or WRF simulating snowfall, though rainfall occurs in reality.

Analysis of daily WRF precipitation from February 4 to February 8 indicates southward movement of the precipitating system from the western Himalaya towards the central and the eastern Himalaya (Fig. 2.16a, b, c, d, and e). On February 4, the downstream portion of the low-pressure component of the dipole block lies over the western Himalaya (close to the border of Afghanistan and Pakistan, c.f. Fig. 2.12b), and causes winds to converge on the WHN resulting in strong precipitation over the windward side of the western Himalaya. The topography of the Himalaya steers the movement of the precipitating low-pressure system southward along the Himalayan arc. On February 7, the deep low-pressure trough spans 40°N to 25°N and causes strong moisture convergence over the Arabian Sea and directs the winds towards the central Himalaya (c.f. Fig. 2.12e), leading to strong precipitation over the Annapurna and Dhaulagiri Range in western Nepal. The slight eastward shift of the depression from 70°E to 75°E on February 8 causes strong precipitation over the entire central Himalaya.

The VIMF during the blocking event reveals the tropical water bodies (the Arabian Sea and the Indian Ocean) as the main sources of moisture for the precipitation along the Himalayan arc (Figs. 2.16f, g, h, i and j).

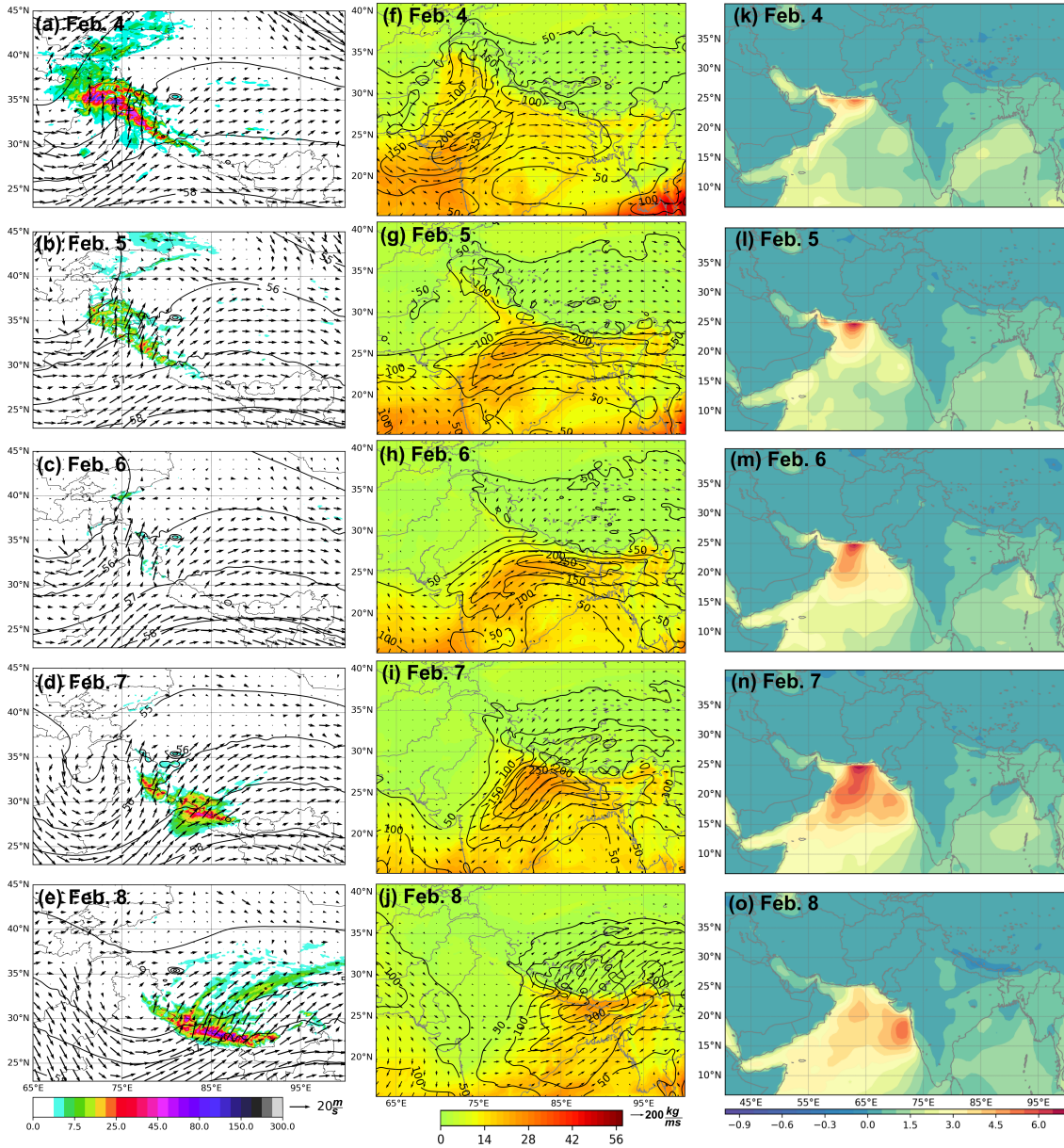


Figure 2.16. (a), (b), (c), (d), and (e) daily accumulated precipitation (shaded, mm), 500 hPa geopotential height (contour, hectometer), 700 hPa wind (vector, m/s) from WRF simulations; (f), (g), (h), (i), and (j) precipitable water (shaded, mm), vertically integrated moisture flux (vector indicating direction and contour indicating magnitude, $\text{kg m}^{-1} \text{s}^{-1}$) computed from WRF simulations, and (k), (l), (m), (n) and (o) ERA-Interim surface evaporation (m of water) for February 4, 5, 6, 7, and 8 respectively.

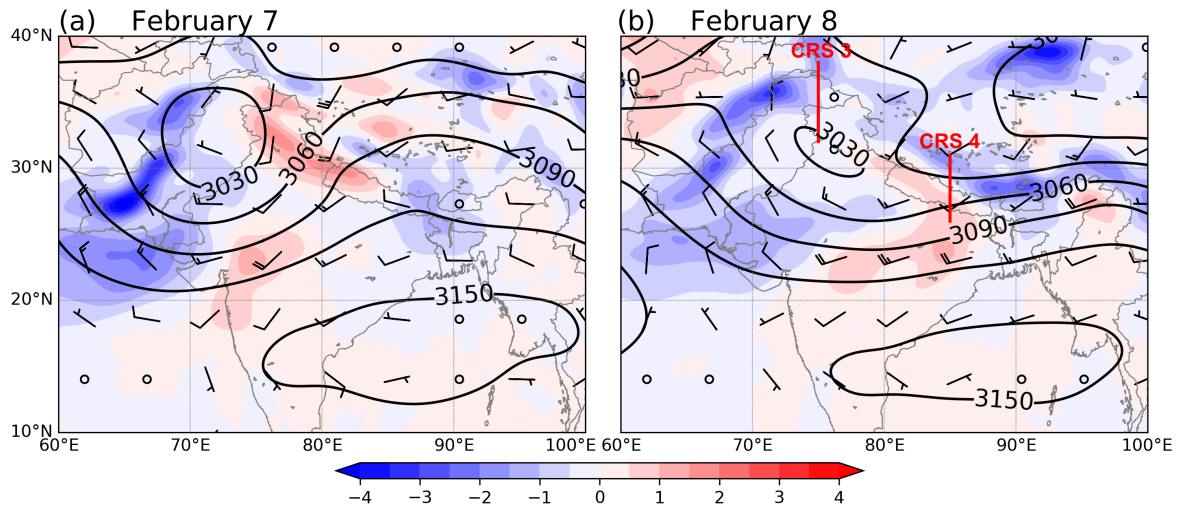


Figure 2.17. 700 hPa average temperature advection ($^{\circ}\text{C}/\text{h}$), geopotential height (m), and wind (barbs, full barb = 10m/s) for (a) February 7 and (b) February 8 (Source: WRF simulations).

The locations of higher values of total precipitable water and VIMF are consistent with the locations of strong precipitation. Thus, the cyclonic component of the dipole block promotes strong moisture transport from the tropical water bodies towards the Himalaya as evident from Era-Interim surface evaporation (Figs. 2.16k, l, m, n, o), which indicates high evaporation over the Arabian Sea during the blocking event. The Arabian Sea lies at the frontal boundary of the cold front formed by the southward advancing cold air. This cold front pushes warm-moist subtropical air towards the Himalaya (Fig. 2.17).

The vertical temperature profile of the atmosphere during the blocking event shows the presence of a thick mid-tropospheric moist layer. The atmospheric sounding (Skew-T diagram) from the Srinagar station on February 03-03Z shows a dry layer between the surface and 650 hPa and an overlying moist layer up to 350 hPa (Fig. 2.18a). The absence of CAPE on February 3 implies topographic lifting as the only mechanism for the air parcel to precipitate. Furthermore, the surface temperature in the Skew-T diagram is below freezing level due to the cold advection associated with the block, so the Srinagar station (elevation 1587 m amsl) and its surroundings receive solid precipitation (cf. Figs. 2.15b).

There is widespread precipitation over the central Himalaya on February 7 and 8. The Gorakhpur station lies in the simulated moisture transport route. Like the Srinagar station sounding, the Gorakhpur station sounding (Fig. 2.18b) shows a thick mid-tropospheric moist layer with a dry layer below. The wind circulation in the lowest 100 hPa layer is from the south-east, while the blocking related south-westerlies flow above 900 hPa. The difference between the Srinagar and Gorakhpur soundings is that the surface temperature at Srinagar is below freezing, whereas at Gorakhpur the freezing level is at 660 hPa (~ 3000 m amsl). The higher freezing level at Gorakhpur is caused by the warm temperature advection associated with the block's wind circulation

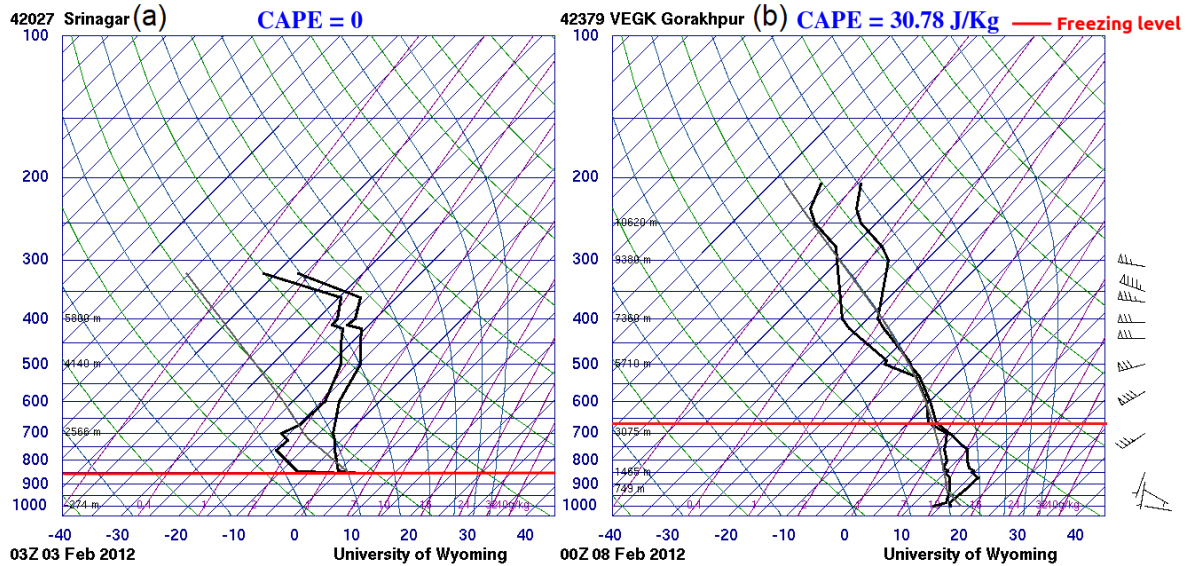


Figure 2.18. Skew-T log-P diagram for (a) Shreenagar station 03Z Feb 03, 2012 (observations obtained from the University of Wyoming), (b) Gorakhpur station 00Z Feb 08, 2012 (Source: University of Wyoming).

anomalies (c.f. Fig. 2.17).

Lower freezing level over the western Himalaya lead to peak snow accumulation over the ridge with elevation below 4 Km elevation, with snow accumulation observed below 2 Km (Fig. 2.19a). On the other hand, due to the higher freezing level, liquid precipitation is still observed at an elevation close to 4 Km (Fig. 2.19b). The peak snow accumulation over the central Himalaya is observed at an elevation around 5 Km, with small amount of rainfall still observed at an elevation above 5 Km.

2.5 Discussion and Conclusion

2.5.1 Discussion

The Ural-Siberian region is an important region for the formation of atmospheric blocks. We have presented two different, but characteristic, types of blocking events that form over the Ural-Siberian region, i.e., an Ω blocking event and a dipole blocking event. Although the structure and the season of occurrence of both the blocking events chosen are different, they are both associated with strong precipitation and varied precipitation types over the Himalaya that are anomalous to that season.

A comparison of tropospheric height and wind field anomalies between the two blocking events displays troughs with axes parallel to the Hindu Kush Mountains, penetrating southward to the Arabian Sea in both cases. The combination of the mid-latitude ridge and subtropical troughs enhance meridional wind flows. This generates southward advection of cold mid-latitude air in both blocking events. The advected upper tropospheric

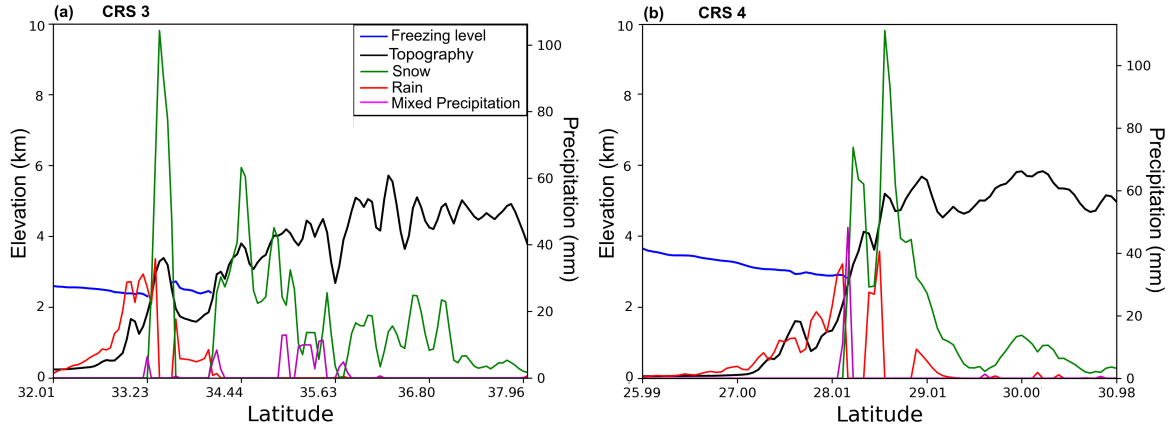


Figure 2.19. Cross section of daily accumulated precipitation (rain, snow and mixed precipitation), average freezing level and elevation along the red lines ((a) CRS 3, February 4, 2012 and (b) CRS 4, February 8, 2012) shown in Fig. 2.17b (Source: WRF simulations).

air subsides over the region from the Arabian Peninsula to South Asia, increasing the surface pressure.

Another feature associated with both blocking events is the equatorward protrusion of high PV air. The vertical cross-sections of PV in both cases display high PV air descending to 5000 m asl showing strong tropopause folding. There is an air mass exchange between troposphere and stratosphere associated with tropopause folds, leading to high ozone concentrations over the ridges of Himalayan Mountains (Bracci et al., 2012; Ojha et al., 2017). Furthermore, Bracci et al. (2012) performed back trajectory analysis associated with the high-ozone concentration measured at the Pyramid station near the Everest base camp and identified the high-ozone concentration trajectory as coming from the northern Eurasia (around the Ural-Siberian region).

During the Ω block, the upper-tropospheric trough induces convergence of ageostrophic winds upstream and divergence downstream. Thus, upper-level convergence occurs over the Arabian Peninsula, while divergence occurs over the Indo-Pakistan border extending all the way to the WHN. The convergence of ageostrophic winds over central Afghanistan and the Arabian Peninsula triggers the subsidence of cold mid-latitude air (cf., section 2.4.2), while the divergence over the WHN drives the upward flow of air causing negative pressure anomalies and convergent, moisture-laden low-level westerly flow towards the WHN and precipitation over the mountains with a type determined by the local freezing level.

Similar to the Ω block, the dipole block initially induces convergence of ageostrophic winds in the upper troposphere over the Middle East and divergence over the Indo-Pakistan region. However, at the later stage, the upper-tropospheric convergence shifts over the region extending from the Middle East to north-western India and the divergence shifts over the central and western Himalaya. Thus, subsidence of cold mid-latitude air occurs over the Middle East and north-western India, and the vertical ascent of warm-moist air occurs over the Gangetic Plain and the foothills of the central Himalaya.

Precipitation is mainly concentrated over the western and eastern Himalayan notches during the Ω blocking event, while the entire Himalayan arc receives precipitation during the dipole blocking event. The Ω blocking event is observed during the month of May (spring/pre-monsoon) which is close to the date of onset of the summer monsoon in South Asia. Strong convection near the Bay of Bengal is common in the pre-monsoon season (Virts and Houze, 2016) and the anomalous low-level westerlies associated with the block advect the moisture eastward and eventually produce precipitation over Bangladesh, Myanmar and north-east India (cf. Figs. 2.6a and c). The analysis of VIMF suggests the moist flow from the Arabian Sea is the main source of moisture for the precipitation around the WHN, while the EHN gets moisture from both the Arabian Sea and the Bay of Bengal. Moisture transport from the Arabian Sea to the eastern Himalayan notch is anomalous and related to the dynamics of the subtropical trough portion of the block west of the Hindu Kush Mountains.

Likewise, the analysis of VIMF during the dipole block shows the moisture flux converging from the Arabian Sea to the WHN. However, as the trough deepens and extends southward over time, moisture transport concentrates over the central Himalaya generating strong widespread precipitation. Norris et al. (2015) simulated two winter precipitation events over the Himalaya, using the WRF model, and observed widespread precipitation over the entire Himalayan arc on one of their simulations (from March 9 to 16, 2006). Though their study is not related to the upper atmospheric blocks, their simulations also show the evolution of two cyclones over an 8-day period that triggered widespread precipitation over the entire Himalayan arc. Thus, southward extension of the low-pressure trough is important to generate precipitation over the central and the eastern Himalaya.

The freezing level in both the blocking events drops/rises depending on cold/warm advection generated by the block and plays an important role in determining the type of precipitation at different elevations. For example, a lowered freezing level due to cold advection over the western Himalaya during the Ω block resulted in frozen precipitation at lower elevations, while an elevated freezing level due to warm advection over the central Himalaya during the dipole block resulted in liquid precipitation at higher elevations.

2.5.2 Conclusion

This study has presented the anomalous weather conditions over the Himalaya during two different blocking events (an Ω blocking event and a dipole blocking event) in the Ural-Siberian region using the simulated output from the WRF model. The analysis of synoptic conditions during both the blocking events reveal the cyclonic component of the block as a driver for the anomalous weather conditions over the Himalaya. The convergence and divergence of ageostrophic winds along the upstream and downstream portion of the upper-level trough cause subsidence of cold mid-latitude air along the upstream portion and ascent of warm subtropical air along the downstream portion. This creates high surface pressure over the Arabian Peninsula and the Middle East, and

local pressure deficit over South Asia. They also create tropopause folds characterized by equatorward protrusions of high PV stratospheric air that descend into tropospheric elevations. Over high topographic elevations such as the Himalaya, the likelihood of such folding events, and hence stratospheric air, reaching the surface is significantly increased.

Simulated precipitation in both cases compares favorably with the TRMM dataset and the MODIS snow-cover product (as observations). The spatial distribution of precipitation during the Ω block is limited to the eastern and western Himalayan notches, while there is widespread precipitation during the dipole blocking event.

Our study shows that Ural-Siberian blocks are important perturbations in the upper atmosphere that generate strong precipitation events over the Himalaya, of both rain and snow, and hence are likely to play a role in the mass balance of Himalayan glaciers. Any change in frequency and intensity of blocks due to climate change, as well as changes in the freezing levels associated with these blocks, will therefore be a factor to consider in determining the future mass balance of Himalayan glaciers, and remains a subject for future research.

2.6 Acknowledgments

The ERA-Interim data are produced by the European Center for Medium Range Weather Forecasts (ECMWF). The TRMM satellite rainfall data are produced as a joint project of NASA and Japan Aerospace Exploration Agency. MODIS Terra Snow Cover Products are produced by NASA National Snow and Ice Data Center. The observed sounding data were obtained from the Department of Atmospheric Science, University of Wyoming. All above mentioned data are freely downloadable. The high-performance computing were done on Compute Canada Clusters. ABGB acknowledges support from the Natural Sciences and Engineering Research Council of Canada.

References

- Andermann, C., Bonnet, S., and Gloaguen, R. (2011). Evaluation of precipitation data sets along the Himalayan front. *Geochemistry, Geophysics, Geosystems*, 12(7).
- Barriopedro, D., García-Herrera, R., Lupo, A. R., and Hernández, E. (2006). A climatology of Northern Hemisphere blocking. *Journal of Climate*, 19(6):1042–1063.
- Bharti, V. and Singh, C. (2015). Evaluation of error in TRMM 3b42v7 precipitation estimates over the Himalayan region. *Journal of Geophysical Research: Atmospheres*, 120(24):12458–12473.
- Bracci, A., Cristofanelli, P., Sprenger, M., Bonaf, U., Calzolari, F., Duchi, R., Laj, P., Marinoni, A., Roccató, F., Vuillermoz, E., and Bonasoni, P. (2012). Transport of stratospheric air masses to the Nepal Climate ObservatoryPyramid (Himalaya; 5079 m msl): A synoptic-scale investigation. *Journal of Applied Meteorology and Climatology*, 51(8):1489–1507.
- Brunner, L., Hegerl, G. C., and Steiner, A. K. (2017). Connecting atmospheric blocking to European temperature extremes in spring. *Journal of Climate*, 30(2):585–594.
- Cannon, F., Carvalho, L. M., Jones, C., and Bookhagen, B. (2014). Multi-annual variations in winter westerly disturbance activity affecting the Himalaya. *Climate Dynamics*, 44(1-2):441–455.
- Carrera, M. L., Higgins, R. W., and Kousky, V. E. (2004). Downstream weather impacts associated with atmospheric blocking over the Northeast Pacific. *Journal of Climate*, 17(24):4823–4839.
- Casola, J. H. and Wallace, J. M. (2007). Identifying weather regimes in the wintertime 500-hPa geopotential height field for the Pacific-North American sector using a limited-contour clustering technique. *Journal of Applied Meteorology and Climatology*, 46(10):1619–1630.
- Cheung, H. N., Zhou, W., Mok, H. Y., and Wu, M. C. (2012). Relationship between Ural-Siberian Blocking and the East Asian winter monsoon in relation to the Arctic oscillation and the El Niño-Southern Oscillation. *Journal of Climate*, 25(12):4242–4257.
- Cheung, H. N., Zhou, W., Mok, H. Y., Wu, M. C., and Shao, Y. (2013a). Revisiting the climatology of atmospheric blocking in the Northern Hemisphere. *Advances in Atmospheric Sciences*, 30(2):397–410.
- Cheung, H. N., Zhou, W., Shao, Y., Chen, W., Mok, H. Y., and Wu, M. C. (2013b). Observational climatology and characteristics of wintertime atmospheric blocking over Ural-Siberia. *Climate Dynamics*, 41(1):63–79.

- Dee, D. P., Uppala, S. M., Simmons, A. J., Berrisford, P., Poli, P., Kobayashi, S., Andrae, U., Balmaseda, M. A., Balsamo, G., Bauer, P., Bechtold, P., Beljaars, A. C. M., van de Berg, L., Bidlot, J., Bormann, N., Delsol, C., Dragani, R., Fuentes, M., Geer, A. J., Haimberger, L., Healy, S. B., Hersbach, H., Hlm, E. V., Isaksen, L., Kllberg, P., Khler, M., Matricardi, M., McNally, A. P., Monge-Sanz, B. M., Morcrette, J.-J., Park, B.-K., Peubey, C., de Rosnay, P., Tavolato, C., Thpaut, J.-N., and Vitart, F. (2011). The era-interim reanalysis: configuration and performance of the data assimilation system. *Quarterly Journal of the Royal Meteorological Society*, 137(656):553–597.
- Huffman, G. J., Adler, R. F., Bolvin, D. T., and Nelkin, E. J. (2010). *The TRMM Multi-Satellite Precipitation Analysis (TMPA)*, pages 3–22. Springer Netherlands, Dordrecht.
- Jiménez, P. A., Dudhia, J., Gonzalez-Rouco, J. F., Navarro, J., Montvez, J. P., and Garca-Bustamante, E. (2012). A revised scheme for the WRF surface layer formulation. *Monthly Weather Review*, 140(3):898–918.
- Kain, J. S. (2004). The KainFritsch convective parameterization: An update. *Journal of Applied Meteorology*, 43(1):170–181.
- Karki, R., Ul Hasson, S., Gerlitz, L., Schickhoff, U., Scholten, T., and Bøhner, J. (2017). Quantifying the added value of convection-permitting climate simulations in complex terrain: A systematic evaluation of WRF over the Himalayas. *Earth System Dynamics*, 8(3):507–528.
- LANG, T. J. and BARROS, A. P. (2004). Winter Storms in the Central Himalayas. *Journal of the Meteorological Society of Japan*, 82(3):829–844.
- Lau, W. K. M. and Kim, K.-M. (2012). The 2010 Pakistan flood and Russian heat wave: Teleconnection of hydrometeorological extremes. *Journal of Hydrometeorology*, 13(1):392–403.
- Lejenäs, H. and Økland, H. (1983). Characteristics of northern hemisphere blocking as determined from a long time series of observational data. *Tellus A*, 35A(5):350–362.
- Medina, S., Houze, R. A., Kumar, A., and Niyogi, D. (2010). Summer monsoon convection in the Himalayan region: Terrain and land cover effects. *Quarterly Journal of the Royal Meteorological Society*, 136(648):593–616.
- Nakanishi, M. and Niino, H. (2006). An improved Mellor-Yamada level-3 model: Its numerical stability and application to a regional prediction of advection fog. *Boundary-Layer Meteorology*, 119(2):397–407.
- Nakanishi, M. and Niino, H. (2009). Development of an improved turbulence closure model for the atmospheric boundary layer. *Journal of the Meteorological Society of Japan. Ser. II*, 87(5):895–912.

- Niu, G.-Y., Yang, Z.-L., Mitchell, K. E., Chen, F., Ek, M. B., Barlage, M., Kumar, A., Manning, K., Niyogi, D., Rosero, E., Tewari, M., and Xia, Y. (2011). The community NOAA land surface model with multiparameterization options (NOAH-MP): 1. model description and evaluation with local-scale measurements. *Journal of Geophysical Research: Atmospheres*, 116(D12).
- Norris, J., Carvalho, L. M., Jones, C., and Cannon, F. (2015). WRF simulations of two extreme snowfall events associated with contrasting extratropical cyclones over the western and central Himalaya. *Journal of Geophysical Research*, 120(8):3114–3138.
- Ojha, N., Pozzer, A., Akritidis, D., and Lelieveld, J. (2017). Secondary ozone peaks in the troposphere over the Himalayas. *Atmospheric Chemistry and Physics*, 17(11):6743–6757.
- Park, Y.-J. and An, J.-B. (2014). Characteristics of atmospheric circulation over East Asia associated with summer blocking. *Journal of Geophysical Research Atmospheres*, 119(2):726–738.
- Pelly, J. L. and Hoskins, B. J. (2003). A New Perspective on Blocking. *Journal of the Atmospheric Sciences*, 60(5):743–755.
- Pook, M. J., Risbey, J. S., McIntosh, P. C., Ummenhofer, C. C., Marshall, A. G., and Meyers, G. A. (2013). The Seasonal Cycle of Blocking and Associated Physical Mechanisms in the Australian Region and Relationship with Rainfall. *American Meteorological Society*, 141(12):4534–4553.
- Postel, G. A. and Hitchman, M. H. (1999). A climatology of Rossby wave breaking along the subtropical tropopause. *Journal of the Atmospheric Sciences*, 56(3):359–373.
- Rex, D. F. (1950). Blocking action in the middle troposphere and its effect upon regional climate. *Tellus*, 2(3):196–211.
- Takaya, K. and Nakamura, H. (2005). Geographical dependence of upper-level blocking formation associated with intraseasonal amplification of the Siberian high. *Journal of the atmospheric sciences*, pages 4441–4449.
- Thompson, G., Field, P. R., Rasmussen, R. M., and Hall, W. D. (2008). Explicit forecasts of winter precipitation using an improved bulk microphysics scheme. part ii: Implementation of a new snow parameterization. *Monthly Weather Review*, 136(12):5095–5115.
- Tibaldi, S. and Molteni, F. (1990). On the operational predictability of blocking. *Tellus A*, 42(3):343–365.
- Tyrlis, E. and Hoskins, B. J. (2008). The Morphology of Northern Hemisphere Blocking. *Journal of the Atmospheric Sciences*, 65(5):1653–1665.

- Vellore, R. K., Kaplan, M. L., Krishnan, R., Lewis, J. M., Sabade, S., Deshpande, N., Singh, B. B., Madhura, R. K., and Rama Rao, M. V. (2016). Monsoon-extratropical circulation interactions in Himalayan extreme rainfall. *Climate Dynamics*, 46(11-12):3517–3546.
- Virts, K. S. and Houze, R. A. (2016). Seasonal and Intraseasonal Variability of Mesoscale Convective Systems over the South Asian Monsoon Region. *Journal of the Atmospheric Sciences*, 73(12):4753–4774.
- Yang, Z.-L., Niu, G.-Y., Mitchell, K. E., Chen, F., Ek, M. B., Barlage, M., Longuevergne, L., Manning, K., Niyogi, D., Tewari, M., and Xia, Y. (2011). The community NOAA land surface model with multiparameterization options (NOAH-MP): 2. evaluation over global river basins. *Journal of Geophysical Research: Atmospheres*, 116(D12).
- Zhou, W., Chan, J. C. L., Chen, W., Ling, J., Pinto, J. G., and Shao, Y. (2009). Synoptic-Scale Controls of Persistent Low Temperature and Icy Weather over Southern China in January 2008. *Monthly Weather Review*, 137(11):3978–3991.

Chapter 3

Sensitivity Tests of Microphysics Schemes in WRF: A Case Study of a Flood-Producing Precipitation Event over Nepal

Planned to submit July 2019 to *Journal of Atmospheric Research*

U. Tiwari and A.B.G. Bush

3.1 Abstract

Floods and landslides are common natural disasters during the monsoon season in Nepal. Strong precipitation during August 2017 triggered widespread flooding over the southern part of the country that caused more than a hundred casualties and affected more than a million people directly, leading to great economic loss. In this study, we perform sensitivity analyses of seven different cloud microphysics schemes (Lin, WSM6, WDM6, Goddard, Morrison, Thompson, and Milbrandt) used in the Weather Research and Forecasting (WRF) model to simulate precipitation over Nepal during 8-20 August 2017. We configure WRF with two nested domains of 15 km (D1) and 3 km (D2) horizontal resolutions and force it with ERA-Interim ($0.75^{\circ} \times 0.75^{\circ}$ horizontal resolution) and NCEP ($1^{\circ} \times 1^{\circ}$ horizontal resolution) data. The simulated precipitation is evaluated against station observations obtained from the Department of Hydrology and Meteorology (DHM), Nepal. Our study

indicates that most of the schemes are able to capture the spatial distribution of precipitation over the southern plains (Terai region) of Nepal. However, only two of them (Morrison and WDM6) are able to simulate the precipitation over both the southern plains and the higher mountains. Moreover, the WDM6 scheme with its cumulus parameterization turned on best represents both spatial and temporal distributions of precipitation over the simulation period. The comparison between NCEP and ERA-Interim simulations suggest that the use of ERA-Interim data slightly improves the output of the simulation when compared with the observational data. Results also indicate that for simulations in mountainous regions, retaining the cumulus parameterization in the microphysics scheme down to at least 3 Km spatial resolution produces more accurate precipitation results.

3.2 Introduction

Floods and landslides are the most common natural disasters in Nepal during the summer monsoon season. According to Pokhrel et al. (2009), water-induced disasters in Nepal account for about 31.8% of the total annual loss of life and about 53.2 % of the total annual loss of properties. Intense and continuous precipitation during the monsoon season together with the extreme Himalayan topography result in such extreme disasters.

Synoptically, there are strong spatial and temporal variations in precipitation over Nepal. The total annual precipitation over central Nepal exceeds 3000 mm, while the northwestern mountains receive less than 1000 mm (Barros et al., 2000; Ichiyanagi et al., 2007; Lang and Barros, 2002; Shrestha, 2000). On average, Nepal receives about 80% of its total annual precipitation during the monsoon season, although this number varies spatially and has a maximum between the region extending from the Terai to the Middle mountains (below 2000 m above sea level (asl)) (Ichiyanagi et al., 2007; Kansakar et al., 2004; Shrestha, 2000).

Summer monsoon precipitation over Nepal is a result of the interaction between a low-level moist flow off tropical water bodies (the Bay of Bengal and the Arabian Sea) and the Himalayan topography. The topography along the Nepal Himalaya is quite unique among other regions in the Himalaya in that the mountains rise in elevation in two distinct steps. This two-step topography results in two significant rainfall peaks during the monsoon season (Shrestha et al., 2012). The first peak is observed along the Sub-Himalaya (elevation \sim 500 - 700 m asl) and the second peak is observed along the Lesser Himalaya (elevation \sim 2,000 - 2,200 m asl). The precipitation over the Lesser Himalaya is characterized by frequent but less intense stratiform precipitation, while the precipitation over the Sub-Himalaya is characterized by intense convective precipitation (Romatschke and Houze, 2011; Shrestha et al., 2012).

The 2017 flooding disaster in Nepal was caused by precipitation falling over the Sub-Himalaya (Bhandari et al., 2018), and unlike other flooding events (where large perennial rivers like Koshi, Gandaki, Karnali, etc. produce floods), the ephemeral rivers originating from the Sub-Himalaya produced a series of flash floods

inundating more than 80% of the total land area in the affected districts (MoHA, 2018). Thus, this event suggests that precipitation over the Sub-Himalaya (the first precipitation peak as explained by Shrestha et al. (2012) alone is capable of triggering such a flooding disaster.

In order to minimize the risks associated with water-induced disasters, early forecasting of extreme weather events is necessary. The Department of Hydrology and Meteorology (DHM), Nepal issues weather and flooding related forecasts in Nepal. Their weather forecasting system is based on the Weather Research and Forecasting (WRF) model (<http://www.mfd.gov.np/nwp/#/nwp/Model>). The WRF model is used worldwide for both numerical weather predictions and mesoscale atmospheric research. The use of WRF for the Himalayan region is also expanding (eg., (Bhomia et al., 2019; Chawla et al., 2018; Collier et al., 2014; Dimri and Chevuturi, 2014; Karki et al., 2017, 2018; Maussion et al., 2011; Medina et al., 2010; Norris et al., 2015; Orr et al., 2017; Regmi et al., 2017; Stigter et al., 2018; Vellore et al., 2016, 2014)).

In this study, we use WRF to simulate an extreme flood-producing precipitation event over Nepal and perform sensitivity tests of different cloud microphysics schemes (including the one used in the DHM's weather forecasting system) and forcing data to simulate the event during August 2017. Previous studies in the Himalaya have shown different microphysics schemes perform well in different events (Chawla et al., 2018; Karki et al., 2018; Orr et al., 2017; Shrestha et al., 2016; Tiwari et al., 2018). Those studies suggest that a single microphysics scheme is not sufficient to accurately simulate every disastrous precipitation event in the Himalaya. Since precipitation over the Sub-Himalaya is highly convective, we will explore how well the microphysics schemes perform at the convection permitting grid scale. Furthermore, we will explore how well the schemes work given the two-step topography across the Nepal Himalaya, which has not been included in any of the previous studies.

3.3 Materials and Methods

3.3.1 Description of the event

During the second week of August 2017, Nepal experienced one of the worst flooding disasters in 15 years which affected 35 southern districts. According to the Ministry of Home Affairs (MoHA, 2018), the total death toll during the 2017 monsoon was 160 with additional 70 people either missing or injured. Furthermore, around 1,688,474 people were directly affected by this disaster (NPC, 017c).

The average synoptic conditions near the surface during the flooding event (11-14 August) reveal the presence of low mean sea level pressure (mslp) along the Indo-Gangetic Plain, parallel to the Himalaya (Fig. 3.1a). In the mid-troposphere an Arabian anticyclone extends eastward to the western coast of India near the Indo-

Pakistan border, allowing mid-latitude air to flow towards the Himalaya and South Asia. Furthermore, the upper-tropospheric Tibetan high is elongated westward to North Africa (Fig. 3.1c). Vellore et al. (2016) studied the synoptic conditions during 34 extreme precipitation events over the western Himalaya and observed similar synoptic preconditions. Thus, the synoptic conditions during this event are a typical example of subtropical monsoon flow interacting with extratropical circulations.

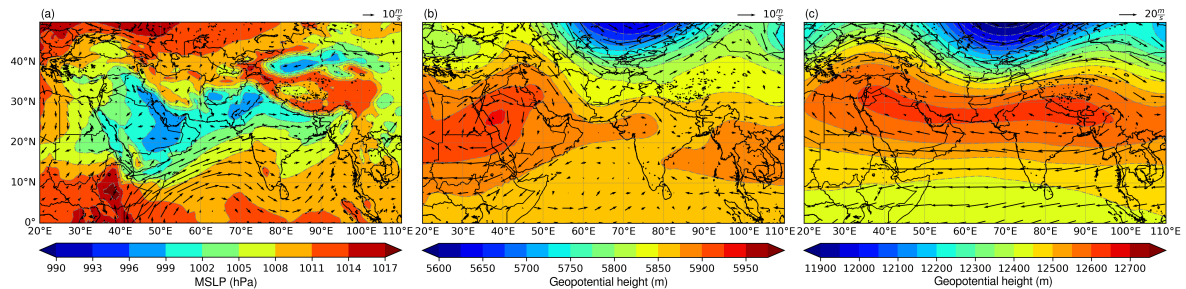


Figure 3.1. Synoptic atmospheric conditions during the flooding event. (a) sea level pressure (hPa, shaded) and 850 hPa wind (m/s, vector), (b) 500 hPa geopotential height (m, shaded) and 500 hPa wind (m/s, vector), and (c) 200 hPa geopotential height (m, shaded) and 200 hPa wind (m/s, vector).

Figs. 3.2a and b display the total accumulated precipitation from 11-16 August based on ground observations and satellite observations, respectively. These observations are consistent with one another and exhibit an accumulation of > 500 mm precipitation around the southern part of central and western Nepal.

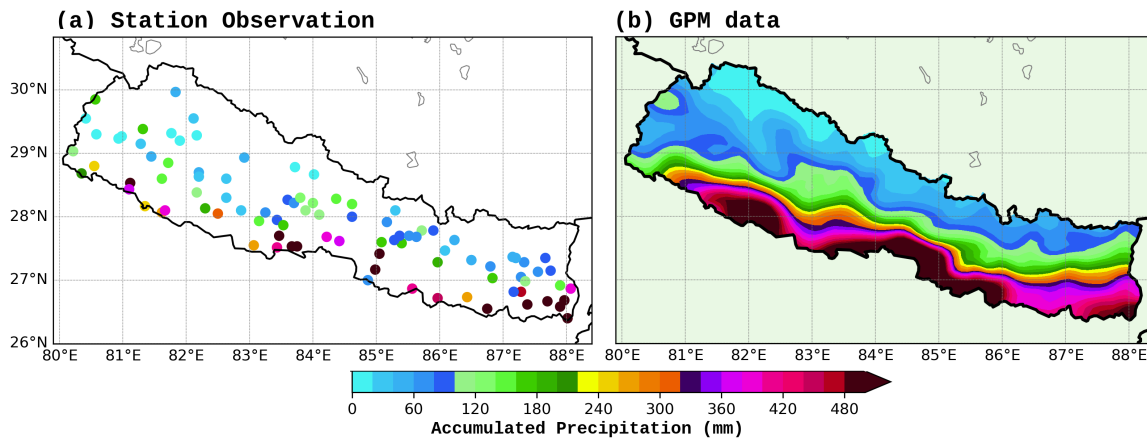


Figure 3.2. Total accumulated precipitation from 11-16 August 2017. (a) Station observations, and (b) Global Precipitation Measurement (GPM) precipitation data

3.3.2 Data

Both the ERA-Interim and National Centers for Environmental Prediction (NCEP) FiNaL (FNL) Operational Global Analysis data are used to force the WRF model at its lateral boundaries (in separate simulations). ERA-Interim is a product of the European Center for Medium-Range Weather Forecast (ECMWF), which

can be downloaded at its default $0.75^{\circ} \times 0.75^{\circ}$ horizontal resolution and 61 vertical model levels (Dee et al., 2011). Furthermore, the NCEP FNL data are available at $1^{\circ} \times 1^{\circ}$ horizontal resolution and 26 vertical pressure levels (<https://rda.ucar.edu/datasets/ds083.2/>, NCEP/NWS/NOAA/U.S. Department of Commerce (2000)). The temporal resolution for both ERA-Interim and NCEP data is 6 hours.

To provide a measure of ground-truthing for the sensitivity tests of the WRF simulations, daily accumulated precipitation recorded at 95 stations across Nepal are used. The station data is obtained from the Department of Hydrology and Meteorology (DHM), Nepal. The list of stations used in this study were given in Appendix A. Furthermore, the Global Precipitation Mission (GPM) satellite product (Huffman et al., 2014) is also used to compare with the gridded model simulations. Murali Krishna et al. (2017) analyzed the performance of GPM data over the Indian subcontinent and found that GPM data reproduced the spatial features of monsoon rainfall but underestimated precipitation values compared to station observations. Since GPM data have not been extensively tested over the Himalaya, we therefore use them for spatial comparisons only.

3.3.3 Model description

The Weather Research and Forecasting (WRF) model version 3.8.1 is used to simulate the atmospheric conditions from 8-20 August 2017 using different cloud microphysics schemes. WRF is a non-hydrostatic mesoscale atmospheric model which is designed for both atmospheric research and numerical weather prediction. In this study, WRF is configured with two nested domains of 15 and 3 km horizontal resolutions and 50 variably spaced vertical levels. The highest model level is at 50 hPa with the lowest 11 levels lying below 1 Km. The model parameters used in this study are based on previous studies (Collier and Immerzeel, 2015; Karki et al., 2017, 2018) over the central Himalaya (Table 3.1).

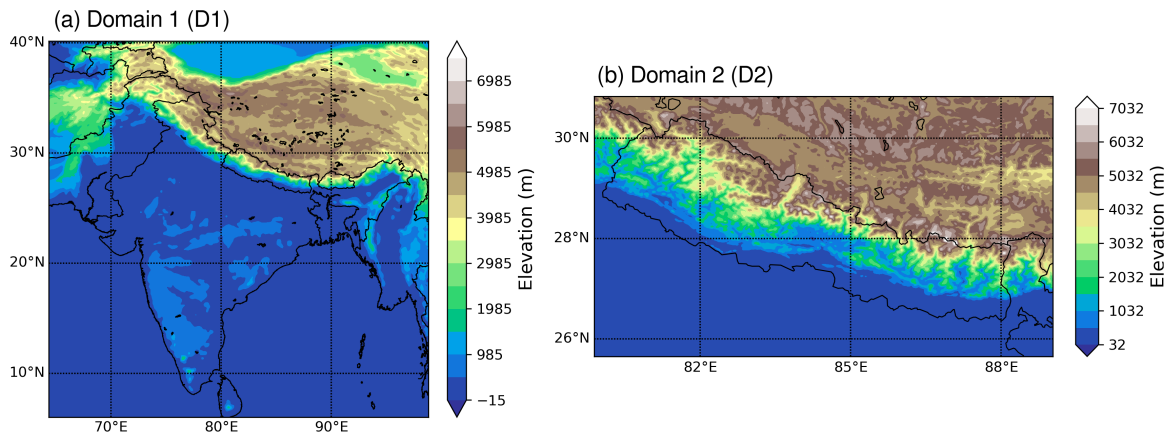
The geographical locations of the model domains are shown in Fig. 3.3. The outer domain (D1) covers South Asia, the Himalaya and the Tibetan Plateau, while the inner domain (D2) covers Nepal. A one-way nesting approach is applied to simulate the atmospheric fields from 8-20 August 2017 in all domains. Furthermore, the cumulus parameterization is turned on for D1 only, as previous studies found that D2 with a grid size of < 5 km, can explicitly resolve convection at the grid scale (Molinari and Dudek, 1992; Weisman et al., 1997).

3.3.4 Description of WRF microphysics schemes

Cloud microphysics is important for the development and distribution of various cloud particles and subsequent formation of different precipitating entities. WRF contains a number of different cloud microphysics schemes, each of which is capable of explicitly resolving cloud growth processes and the formation of hydrometeor particles. In this study, we analyzed the sensitivity of seven different microphysics schemes to simulate the

Table 3.1. WRF model configuration

Domain Configuration	
Horizontal grid Spacing	15 and 3 Km
Vertical levels	50
Model top pressure	50-hPa
Model Physics	
Radiation	Community Atmospheric Model
Cumulus	Kain-Fritsch (Kain, 2004)
Planetary boundary layer	MYNN level 2.5 (Nakanishi and Niino, 2006, 2009)
Atmospheric surface layer	Revised MM5 (Jiménez et al., 2012)
Land surface model	NOAH-MP (Niu et al., 2011; Yang et al., 2011)
Dynamics	
Top boundary condition	Rayleigh damping
Diffusion	Calculated in physical space
Lateral Boundaries	
Forcing	ERA–Interim 0.75 ⁰ X 0.75 ⁰

**Figure 3.3.** WRF domains (a) Outer domain (D1, 15km) and (b) Inner domain(D2, 3km). Topography is shaded in both domains.

flood-producing precipitation over Nepal, during August 2017. The microphysics schemes used in this study are: (a) Thompson (Thompson et al., 2008), (b) Morrison (Morrison and Gettelman, 2008); (c) Lin (Chen and Sun, 2002; Lin et al., 1983; Rutledge and Hobbs, 1984); (d) Milbrandt (Milbrandt and Yau, 2005); (e) Goddard (Lang et al., 2014; Tao et al., 2016); (f) WRF Single-moment 6-class (WSM6) (Hong et al., 2004; S.-Y. and J.-O., 2006); and (g) WRF Double-moment 6-class (WDM6) (Dudhia et al., 2008; Lim and Hong, 2010) schemes. These microphysics schemes consist of both single-moment and double-moment representations of hydrometeor particles. The single-moment microphysics schemes predict the total mass concentration, while the double-moment schemes predict both the mass and number concentration of a population of hydrometeors.

The WSM6 scheme is a single-moment 6-class microphysics scheme which includes water vapor, rain,

snow, cloud ice, cloud water, and graupel. This scheme works best for cloud-resolving grids. The WDM6 scheme is an update of WSM6 and calculates double-moment warm rain processes considering cloud and rain as prognostic variables. In both the WSM6 and WDM6, sedimentation of precipitating particles is handled with the Lagrangian scheme.

The Lin scheme also includes 6-classes of moisture variables (water vapor, cloud water, rain, cloud ice, snow and graupel). This scheme is a single-moment scheme and is suitable for high-resolution real-data simulations. The DHM uses the Lin scheme in their WRF model to forecast weather. The Goddard scheme is another single-moment 6-class microphysics scheme with an option to choose between graupel and hail.

The Thompson scheme is a bulk microphysics scheme with double-moment treatment of ice and rain. This scheme works best at a convection-permitting grid scale to represent mid-latitude convective and orographic precipitation. The Milbrandt scheme is a double-moment scheme with 12 prognostic variables (besides water vapor) and computes graupel and hail separately. The Morrison scheme is a double-moment bulk microphysics scheme with six species of hydrometeor (water vapor, cloud droplets, cloud ice, rain, snow, and graupel/hail). This scheme has been widely used and extensively tested for both real and idealized simulations of a variety of atmospheric conditions.

3.3.5 Evaluation of model output

The model output are first compared with the station observations. For this purpose, the simulations within the political boundaries of Nepal are divided into three different altitude levels based on the physiographic division of the Nepal Himalaya. The first level, consisting of the Terai and the Siwalik Regions (60 - 1,300 m asl), is defined as Region 1 (R1); a second level, consisting of the Middle Mountains (1,300 - 3,000 m asl), is defined as Region 2 (R2); and a third level, consisting of the High Mountains (>3,000 m asl), is defined as Region 3 (R3). R1 is the first step topography, and R2 and R3 combined form the second step of topography as explained by Shrestha et al. (2012). Thus, the first rainfall peak is observed over R1 and the second peak is observed over R2.

Simulated rainfall values are extracted from the closest-to-station grid-point based on the coordinates of the weather stations. Averages of individual points over the regions defined above are taken to make the statistical comparisons with the observations.

Bias

In this study we calculated the mean rainfall bias as the difference between the average simulated precipitation and the average observed precipitation over the three regions R1, R2, and R3. The unit of mean rainfall bias is

mmd⁻¹.

We also use relative bias (RB) to evaluate the performance of the WRF simulations. The relative bias is defined as:

$$RB = \frac{\sum M_i - O_i}{\sum O_i} \times 100 \quad (3.1)$$

where, M_i is the simulated precipitation and O_i is the observed precipitation. The value of RB is expressed in percentage (%). The values of RB are further categorized into three different classes as underestimation ($RB < -10\%$), overestimation ($RB > 10\%$), and nearly equal ($-10\% \leq RB \leq 10\%$).

Error calculation

The mean error (ME), mean absolute error (MAE), root mean square error (RMSE) and centered root mean square error (CRMSE) are the statistical tools used to evaluate the deviation of simulated parameters with respect to the observations. The MAE provides the linear measure of error, while the RMSE provides the quadratic mean of the difference between observed and simulated variables. Furthermore, the CRMSE is the quadratic mean of the difference between deviation of observed and simulated variables from their respective means. CRMSE is used to plot Taylor diagram. These statistics are calculated as follows:

$$ME = \frac{1}{n} \sum_{i=1}^n (M_i - O_i) \quad (3.2)$$

$$MAE = \frac{1}{n} \sum_{i=1}^n |M_i - O_i| \quad (3.3)$$

$$RMSE = \sqrt{\frac{1}{n} \sum_{i=1}^n (M_i - O_i)^2} \quad (3.4)$$

$$CRMSE = \sqrt{\frac{1}{n} \sum_{i=1}^n [(M_i - \bar{M}_i) - (O_i - \bar{O}_i)]^2} \quad (3.5)$$

Standard deviation, coefficient of variation and scale error

Standard deviation, coefficient of variation and scale error are calculated to estimate the deviation of daily precipitation from the mean precipitation over the study period. Standard deviation gives the difference of the daily precipitation (either simulated or observed) from the mean value. The coefficient of variation is calculated as the ratio of standard deviation to the mean. Likewise, scale error is the ratio of the standard deviation of simulated precipitation to the observed precipitation. A value of scale error close to 1 implies similarity in the

degree of scatter present in the simulations and observations.

Vertically integrated moisture flux

Vertically integrated moisture flux (VIMF) is calculated to ascertain the route of moisture flux. Since monsoon flow over Nepal is characterized by low-level moist flow, the horizontal components of mean VIMF are defined as the horizontal moisture fluxes in the zonal (Q_u) and meridional (Q_v) directions integrated from the surface to 700 hPa pressure level, i.e.,

$$Q_u = \frac{1}{g} \int_{700hPa}^{P_s} qu \, dp \quad (3.6)$$

$$Q_v = \frac{1}{g} \int_{700hPa}^{P_s} qv \, dp \quad (3.7)$$

Where, g is gravitational acceleration, q is specific humidity, and u and v are the zonal and meridional components of horizontal wind. The magnitude of VIMF is computed as the vector magnitude of Q_u and Q_v .

3.4 Results

3.4.1 Sensitivity analysis

The total accumulated precipitation over Nepal from 11 -16 August 2017 extracted from the D1 simulations using different cloud microphysics schemes and forcing data are presented in Fig. 3.4. Amongst the different simulations, both the Goddard-NCEP and Goddard-ERA simulations fail to capture the precipitation event presented in this study (Figs. 3.4a and h). All other simulations display precipitation accumulations over Nepal with varying intensities and spatial distributions. The WDM6-ERA and WSM6-ERA simulations produce > 480 mm of accumulated precipitation over the south-central and the south-eastern parts of Nepal (Figs. 3.4m and n). These regions of strong precipitation accumulations are consistent with the observations (Figs. 3.4o and p). Furthermore, amongst different simulations, WDM6-NCEP simulates the highest accumulated precipitation over the south-western part of Nepal (Fig. 3.4f).

The D2 simulation with the WDM6-ERA configuration produces large accumulated precipitation along the southern belt (the Terai) of Nepal. While the other configurations produce precipitation over the region, the magnitudes of the accumulation are relatively small. Although the D1 simulation with WSM6-ERA configuration performs well over south-central and south-eastern parts of Nepal, the D2 simulation with the same configuration fails to capture the intensity and spatial distribution of accumulated precipitation over Nepal. Comparison of the accumulated precipitation simulated in the D1 and D2 runs indicates that the grid scale "convection resolving" simulation (D2 with cumulus parameterization turned off) performs poorly compared with the coarser

simulation (D1).

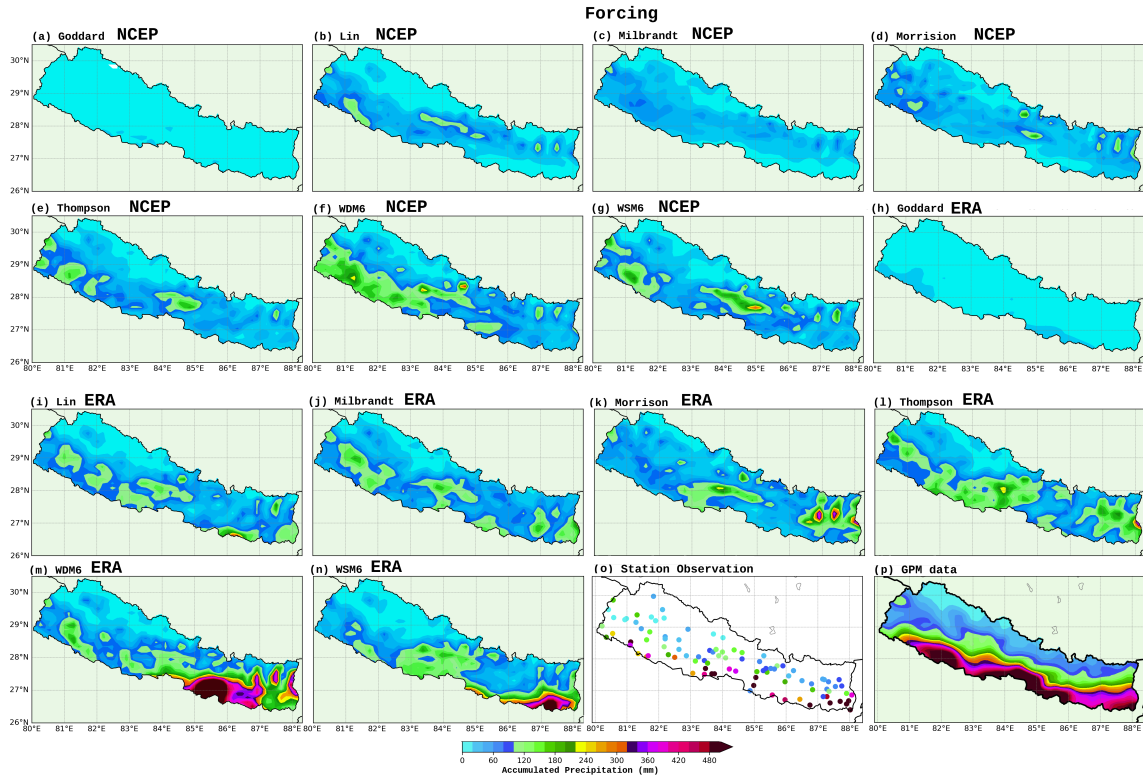


Figure 3.4. WRF simulated precipitation over D1 using (a) Goddard, (b) Lin, (c) Milbrandt, (d) Morrison, (e) Thompson, (f) WDM6 and (g) WSM6 schemes forced with NCEP data; (h) Goddard, (i) Lin, (j) Milbrandt, (k) Morrison, (l) Thompson, (m) WDM6, and (n) WSM6 schemes forced with ERA-Interim data; (o) station observation and (p) GPM data. All plots are accumulated precipitation over 11-16 August, 2017.

Comparison of daily accumulated precipitation over the simulation period over the three altitude regions (R1, R2 and R3) shows that the D1 simulations with ERA-Interim forcing perform better than the small grid scale, convection permitting D2 simulations. In particular, the D1 simulations with the WDM6-ERA and WSM6-ERA configurations perform better over R1, and almost every configuration (except Goddard) is consistent with the observations over R2. The D1 simulation with the WDM6-ERA configuration displays the precipitation peak on 12 August over R1, while the simulation with the WSM6-ERA configuration displays the peak on 13 August (Fig. 3.6a). Furthermore, over R2 every ERA-Interim forced simulation underestimates the precipitation peak on 11 August, while more than half of the simulations overestimate the peak on 13 August (Fig. 3.6b). Over R3, none of the simulations show any consistency with the observations.

For all configurations, the D2 simulations with the cumulus parameterization turned off fail to capture the magnitude of accumulated precipitation over R1 (Fig.3.6d), suggesting that WRF model is not explicitly simulating convection at this grid scale. Furthermore, over R2, the D2 simulations with the Goddard-ERA and Goddard-NCEP configurations capture the precipitation peak on 11 August, while the D2 simulation with the

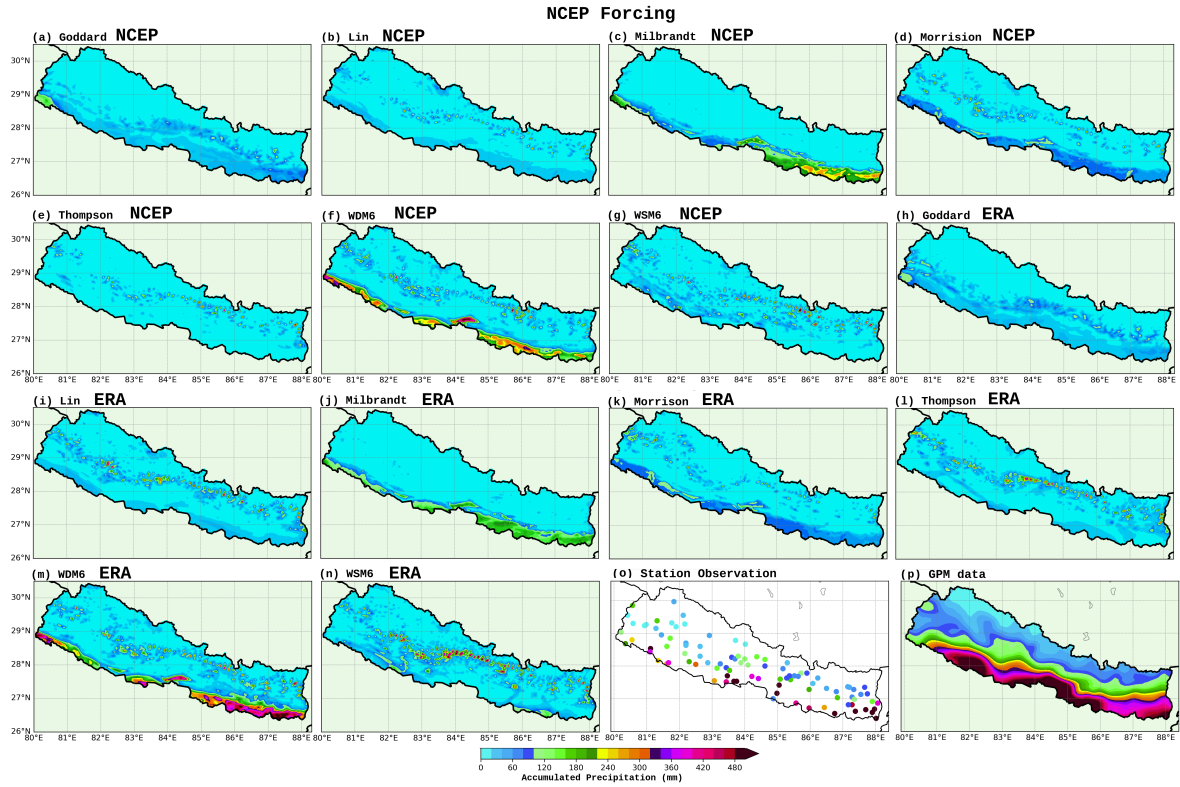


Figure 3.5. Same as Fig. 3.4, but for D2

WSM6-ERA configuration also captures the peak on 13 August (Fig. 3.6e). As with the D1 simulations, the D2 simulations are not consistent with the observation over R3 (Fig. 3.6f).

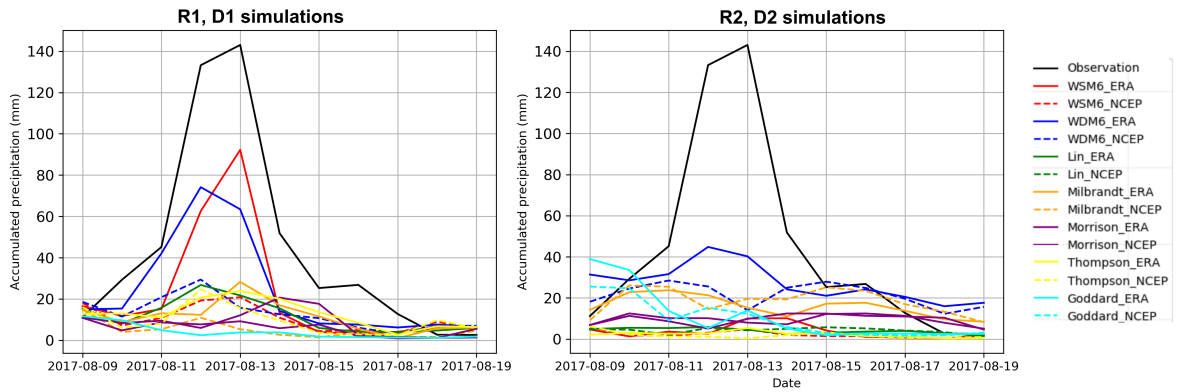


Figure 3.6. Comparison of the intensities of simulated precipitation with the observations.

A statistical comparison of precipitation results using different microphysics-forcing combinations is presented in Appendix B and Figs. 3.7 and 3.8. The RMSE and relative bias for the simulations using ERA-Interim initial conditions is lower than that for NCEP initial conditions, suggesting better performance with ERA-Interim forcing.

Table 3.2. Best performing simulations over different regions (R1, R2, R3) and domains (D1, D2)

Simulations	R1	R2	R3
D1	WSM6-ERA	WSM6-ERA	WDM6-NCEP
D2	WDM6-ERA	Goddard-ERA	WSM6-ERA

Among the different simulations over R1, the D1 simulation with the WSM6-ERA configuration exhibits the smallest RMSE followed by the WDM6-ERA configuration (Appendix B). The correlation coefficients (r) computed between the simulations and observations reveal that the value of r is between 0.9 and 0.95 for the WSM6-ERA (D1 simulation) and WDM6-ERA (D1 simulation) configurations. Furthermore, the standard deviation (σ) of the D1 simulation with the WSM6-ERA configuration is closer to the σ of the observations.

All D1 simulations (except those using Goddard) display improved performance over R2 than over R1. The WSM6-ERA configuration produces $< 1\%$ relative bias (positive) implying a higher accuracy of its precipitation simulation. Likewise, WSM6-NCEP also performs well with $< 5\%$ relative bias (positive). Out of 14 D1 simulations, 8 of them overestimate the magnitude of accumulated precipitation over R2, while all others underestimate it. The comparison of error statistics over R2 indicates that the D1 simulation with the WSM6-ERA configuration performs better and has the smallest RSME value. In addition, the RMSE values over R2 for all other D1 simulations are significantly lower than the RMSE values for R1, meaning there is better performance of all the simulations over R2. Furthermore, the D1 simulation over R2 with the WSM6-ERA configuration is more highly correlated with the observations than are the other simulations.

Over R3, the magnitude of the observed accumulated precipitation is very small, but even so the D1 simulations underestimate the quantity of accumulated precipitation. The D1 simulation with WDM6-NCEP produces the smallest RMSE over this region, followed by Thompson-ERA.

A statistical comparison of the D2 simulations shows that the WDM6-ERA configuration performs better than the other schemes over R1 with a low RMSE and strong positive correlations with the observations (Fig. 3.8). Conversely, over R2 and R3 the WDM6-ERA configuration is negatively correlated with the observations and hence exhibits poor performance. The D2 simulation with Goddard-ERA configuration is observed to perform best in R2 and WSM6-ERA performs best in R3. The best performing simulations over the three different regions are presented in Table 2.

3.4.2 Influence of cumulus parameterization on high-resolution simulation

High-resolution simulations (D2) with cumulus off fail to capture the magnitude and spatial distribution of precipitation over Nepal during the simulation period. So, we perform two experiments with cumulus turned on WSM6-ERA and WDM6-ERA configurations. We choose WSM6-ERA and WDM6-ERA configuration

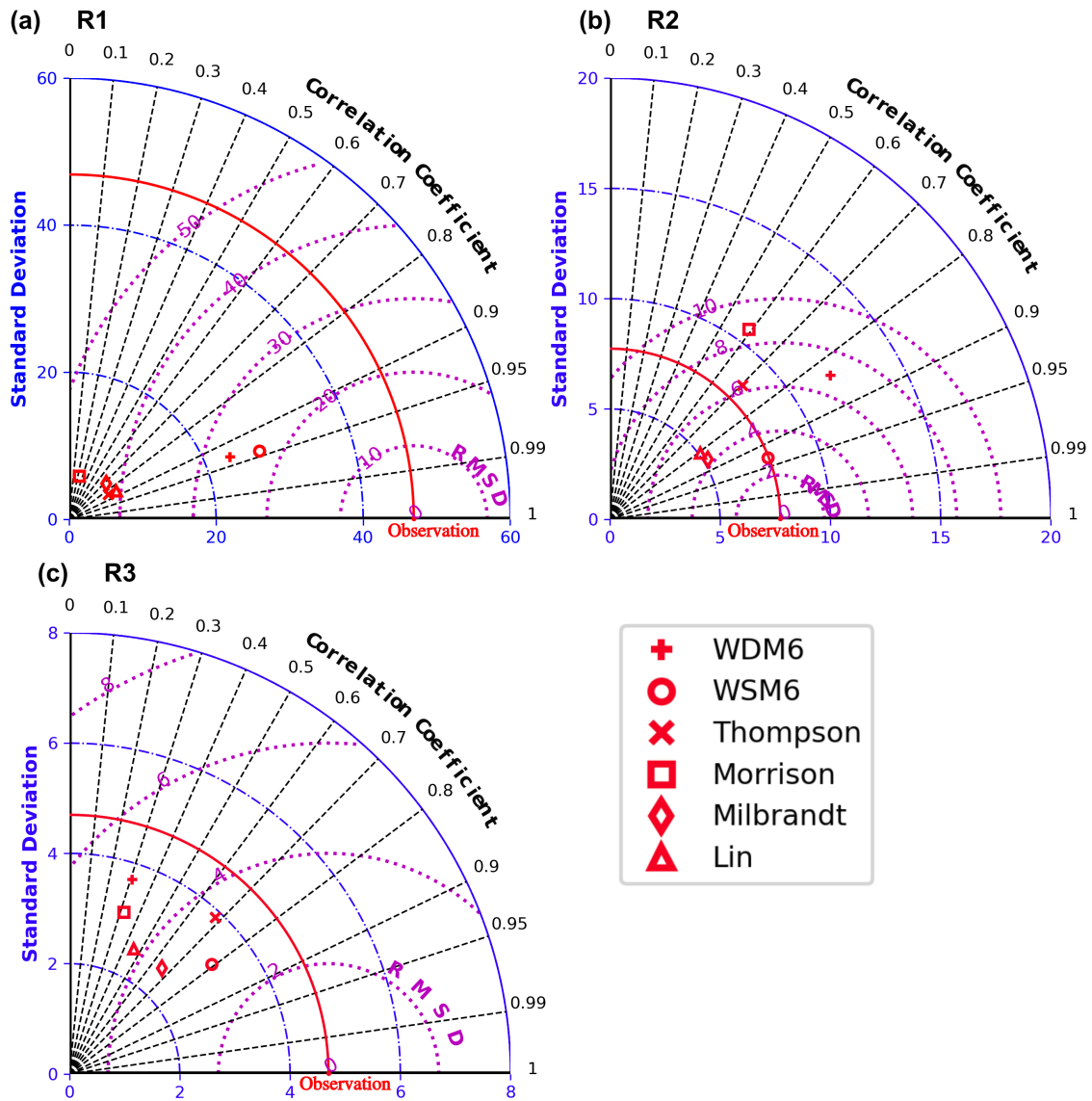


Figure 3.7. Comparison of the intensities of D1 simulations with the observations. (a) Over R1, (b) over R2, and (c) over R3. X and y axes represent standard deviation, blue arc represents correlation coefficient and purple arcs within plots represent centered root mean square deviation/error.

because they perform better than the other simulations in simulating precipitation over Nepal.

Turning on the cumulus schemes in the high resolution simulations with the WSM6-ERA and WDM6-ERA configurations shows no improvement in the WSM6-ERA configuration (Appendix B), but overall improvement in the WDM6-ERA configuration over R1 and slight improvement over R2 (Fig. 3.9). There is not much change in the performance over R3 in either configuration (figure not shown).

As explained by Shrestha et al. (2012), the precipitation over the Sub-Himalaya is of convective type, while the precipitation over the Lesser-Himalaya is stratiform type. Thus, over the highly convective region of the Sub-Himalaya, it is likely that WRF is not fully able to resolve convection at the 3 km grid scale. In the

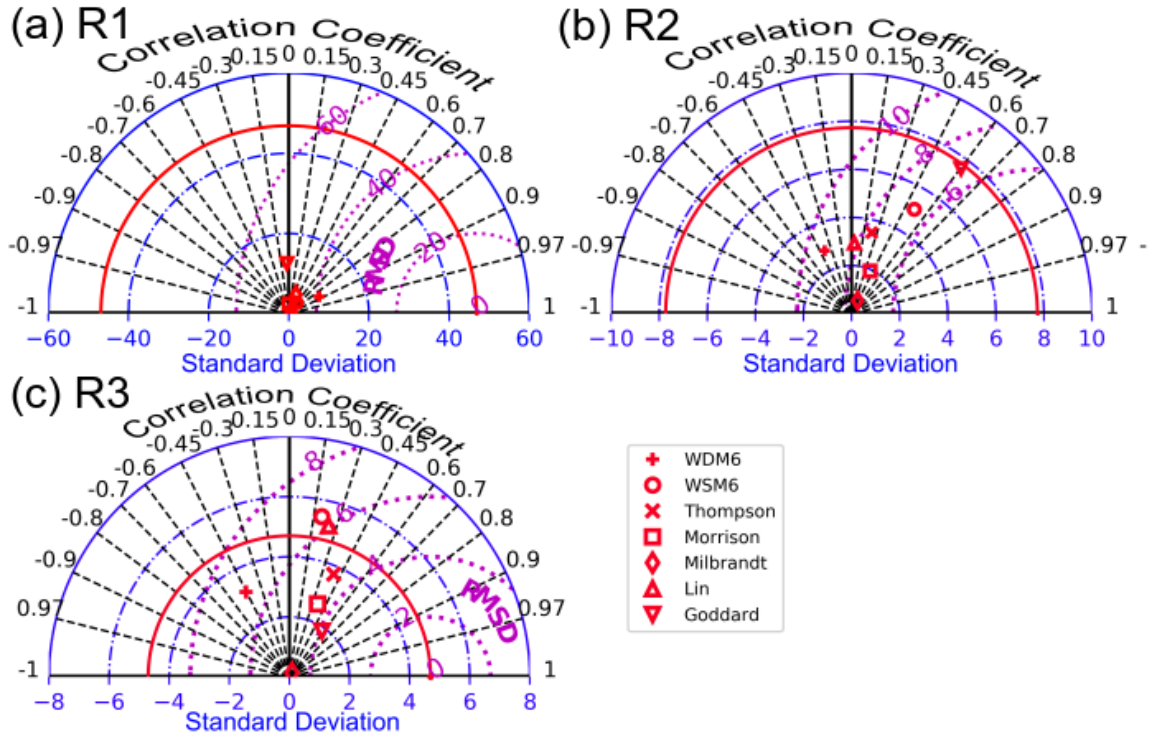


Figure 3.8. Same as Fig.3.7 but for D2 simulations

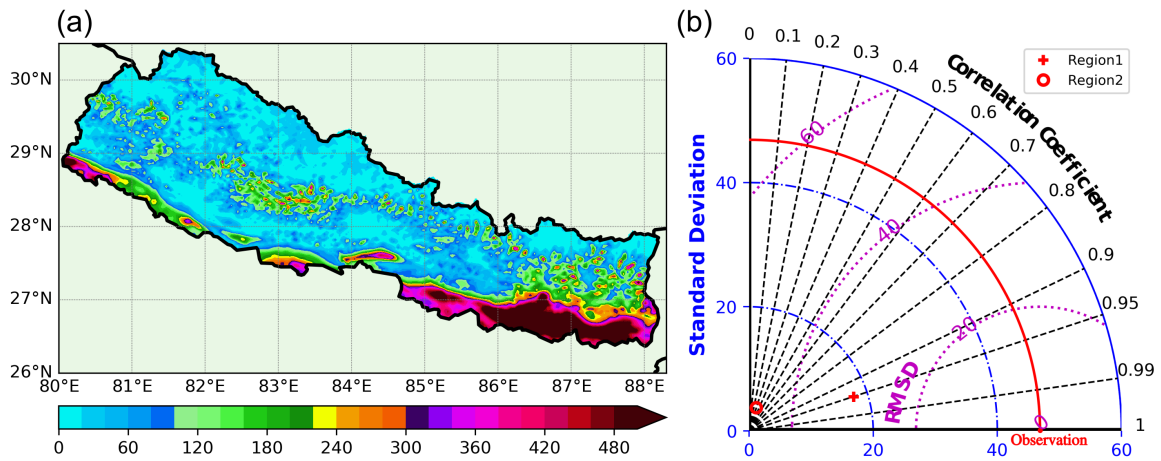


Figure 3.9. Comparison of precipitation intensities between the WDM6-ERA D2 simulation with cumulus scheme on and the observations over R1 and R2.

following sub-section we evaluate the extent of convection simulated by WRF by comparison with observed soundings obtained from the University of Wyoming.

3.4.3 Convection during the event

Analysis of vertical atmospheric soundings indicates that this flood-producing intense precipitation event is the result of strong convection. The radiosonde profile at the Patna station recorded at 00Z, 11 August 2017 (05:30 am local time) displays the presence of Convective Available Potential Energy (CAPE) > 1800 J/Kg without any Convective Inhibition (CIN) (Fig. 3.10a) and a thick moist layer extending from the surface to 400 hPa. The skew-T log-P diagrams in Fig. 3.10b and c are plotted from two WRF simulations (a D2 simulation with WDM6 microphysics with the cumulus scheme turned on and a D1 simulation with WSM6 microphysics, also with the cumulus scheme on). Both simulations show CAPE > 1500 J/Kg, although the depth of the moist layer is relatively shallow (from surface to 700 hPa) compared with the observations.

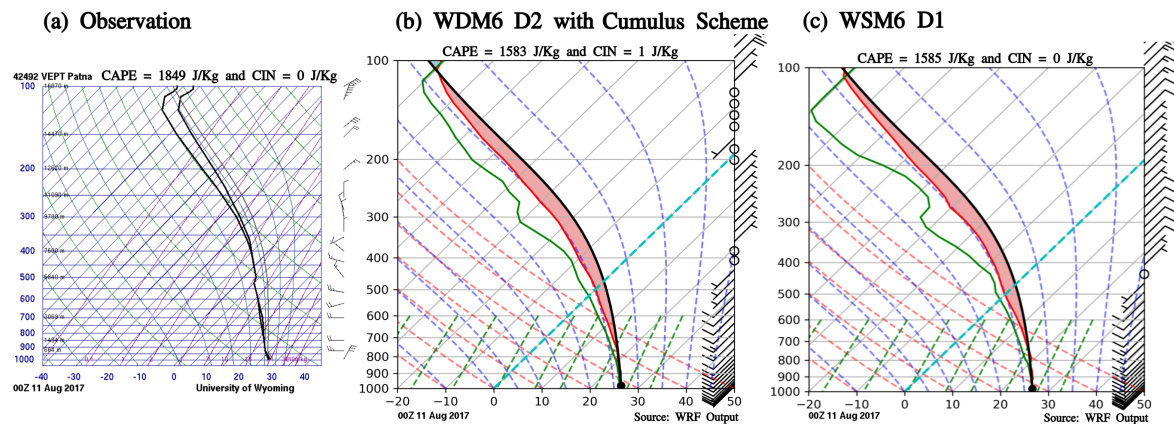


Figure 3.10. Skew-T diagram at 00Z, 11 August 2017, (a) Observation taken from Patna station, (b) WDM6 D2 with cumulus parameterization, and (c) WSM6 D1.

The soundings from the Patna station are not available for later hours (they are only available daily at 00Z), so only the skew-T diagrams from the two simulations are plotted at later hours. The skew-T diagrams at 06Z, 11 August 2017 (11:30 am local time) indicate a large increase in CAPE associated with diurnal solar heating (Fig. 3.11). Note that the wind barbs in Figs. 3.10 and 3.11 are consistent with the synoptic plots presented in Fig. 3.1.

3.4.4 Moisture flux

The VIMF is only computed for D1 with ERA-Interim forcing due to the superior performance of ERA-Interim data over NCEP data for simulated precipitation. Fig. 3.12 displays the VIMF and the total average precipitable water from 11-16 August. All the simulations, except those using Goddard, produce similar features of VIMF and total precipitable water, with > 70 mm precipitable water over the region extending from the Indo-Gangetic plain (along the Himalayan foothills) to the Bay of Bengal. The region of highest precipitable water is consistent

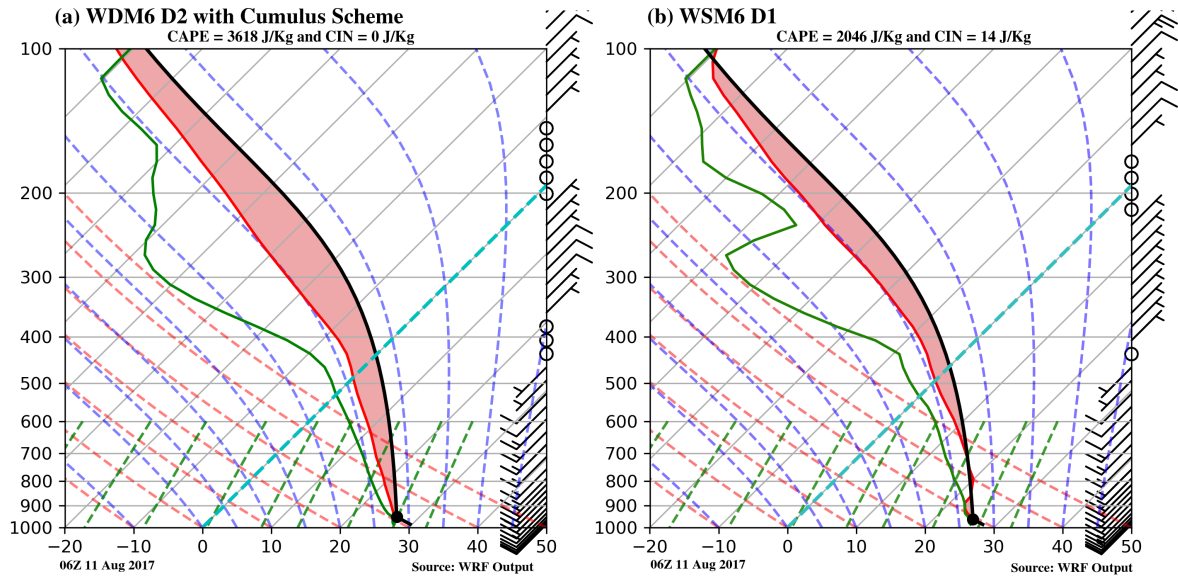


Figure 3.11. Skew-T diagram at 06Z, 11 August 2017, (a) WDM6 D2 with cumulus parameterization, and (b) WSM6 D1.

with the region of most intense precipitation over Nepal. Although all the simulations exhibit their highest precipitable water along the southern part of Nepal over the sub-Himalaya, only WDM6 and WSM6 show strong precipitation over the sub-Himalaya, suggesting the importance of cloud microphysics schemes in WRF as a function of orographic relief.

Further analysis of the VIMF reveals strong moisture flux from the Arabian Sea and the Bay of Bengal. Most of the simulations display the moisture flux between $150 - 250 \text{ Kg m}^{-1} \text{ s}^{-1}$ along the Indo-Nepal border. Furthermore, the Q_u and Q_v vectors show the cyclonic moisture convergence near $25 - 27^\circ \text{N}$ and $82-88^\circ \text{E}$. This cyclonic flow brings moisture towards the Gangetic plain producing precipitation along the Gangetic plain and sub-Himalaya.

3.5 Discussion

This study highlights the importance of cloud microphysics, convection and initial conditions to simulate the flood-producing precipitation event over the southern belt of Nepal during the monsoon 2017. Almost all the simulations performed display precipitation accumulations over Nepal over the simulation period. However, there are large variations in the intensity of precipitation simulated by the different microphysics-forcing combinations. Region-wise evaluation of the simulations reveals that over R1, the D1 simulation with WSM6-ERA performed the best, followed by WDM6-ERA. However, all the simulations underestimate the intensity of precipitation. Over R2 more than half of the D1 simulations display improved performance, with WSM6-ERA

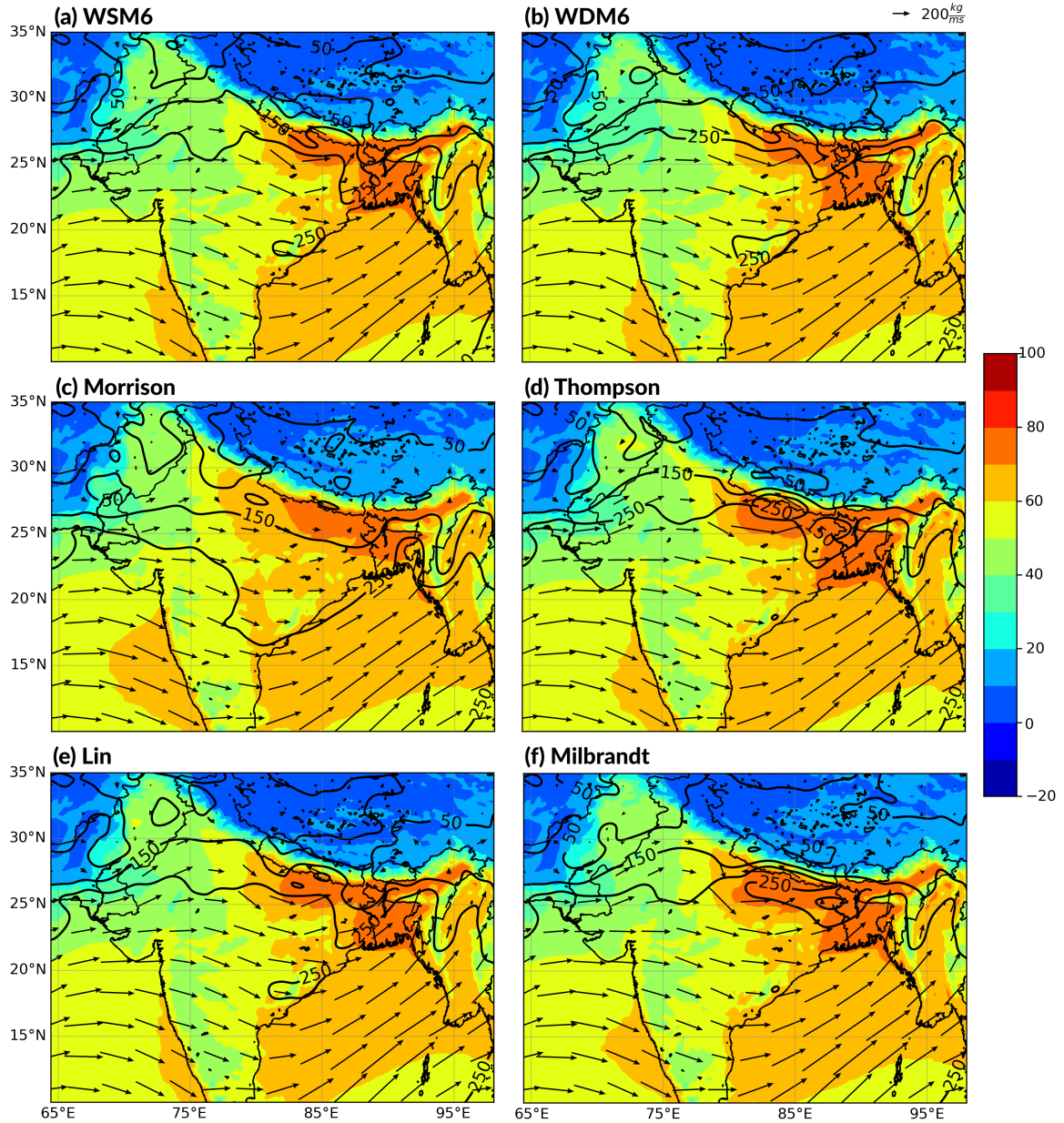


Figure 3.12. Average simulated VIMF from the surface to 700 hPa (vector and contour, $\text{kgm}^{-1}\text{s}^{-1}$) and precipitable water (shaded, mm) over 11-16 August using various microphysics options and ERA-Interim forcing.

displaying minimum RMSE and a small positive bias. None of the WRF simulations are consistent with observations over R3, where the daily accumulated precipitation is very low.

The overall comparison of precipitation simulations from different WRF runs show that ERA-Interim initial conditions and forcing provide better results compared with the NCEP data. There has been a similar study over the Tibetan plateau, where the initial condition obtained from the ERA-Interim data resulted in better simulations than the NCEP data (Liu et al., 2019).

Furthermore, the high resolution (D2) simulations with cumulus parameterization turned off display poor performance compared to the D1 simulations. Numerical weather prediction models are believed to explicitly resolve convection at grid size below 10 km, though some studies have identified that grid resolutions between 5 - 10 km are a gray zone where the cumulus scheme may or may not be important. However, Kotroni and Lagouvardos (2004) and Deng and Stauffer (2006) found the improvement in the performance of mesoscale numerical models over Athens, Greece and eastern United States, respectively when the cumulus scheme is turned on for horizontal resolutions below 5 km. Chawla et al. (2018) performed sensitivity experiments involving different cloud microphysics, cumulus and planetary boundary layer schemes and found unrealistic results in their 3 km run with cumulus parameterization turned off over the upper Ganga Basin in the western Himalaya.

The sensitivity experiments with the cumulus scheme turned on using WDM6-ERA at the horizontal resolution of 3 Km (D2) displayed an overall improvement in the performance of the model to simulate the precipitation over R1. The RMSE and relative bias computed with this simulation is even better than the D1 simulation with the WSM6-ERA combination. Furthermore, the skew-T diagram plotted from different WRF runs (at 00Z) show the D1 run with the WSM6-ERA combination and the D2 run with the WDM6-ERA and cumulus parameterization on show CAPE close to the observations. Moreover, the skew-Ts plotted six hours later (06Z) show that the D2 run (with WDM6-ERA and cumulus) simulates more than 3500 J/Kg CAPE, which is more than 1500 J/Kg higher than the D1 run with the WSM6-ERA combination. Thus, our study suggests that over steeper topography mesoscale atmospheric models are not capable of resolving convection at grid scale even if the horizontal resolution is < 5 km, and underestimate the quantity of accumulated precipitation. So, it is important leave the cumulus scheme on for highly convective events over steeper topography.

The analysis of VIMF and precipitable water from the different WRF simulations display a general consistency amongst the simulations. The WRF simulations using WSM6, WDM6, Thompson, Lin and Milbrandt microphysics schemes forced with ERA-Interim data show a moisture flux between 150 - 250 $\text{Kg m}^{-1}\text{s}^{-1}$ along the Indo - Gangetic plain. Similarly, the amount of precipitable water is also consistent between the different simulations. This highlights the fact that despite all the simulations showing consistency in moisture flux, the cloud microphysics controls the development and distribution of various hydrometeors and hence the quantity of precipitation.

3.6 Conclusions

In this study we performed sensitivity tests of seven different cloud microphysics schemes available within the WRF model and two different forcing data to simulate a severe flood-producing precipitation event over Nepal. The D1 simulations with WSM6 and WDM6 microphysics schemes forced with the ERA-Interim data produced

the minimum RMSE and are highly correlated with the observations. It is of note that the D2 simulations with convection permitting horizontal resolution (i.e., with the cumulus scheme turned off) fail to capture both the intensity and spatial distribution of precipitation.

The use of the cumulus scheme for the high resolution (D2) WDM6-ERA simulation produces an overall improvement in the precipitation simulation. In particular, there is a more than 50 % reduction in the RMSE value when the cumulus scheme is turned on. Furthermore, comparison of the simulated vertical atmospheric profile with observations at the Patna station indicate similar profiles with $CAPE > 500 \text{ J/Kg}$.

Most of the microphysics schemes used in this study display a similar pattern of moisture flux and precipitable water, while the microphysics scheme determines the type of hydrometeor and hence the spatial and temporal precipitation patterns. For this particular event, and presumably for other events similar to it in a synoptic sense, the current microphysics scheme used by the DHM's weather forecasting system fails to capture the intensity and distribution of flood-producing precipitation. We would therefore recommend an examination of our statistical results in order to choose the best scheme for the physical configuration of their forecasting system.

References

- Barros, A. P., Joshi, M., Putkonen, J., and Burbank, D. W. (2000). A study of 1999 monsoon rainfall in a mountainous region in Central Nepal using TRMM products and rain gauge observations. *Geophysical Research Letters*, 27(22):3683–3686.
- Bhandari, D., Uprety, M., Ghimire, G., Kumal, B., Pokharel, L., and Khadka, P. (2018). Nepal flood 2017: Wake up call for effective preparedness and response. *Rugby, UK: Practical Action*.
- Bhomia, S., Kumar, P., and Kishtawal, C. M. (2019). Evaluation of the weather research and forecasting model forecasts for Indian summer monsoon rainfall of 2014 using ground based observations. *Asia-Pacific Journal of Atmospheric Sciences*.
- Chawla, I., Osuri, K. K., Mujumdar, P. P., and Niyogi, D. (2018). Assessment of the Weather Research and Forecasting (WRF) model for simulation of extreme rainfall events in the upper Ganga Basin. *Hydrology and Earth System Sciences*, 22(2):1095–1117.
- Chen, S.-H. and Sun, W.-Y. (2002). A one-dimensional time dependent cloud model. *Journal of the Meteorological Society of Japan. Ser. II*, 80(1):99–118.
- Collier, E. and Immerzeel, W. W. (2015). High-resolution modeling of atmospheric dynamics in the Nepalese Himalaya. *Journal of Geophysical Research: Atmospheres*, 120(19):9882–9896.
- Collier, E., Nicholson, L. I., Brock, B. W., Maussion, F., Essery, R., and Bush, A. B. G. (2014). Representing moisture fluxes and phase changes in glacier debris cover using a reservoir approach. *The Cryosphere*, pages 1429–1444.
- Dee, D. P., Uppala, S. M., Simmons, A. J., Berrisford, P., Poli, P., Kobayashi, S., Andrae, U., Balmaseda, M. A., Balsamo, G., Bauer, P., Bechtold, P., Beljaars, A. C. M., van de Berg, L., Bidlot, J., Bormann, N., Delsol, C., Dragani, R., Fuentes, M., Geer, A. J., Haimberger, L., Healy, S. B., Hersbach, H., Hlm, E. V., Isaksen, L., Killberg, P., Khlér, M., Matricardi, M., McNally, A. P., Monge-Sanz, B. M., Morcrette, J.-J., Park, B.-K., Peubey, C., de Rosnay, P., Tavolato, C., Thpaut, J.-N., and Vitart, F. (2011). The era-interim reanalysis: configuration and performance of the data assimilation system. *Quarterly Journal of the Royal Meteorological Society*, 137(656):553–597.
- Deng, A. and Stauffer, D. R. (2006). On improving 4-km mesoscale model simulations. *Journal of Applied Meteorology and Climatology*, 45(3):361–381.

- Dimri, A. P. and Chevuturi, A. (2014). Model sensitivity analysis study for western disturbances over the Himalayas. *Meteorology and Atmospheric Physics*, 123(3-4):155–180.
- Dudhia, J., HONG, S.-Y., and Lim, K.-S. (2008). A new method for representing mixed-phase particle fall speeds in bulk microphysics parameterizations. *Journal of the Meteorological Society of Japan. Ser. II*, 86A:33–44.
- Hong, S.-Y., Dudhia, J., and Chen, S.-H. (2004). A revised approach to ice microphysical processes for the bulk parameterization of clouds and precipitation. *Monthly Weather Review*, 132(1):103–120.
- Huffman, G., Bolvin, D., Braithwaite, D., Hus, K., Joyce, R., and Xie, P. (2014). Integrated multi-satellite retrievals for GPM (IMERG), version 4.4. *NASA's Precipitation Processing Center*.
- Ichiyanagi, K., Yamanaka, M. D., Muraji, Y., and Vaidya, B. K. (2007). Precipitation in Nepal between 1987 and 1996. *International Journal of Climatology*, 27(13):1753–1762.
- Jiménez, P. A., Dudhia, J., González-Rouco, J. F., Navarro, J., Montvez, J. P., and García-Bustamante, E. (2012). A revised scheme for the WRF surface layer formulation. *Monthly Weather Review*, 140(3):898–918.
- Kain, J. S. (2004). The Kain-Fritsch convective parameterization: An update. *Journal of Applied Meteorology*, 43(1):170–181.
- Kansakar, S. R., Hannah, D. M., Gerrard, J., and Rees, G. (2004). Spatial pattern in the precipitation regime in Nepal. *International Journal of Climatology*, 24(13):1645–1659.
- Karki, R., Ul-Hasson, S., Gerlitz, L., Schickhoff, U., Scholten, T., and Böhner, J. (2017). Quantifying the added value of convection-permitting climate simulations in complex terrain: A systematic evaluation of WRF over the Himalayas. *Earth System Dynamics*, 8(3):507–528.
- Karki, R., ul-Hasson, S., Gerlitz, L., Talchabhadel, R., Schenk, E., Schickhoff, U., Scholten, T., and Böhner, J. (2018). WRF-based simulation of an extreme precipitation event over the Central Himalayas: Atmospheric mechanisms and their representation by microphysics parameterization schemes. *Atmospheric Research*, 214(July):21–35.
- Kotroni, V. and Lagouvardos, K. (2004). Evaluation of MM5 high-resolution real-time forecasts over the urban area of Athens, Greece. *Journal of Applied Meteorology*, 43(11):1666–1678.
- Lang, S. E., Tao, W.-K., Chern, J.-D., Wu, D., and Li, X. (2014). Benefits of a fourth ice class in the simulated radar reflectivities of convective systems using a bulk microphysics scheme. *Journal of the Atmospheric Sciences*, 71(10):3583–3612.

- Lang, T. J. and Barros, A. P. (2002). An investigation of the onsets of the 1999 and 2000 monsoons in Central Nepal. *Monthly Weather Review*, 130(5):1299–1316.
- Lim, K.-S. S. and Hong, S.-Y. (2010). Development of an effective double-moment cloud microphysics scheme with prognostic cloud condensation nuclei (CCN) for weather and climate models. *Monthly Weather Review*, 138(5):1587–1612.
- Lin, Y.-L., Farley, R. D., and Orville, H. D. (1983). Bulk parameterization of the snow field in a cloud model. *Journal of Climate and Applied Meteorology*, 22(6):1065–1092.
- Liu, L., Ma, Y., Menenti, M., Zhang, X., and Ma, W. (2019). Evaluation of WRF modeling in relation to different land surface schemes and initial and boundary conditions: A snow event simulation over the Tibetan plateau. *Journal of Geophysical Research: Atmospheres*, 124(1):209–226.
- Maussion, F., Scherer, D., Finkelnburg, R., Richters, J., Yang, W., and Yao, T. (2011). WRF simulation of a precipitation event over the Tibetan Plateau, China - An assessment using remote sensing and ground observations. *Hydrology and Earth System Sciences*, 15(6):1795–1817.
- Medina, S., Houze, R. A., Kumar, A., and Niyogi, D. (2010). Summer monsoon convection in the Himalayan region: Terrain and land cover effects. *Quarterly Journal of the Royal Meteorological Society*, 136(648):593–616.
- Milbrandt, J. A. and Yau, M. K. (2005). A multimoment bulk microphysics parameterization. part I: Analysis of the role of the spectral shape parameter. *Journal of the Atmospheric Sciences*, 62(9):3051–3064.
- MoHA (2018). *Nepal Disaster Report, 2017: The Road to Sendai*. Kathmandu: Government of Nepal.
- Molinari, J. and Dudek, M. (1992). Parameterization of convective precipitation in mesoscale numerical models: A critical review. *Monthly Weather Review*, 120(2):326–344.
- Morrison, H. and Gettelman, A. (2008). A new two-moment bulk stratiform cloud microphysics scheme in the community atmosphere model, version 3 (cam3). part I: Description and numerical tests. *Journal of Climate*, 21(15):3642–3659.
- Murali Krishna, U. V., Das, S. K., Deshpande, S. M., Doiphode, S. L., and Pandithurai, G. (2017). The assessment of global precipitation measurement estimates over the Indian subcontinent. *Earth and Space Science*, 4(8):540–553.
- Nakanishi, M. and Niino, H. (2006). An improved Mellor-Yamada level-3 model: Its numerical stability and application to a regional prediction of advection fog. *Boundary-Layer Meteorology*, 119(2):397–407.

- Nakanishi, M. and Niino, H. (2009). Development of an improved turbulence closure model for the atmospheric boundary layer. *Journal of the Meteorological Society of Japan. Ser. II*, 87(5):895–912.
- National Centers for Environmental Prediction/National Weather Service/NOAA/U.S. Department of Commerce (2000). NCEP FNL operational model global tropospheric analyses, continuing from July 1999. Research Data Archive at the National Center for Atmospheric Research, Computational and Information System Laboratory, Boulder, Colorado (Updated Daily). Accessed 23/03/2019
- Niu, G.-Y., Yang, Z.-L., Mitchell, K. E., Chen, F., Ek, M. B., Barlage, M., Kumar, A., Manning, K., Niyogi, D., Rosero, E., Tewari, M., and Xia, Y. (2011). The community NOAA land surface model with multiparameterization options (NOAH-MP): 1. model description and evaluation with local-scale measurements. *Journal of Geophysical Research: Atmospheres*, 116(D12).
- Norris, J., Carvalho, L. M., Jones, C., and Cannon, F. (2015). WRF simulations of two extreme snowfall events associated with contrasting extratropical cyclones over the western and Central Himalaya. *Journal of Geophysical Research*, 120(8):3114–3138.
- NPC (2017c). *Nepal Flood 2017: Post flood recovery needs assessment*. Kathmandu: National Planning Commission (NPC), Government of Nepal.
- Orr, A., Listowski, C., Coustet, M., Collier, E., Immerzeel, W., Deb, P., and Bannister, D. (2017). Sensitivity of simulated summer monsoonal precipitation in Langtang Valley, Himalaya, to cloud microphysics schemes in WRF. *Journal of Geophysical Research: Atmospheres*, 122(12):6298–6318.
- Pokhrel, D., Bhandari, B., and Viraraghavan, T. (2009). Natural hazards and environmental implications in Nepal. *Disaster Prevention and Management: An International Journal*, 18(5):478–489.
- Regmi, R. P., Kitada, T., Dudhia, J., and Maharjan, S. (2017). Large-scale gravity current over the middle hills of the Nepal Himalaya: Implications for aircraft accidents. *Journal of Applied Meteorology and Climatology*, 56(2):371–390.
- Romatschke, U. and Houze, R. A. (2011). Characteristics of precipitating convective systems in the South Asian monsoon. *Journal of Hydrometeorology*, 12(1):3–26.
- Rutledge, S. A. and Hobbs, P. V. (1984). The mesoscale and microscale structure and organization of clouds and precipitation in midlatitude cyclones. XII: A diagnostic modeling study of precipitation development in narrow cold-frontal rainbands. *Journal of the Atmospheric Sciences*, 41(20):2949–2972.

- S.-Y., H. and J.-O., J. (2006). The WRF single-moment 6-class microphysics scheme (WSM6). *J. Korean Metero. Soc.*, 42:129–151.
- Shrestha, D., Singh, P., and Nakamura, K. (2012). Spatiotemporal variation of rainfall over the Central Himalayan region revealed by TRMM precipitation radar. *Journal of Geophysical Research: Atmospheres*, 117(D22).
- Shrestha, M. L. (2000). Interannual variation of summer monsoon rainfall over Nepal and its relation to Southern Oscillation Index. *Meteorology and Atmospheric Physics*, 75(1-2):21–28.
- Shrestha, R. K., Gallagher, M. W., and Connolly, P. J. (2016). Diurnal and seasonal variations of meteorology and aerosol concentrations in the foothills of the Nepal Himalayas (Nagarkot: 1,900 m asl). *Asia-Pacific Journal of Atmospheric Sciences*, 52(1):63–75.
- Stigter, E. E., Litt, M., Steiner, J. F., Bonekamp, P. N. J., Shea, J. M., Bierkens, M. F. P., and Immerzeel, W. W. (2018). The Importance of Snow Sublimation on a Himalayan Glacier. *Frontiers in Earth Science*, 6(August):1–16.
- Tao, W.-K., Wu, D., Lang, S., Chern, J.-D., Peters-Lidard, C., Fridlind, A., and Matsui, T. (2016). High-resolution nu-WRF simulations of a deep convective-precipitation system during MC3E: Further improvements and comparisons between Goddard microphysics schemes and observations. *Journal of Geophysical Research: Atmospheres*, 121(3):1278–1305.
- Thompson, G., Field, P. R., Rasmussen, R. M., and Hall, W. D. (2008). Explicit forecasts of winter precipitation using an improved bulk microphysics scheme. part II: Implementation of a new snow parameterization. *Monthly Weather Review*, 136(12):5095–5115.
- Tiwari, S., Kar, S. C., and Bhatla, R. (2018). Dynamic downscaling over Western Himalayas: Impact of cloud microphysics schemes. *Atmospheric Research*, 201(October 2017):1–16.
- Vellore, R. K., Kaplan, M. L., Krishnan, R., Lewis, J. M., Sabade, S., Deshpande, N., Singh, B. B., Madhura, R. K., and Rama Rao, M. V. (2016). Monsoon-extratropical circulation interactions in Himalayan extreme rainfall. *Climate Dynamics*, 46(11-12):3517–3546.
- Vellore, R. K., Krishnan, R., Pendharkar, J., Choudhury, A. D., and Sabin, T. P. (2014). On the anomalous precipitation enhancement over the Himalayan foothills during monsoon breaks. *Climate Dynamics*, 43(7-8):2009–2031.

Weisman, M. L., Skamarock, W. C., and Klemp, J. B. (1997). The resolution dependence of explicitly modeled convective systems. *Monthly Weather Review*, 125(4):527–548.

Yang, Z.-L., Niu, G.-Y., Mitchell, K. E., Chen, F., Ek, M. B., Barlage, M., Longuevergne, L., Manning, K., Niyogi, D., Tewari, M., and Xia, Y. (2011). The community NOAH land surface model with multiparameterization options (NOAH-MP): 2. evaluation over global river basins. *Journal of Geophysical Research: Atmospheres*, 116(D12).

Appendix A

Appendix A: List of Meteorological Stations used in the Study

ID	Station Name	Lat.	Lon.	ID	Station Name	Lat.	Lon.
102	Baitadi	29.55	80.42	805	Syangja	28.10	83.88
104	Dadeldhura	29.30	80.58	809	Gorkha	28.00	84.62
105	Mahendranagar	29.03	80.22	814	Kaski	28.30	83.80
106	Belauri Santipur	28.68	80.35	815	Khairini Tar	28.03	84.10
107	Darchula	29.85	80.57	820	Chame	28.67	84.02
203	Silgadhi Doti	29.27	80.98	823	Gharedhunga	28.20	84.62
204	Bajura	29.38	81.32	902	Rampur	27.62	84.42
206	Asra Ghat	28.95	81.45	905	Daman	27.60	85.08
207	Tikapur	28.53	81.12	906	Hetauda	27.42	85.05
209	Dhangadhi (Atariya)	28.80	80.55	909	Simara Airport	27.17	84.98
217	Mangalsen	29.15	81.28	918	Birganj	27.00	84.87
218	Dipayal (Doti)	29.23	80.93	1004	Nuwakot	27.92	85.17
302	Thirpu	29.32	81.77	1009	Chautara	27.78	85.72
303	Jumla	29.28	82.17	1022	Godavari	27.58	85.40
307	Mugu	29.55	82.12	1027	Barabise	27.78	85.90
308	Kalikot	29.20	81.90	1030	Kathmandu Airport	27.70	85.37
311	Humla	29.97	81.83	1036	Panchkhal	27.68	85.63
312	Dolpa	28.93	82.92	1043	Nagarkot	27.70	85.52
402	Dailkeh	28.85	81.72	1055	Dhunche	28.10	85.30
404	Jajarkot	28.70	82.20	1073	Kokhana	27.63	85.28
406	Surkhet (Birendranagar)	28.60	81.62	1103	Jiri	27.63	86.23
408	Gulariya	28.17	81.35	1107	Sindhuli Gadhi	27.28	85.97
411	Rajapur	28.43	81.10	1111	Janakpur Airport	26.72	85.97
416	Nepalgunj (Reg. Off)	28.07	81.62	1120	Malangwa	26.87	85.57
420	Nepalgunj Airport	28.10	81.67	1123	Manthali	27.47	86.08
501	Rukumkot	28.60	82.63	1206	Okhaldhunga	27.32	86.50
504	Liban Gaun	28.30	82.63	1211	Khotang Bazar	27.03	86.83
505	Bijuwar Tar	28.10	82.87	1215	Lahan	26.73	86.43
508	Tulsipur	28.13	82.30	1222	Diktel	27.22	86.80
511	Salyan Bazar	28.38	82.17	1223	Rajbiraj	26.55	86.75
513	Chaur Jhari Tar	28.63	82.20	1303	Chainpur (East)	27.28	87.33
515	Ghorai (Dang)	28.05	82.50	1304	Pakhribas	27.05	87.28
601	Jomson	28.78	83.72	1307	Dhankuta	26.98	87.35
605	Baglung	28.27	83.60	1311	Dharan Bazar	26.82	87.28
614	Kushma	28.22	83.70	1312	Haraincha	26.62	87.38
701	Ridi Bazar	27.95	83.43	1314	Terhathum	27.13	87.55
702	Tansen	27.87	83.53	1316	Chatara	26.82	87.17
703	Butwal	27.70	83.47	1325	Dingla	27.37	87.15
705	Bhairahawa Airport	27.52	83.43	1327	Khadbari	27.35	87.20
706	Dumkauli	27.68	84.22	1405	Taplejung	27.35	87.67
708	Parasi	27.53	83.67	1407	Ilam Tea Estate	26.92	87.90
715	Argakhanchi	27.93	83.15	1408	Damak	26.67	87.70
716	Taulihawa	27.55	83.07	1415	Sanischare	26.68	87.97
725	Gulmi	28.07	83.25	1416	Kanyam Tea Estate	26.87	88.07
728	Simari	27.53	83.75	1419	Phidim (Panchthar)	27.15	87.75
802	Khudi Bazar	28.28	84.37	1421	Gaida (Kankai)	26.58	87.90
804	Pokhara Airport	28.22	84.00	1422	Kechana	26.40	88.02

Appendix B

Appendix B: Statistical Comparison Between Simulations and Observations

Scheme	Region 1					Region 2					Region 3							
	RB	ME	MAE	RMSE	SE	CV	RB	ME	MAE	RMSE	SE	CV	RB	ME	MAE	RMSE	SE	CV
ERA-Interim Forcing																		
WSM6_15km	-51.39	-22.61	24.89	32.22	0.59	1.29	0.70	0.09	2.38	2.85	0.99	0.59	-41.96	-5.45	5.83	7.76	0.42	0.43
WSM6_3Km	-91.63	-40.31	40.31	60.54	0.07	0.90	-70.22	-9.13	9.13	11.33	0.66	1.31	-37.78	-4.91	8.34	9.84	0.70	0.67
WSM6_3Km_Con	-71.96	-31.66	33.03	49.99	0.20	0.76	-19.33	-2.51	4.63	5.50	0.57	0.42	-10.27	-1.34	5.65	6.69	0.66	0.44
WDM6_15km	-46.25	-20.35	22.63	33.32	0.50	0.99	35.50	4.61	6.23	8.31	1.55	0.68	-32.43	-4.22	6.46	8.58	0.48	0.42
WDM6_3Km	-37.94	-16.69	26.95	42.89	0.19	0.32	-70.52	-9.17	10.02	13.00	0.37	0.74	-64.98	-8.45	9.31	12.79	0.41	0.70
WDM6_3Km_Con	-16.62	-7.31	22.02	31.38	0.38	0.48	-25.48	-3.31	6.57	8.26	0.51	0.41	-22.79	-2.96	7.55	10.39	0.45	0.35
Lin_15Km	-73.45	-32.35	34.12	51.96	0.16	0.64	2.46	0.32	3.75	4.72	0.66	0.38	-34.95	-4.54	5.19	8.30	0.33	0.30
Lin_3Km	-90.92	-40.00	40.04	61.14	0.03	0.33	-76.26	-9.91	9.91	12.83	0.38	0.95	-58.46	-7.60	9.17	11.15	0.67	0.96
Thompson_15Km	-71.19	-31.32	33.06	52.15	0.14	0.50	24.76	3.22	4.54	7.09	1.11	0.53	-22.69	-2.95	5.07	6.53	0.50	0.39
Thompson_3Km	-94.85	-41.73	41.73	61.98	0.03	0.59	-68.40	-8.89	9.17	11.74	0.45	0.85	-59.45	-7.73	8.30	10.52	0.48	0.71
Morrison_15Km	-80.14	-35.26	35.80	57.85	0.13	0.69	6.03	0.78	6.11	8.77	1.38	0.77	-43.24	-5.62	7.10	9.26	0.40	0.42
Morrison_3Km	-78.52	-34.54	35.96	58.25	0.05	0.26	-84.07	-10.93	10.93	13.07	0.25	0.93	-75.74	-9.84	9.84	12.21	0.34	0.83
Milbrandt_15Km	-74.32	-32.70	34.56	53.32	0.15	0.62	7.04	0.92	3.51	4.35	0.67	0.37	-32.79	-4.26	5.76	7.65	0.33	0.29
Milbrandt_3Km	-63.79	-28.06	31.13	53.30	0.11	0.31	-95.58	-12.42	12.42	14.51	0.08	1.03	-98.87	-12.85	12.85	14.95	0.02	1.12
Goddard_15Km	-90.94	-40.08	40.09	61.90	0.07	0.85	-78.74	-10.23	10.82	13.57	0.55	1.55	-84.30	-10.96	11.61	14.14	0.50	1.87
Goddard_3Km	-74.60	-32.82	38.64	58.95	0.27	1.13	44.63	-5.80	7.25	8.95	0.98	1.04	-91.93	-11.95	11.95	13.76	0.02	1.78
NCEP Initial Condition																		
WSM6_15km	-76.29	-33.56	36.56	54.26	0.13	0.57	4.61	0.60	6.22	7.54	0.29	0.16	-31.06	-4.04	6.81	8.72	0.25	0.21
WSM6_3Km	-95.02	-41.80	41.80	62.24	0.04	0.75	-70.14	-9.12	9.75	12.11	0.43	0.85	-56.36	-7.33	8.99	11.79	0.64	0.88
WDM6_15km	-70.54	-31.03	33.97	52.46	0.16	0.57	6.95	0.90	4.65	5.33	0.73	0.40	-28.01	-3.64	4.88	6.31	0.43	0.36
WDM6_3Km	-51.18	-22.51	29.65	51.90	0.12	0.25	-78.03	-10.14	10.85	13.31	0.35	0.95	-68.88	-8.95	10.63	13.03	0.53	1.01
Lin_15Km	-82.95	-36.49	38.91	57.72	0.12	0.74	-17.78	-2.31	5.69	7.58	0.54	0.39	-37.66	-4.89	6.38	8.88	0.32	0.30
Lin_3Km	-90.47	-39.80	39.93	61.21	0.03	0.32	-88.47	-11.50	11.50	14.15	0.25	1.27	-75.24	-9.78	10.56	13.19	0.46	1.11
Thompson_15Km	-78.42	-34.50	37.26	54.76	0.14	0.69	-10.13	-1.32	4.99	7.13	0.51	0.34	-36.82	-4.78	6.06	8.87	0.29	0.27
Thompson_3Km	-95.87	-42.18	42.18	63.44	0.03	0.87	-82.12	-10.67	10.67	13.23	0.25	0.84	-71.15	-9.25	9.98	12.76	0.48	0.98
Morrison_15Km	-87.62	-38.54	38.54	59.40	0.07	0.63	-41.38	-5.38	5.95	7.46	0.53	0.54	-51.79	-6.73	7.23	9.46	0.37	0.46
Morrison_3Km	-78.52	-34.54	36.32	58.67	0.06	0.28	-87.64	-11.39	11.39	14.00	0.16	0.76	-87.28	-11.34	11.34	14.18	0.24	1.14
Milbrandt_15Km	-88.43	-38.90	39.94	60.17	0.09	0.79	-30.18	-3.92	6.76	9.03	0.67	0.57	-43.97	-5.71	6.21	8.76	0.38	0.40
Milbrandt_3Km	-58.37	-25.68	29.42	53.05	0.13	0.33	-95.82	-12.45	12.45	14.47	0.11	1.61	-96.57	-12.55	12.55	14.57	0.09	1.48
Goddard_15Km	-92.51	-40.70	41.21	62.39	0.09	1.21	-77.04	-10.01	11.81	14.06	0.71	1.85	-87.76	-11.41	12.01	14.46	0.45	2.17
Goddard_3Km	-78.39	-34.48	37.20	57.12	0.18	0.90	-62.52	-8.13	8.13	10.03	0.74	1.18	-93.51	-12.15	12.15	14.11	0.19	1.72

RB = Relative Bias, ME = Mean Error, MAE = Mean Absolute Error, RMSE = Root Mean Square Error, SE = Scale Error, CV = Coefficient of Variance

Chapter 4

Conclusions

The HKH lie in a unique geographical location that is heavily influenced by moist low-level monsoon winds during summer and upper-level westerly winds during winter. These systems create strong north-south and east-west gradients of precipitation, patterns that are further shaped by the extreme topography of the HKH. In particular, south-facing slopes of the central and eastern Himalaya receive large amounts of precipitation during the summer season, while the north-western mountains in the western Himalaya receive greater amounts of precipitation during the winter. Thus, strong topographic variations in the HKH produce strong spatial and temporal variations in the intensity of precipitation, making weather forecasting in the region a challenging job.

In this thesis, I determined the influence of upper-atmospheric blocks formed over the Ural-Siberian region on Himalayan weather using a combination of reanalysis data and MAM simulations. In addition, I evaluated the sensitivity of different cloud microphysics schemes available within the WRF model to simulate an extreme flood-producing precipitation event over the central Himalaya, and determined the best microphysics scheme for use over Nepal. Key findings from this thesis are presented in the following sections.

4.1 Key findings and future research

4.1.1 Coarse resolution simulations with WSM6 and WDM6 microphysics schemes perform better than high resolution simulations

Sensitivity analyses of different cloud microphysics schemes were performed over three different regions based on the altitudinal gradient of the Nepal Himalaya. Overall, the WSM6 scheme at 15 km horizontal resolution performs the best (i.e. it has the smallest RMSE) amongst the different microphysics schemes used in the experiments, followed by the WDM6 scheme. The performance of high resolution simulations (3 km), however,

is poorer than the coarse resolution simulations and none of the schemes realistically simulate the precipitation intensity. A commonly applied rule of thumb in WRF is that convective parameterization scheme be turned off at resolutions below 10 km, with the assumption being that at these resolutions convection is explicitly resolved by the model. To evaluate if our observed discrepancy is a result of turning off the cumulus scheme at 3 km resolution, two additional experiments using WSM6 and WDM6 schemes with cumulus schemes turned on are performed and resulted in the following fundamental conclusion from this thesis.

4.1.2 Cumulus parametrization is essential for highly convective systems over the Himalaya

Previous studies suggest that cumulus parametrization is not necessary for numerical simulations below 10 km horizontal resolution because the numerical models are capable of resolving convection explicitly at grid scales finer than 10 km. However, this research shows that cumulus parametrization is essential at resolutions below 10 km to realistically simulate the precipitation intensity in highly convective systems over steep topography. Our case study is an extreme rainfall event over southern Nepal during the monsoon of 2017. The upper-air profile obtained from the sounding station at Patna, India indicate the event as highly convective (early morning CAPE > 1500 J/Kg). WRF simulations at 3 km horizontal resolution using various cloud microphysics schemes with the cumulus scheme off grossly underestimate the precipitation intensity. Identical simulations using the WDM6 microphysics scheme and keeping the cumulus scheme on shows dramatic improvement (with minimum RMSE) in the precipitation hindcast.

The conclusion presented here, however, is based only on a single case; it will be interesting to see if the conclusion of this study is valid for other cases of highly convection systems over the Nepal Himalaya as well as other geographical locations that exhibit steep topography. Furthermore, this conclusion from the thesis highlights the importance of improving the physical parametrizations available within the MAMs for the Himalayan region.

4.1.3 Ural-Siberian blocks generate Himalayan climate anomalies

Ural-Siberian blocks are associated with anomalous weather patterns over the Himalaya. The typical quasi-stationary blocking pattern that develops in the upper-troposphere over the Ural-Siberian region consists of a high-pressure centre lying over the Ural-Siberian region and low-pressure trough/troughs lying over the subtropics forming either an omega or a dipole structure. In case of an block the low-pressure component at its trailing edge lies in the vicinity of the western Himalaya. When the low-pressure component of the block gets terrain locked over the western Himalayan notch (WHN), descent and ascent of the ageostrophic winds creates

high pressure over the Arabian Peninsula and the western Arabian Sea and low pressure along the foothills of the western Himalaya, respectively. This flow pattern advects moisture from the Arabian sea to the WHN producing anomalously high precipitation.

On the other hand, if the trough shifts south-eastward over central India, surface pressure over the western coast of India and the southern part of the Arabian sea increases, while low pressures form along the foothills of the central Himalaya. This anomalous pattern produces strong precipitation over the central and eastern Himalaya. Thus, this study implies that Ural-Siberian blocks are important perturbations of Himalayan climate and strongly contribute to precipitation anomalies and snow accumulation over Himalayan glaciers. Any changes in the frequency and intensity of blocking events under future climate change scenarios and their impact on anomalous Himalayan weather and snow accumulation is an important topic for future research.

4.1.4 Differential temperature advection during blocking events determines the type of precipitation at the surface

The spatial patterns of anomalous pressures associated with Ural-Siberian atmospheric blocks produce differential temperature advection. In particular, cold midlatitude air is present on the northern side of the block and warm subtropical air is present on the southern side of the block. Southward advection of the colder air lowers the freezing level, while northward advection of warmer air raises the freezing level. Hence, regions where anomalously cold temperature advection lowers the freezing level will get snowfall at lower elevations, while region where anomalously warm temperature advection raises the freezing level will get rainfall at higher elevations. The anomalous change in type of precipitation as a function of altitude may be important for glacier mass balance at high elevations, and is another important topic for future research.

4.2 Thesis Summary

This thesis highlights the importance of competent parameterizations in the numerical weather forecasting model for the simulation of climate and extreme events over the Himalaya. Also highlighted is the importance of Ural-Siberian blocks in the generation of anomalous Himalayan weather. Understanding these anomalies today and in future climate scenario requires a robust numerical model and a resourceful weather forecasting network. The overall findings of this thesis are summarized in following key points.

- Cumulus parametrization should be retained in MAM simulations over steep topography, even at high spatial resolution.

- Ural-Siberian blocks are important generators of anomalous weather conditions over the HKH and could therefore be useful indicators for forecasters.
- Differential temperature advection over the HKH results in anomalies of precipitation type as a function of altitude, and could be an important factor determining future snow accumulation over Himalayan glaciers.

Bibliography

- Andermann, C., Bonnet, S., and Gloaguen, R. (2011). Evaluation of precipitation data sets along the Himalayan front. *Geochemistry, Geophysics, Geosystems*, 12(7).
- Annamalai, H., Hamilton, K., and Sperber, K. R. (2007). The south Asian summer monsoon and its relationship with ENSO in the IPCC AR4 simulations. *Journal of Climate*, 20(6):1071–1092.
- Bader, M. J., Forbes, G. S., Grant, J. R., E., L. R. B., and Waters, J. (1995). Images in weather forecasting. Technical report, Cambridge University Press.
- Barriopedro, D., García-Herrera, R., Lupo, A. R., and Hernández, E. (2006). A climatology of Northern Hemisphere blocking. *Journal of Climate*, 19(6):1042–1063.
- Barros, A. P., Joshi, M., Putkonen, J., and Burbank, D. W. (2000). A study of 1999 monsoon rainfall in a mountainous region in Central Nepal using TRMM products and rain gauge observations. *Geophysical Research Letters*, 27(22):3683–3686.
- Barros, A. P. and Lang, T. J. (2003). Monitoring the monsoon in the Himalayas: Observations in central Nepal, June 2001. *Monthly Weather Review*, 131(7):1408–1427.
- Bhandari, D., Uprety, M., Ghimire, G., Kumal, B., Pokharel, L., and Khadka, P. (2018). Nepal flood 2017: Wake up call for effective preparedness and response. *Rugby, UK: Practical Action*.
- Bharati, L., Gurung, P., Jayakody, P., Smakhtin, V., and Bhattarai, U. (2014). The projected impact of climate change on water availability and development in the Koshi basin, Nepal. *Mountain Research and Development*, 34(2):118 – 130 – 13.
- Bhatt, B. C. and Nakamura, K. (2005). Characteristics of monsoon rainfall around the Himalayas revealed by TRMM precipitation radar. *Monthly Weather Review*, 133(1):149–165.
- Bhomia, S., Kumar, P., and Kishtawal, C. M. (2019). Evaluation of the weather research and forecasting model forecasts for Indian summer monsoon rainfall of 2014 using ground based observations. *Asia-Pacific Journal of Atmospheric Sciences*.
- Bolch, T., Kulkarni, A., Kaab, A., Huggel, C., Paul, F., Cogley, J. G., Frey, H., Kargel, J. S., Fujita, K., Scheel, M., Bajracharya, S., and Stoffel, M. (2012). The state and fate of Himalayan glaciers. *Science*, 336(6079):310–314.
- Bonekamp, P. N. J., Collier, E., and Immerzeel, W. W. (2018). The impact of spatial resolution, landuse and spin-up time on resolving spatial precipitation patterns in the Himalayas. *Journal of Hydrometeorology*.

- Bookhagen, B. and Burbank, D. W. (2010). Toward a complete Himalayan hydrological budget: Spatiotemporal distribution of snowmelt and rainfall and their impact on river discharge. *Journal of Geophysical Research: Earth Surface*, 115(F3).
- Bracci, A., Cristofanelli, P., Sprenger, M., Bonaf, U., Calzolari, F., Duchi, R., Laj, P., Marinoni, A., Roccatò, F., Vuillermoz, E., and Bonasoni, P. (2012). Transport of stratospheric air masses to the Nepal Climate Observatory Pyramid (Himalaya; 5079 m msl): A synoptic-scale investigation. *Journal of Applied Meteorology and Climatology*, 51(8):1489–1507.
- Brunner, L., Hegerl, G. C., and Steiner, A. K. (2017). Connecting atmospheric blocking to European temperature extremes in spring. *Journal of Climate*, 30(2):585–594.
- Cannon, F., Carvalho, L. M., Jones, C., and Bookhagen, B. (2014). Multi-annual variations in winter westerly disturbance activity affecting the Himalaya. *Climate Dynamics*, 44(1-2):441–455.
- Carrera, M. L., Higgins, R. W., and Kousky, V. E. (2004). Downstream weather impacts associated with atmospheric blocking over the Northeast Pacific. *Journal of Climate*, 17(24):4823–4839.
- Casola, J. H. and Wallace, J. M. (2007). Identifying weather regimes in the wintertime 500-hPa geopotential height field for the Pacific-North American sector using a limited-contour clustering technique. *Journal of Applied Meteorology and Climatology*, 46(10):1619–1630.
- Chawla, I., Osuri, K. K., Mujumdar, P. P., and Niyogi, D. (2018). Assessment of the Weather Research and Forecasting (WRF) model for simulation of extreme rainfall events in the upper Ganga Basin. *Hydrology and Earth System Sciences*, 22(2):1095–1117.
- Chen, S.-H. and Sun, W.-Y. (2002). A one-dimensional time dependent cloud model. *Journal of the Meteorological Society of Japan. Ser. II*, 80(1):99–118.
- Cheung, H. N., Zhou, W., Mok, H. Y., and Wu, M. C. (2012). Relationship between Ural-Siberian Blocking and the East Asian winter monsoon in relation to the Arctic Oscillation and the El Niño-Southern Oscillation. *Journal of Climate*, 25(12):4242–4257.
- Cheung, H. N., Zhou, W., Mok, H. Y., Wu, M. C., and Shao, Y. (2013a). Revisiting the climatology of atmospheric blocking in the Northern Hemisphere. *Advances in Atmospheric Sciences*, 30(2):397–410.
- Cheung, H. N., Zhou, W., Shao, Y., Chen, W., Mok, H. Y., and Wu, M. C. (2013b). Observational climatology and characteristics of wintertime atmospheric blocking over Ural-Siberia. *Climate Dynamics*, 41(1):63–79.

- Choudhary, A. and Dimri, A. P. (2018). Assessment of CORDEX-South Asia experiments for monsoonal precipitation over Himalayan region for future climate. *Climate Dynamics*, 50(7):3009–3030.
- Collier, E. and Immerzeel, W. W. (2015). High-resolution modeling of atmospheric dynamics in the Nepalese Himalaya. *Journal of Geophysical Research: Atmospheres*, 120(19):9882–9896.
- Collier, E., Mölg, T., Maussion, F., Scherer, D., Mayer, C., and Bush, A. B. G. (2013). High-resolution interactive modelling of the mountain glacier-atmosphere interface: an application over the Karakoram. *The Cryosphere*, 7(3):779–795.
- Collier, E., Nicholson, L. I., Brock, B. W., Maussion, F., Essery, R., and Bush, A. B. G. (2014). Representing moisture fluxes and phase changes in glacier debris cover using a reservoir approach. *The Cryosphere*, pages 1429–1444.
- Dee, D. P., Uppala, S. M., Simmons, A. J., Berrisford, P., Poli, P., Kobayashi, S., Andrae, U., Balmaseda, M. A., Balsamo, G., Bauer, P., Bechtold, P., Beljaars, A. C. M., van de Berg, L., Bidlot, J., Bormann, N., Delsol, C., Dragani, R., Fuentes, M., Geer, A. J., Haimberger, L., Healy, S. B., Hersbach, H., Hlm, E. V., Isaksen, L., Kllberg, P., Kllner, M., Matricardi, M., McNally, A. P., Monge-Sanz, B. M., Morcrette, J.-J., Park, B.-K., Peubey, C., de Rosnay, P., Tavolato, C., Thpaut, J.-N., and Vitart, F. (2011). The ERA-Interim reanalysis: configuration and performance of the data assimilation system. *Quarterly Journal of the Royal Meteorological Society*, 137(656):553–597.
- Deng, A. and Stauffer, D. R. (2006). On improving 4-km mesoscale model simulations. *Journal of Applied Meteorology and Climatology*, 45(3):361–381.
- Dimri, A. P. and Chevuturi, A. (2014). Model sensitivity analysis study for western disturbances over the Himalayas. *Meteorology and Atmospheric Physics*, 123(3-4):155–180.
- Dimri, A. P. and Mohanty, U. C. (2009). Simulation of mesoscale features associated with intense western disturbances over Western Himalayas. *Meteorological Applications*, 16(3):289–308.
- Dimri, A. P. and Niyogi, D. (2013). Regional climate model application at subgrid scale on Indian winter monsoon over the western Himalayas. *International Journal of Climatology*, 33(9):2185–2205.
- Dimri, A. P., Niyogi, D., Barros, A. P., Ridley, J., Mohanty, U. C., Yasunari, T., and Sikka, D. R. (2015). Western disturbances: A review. *Reviews of Geophysics*, 53(2):225–246.
- Dudhia, J., HONG, S.-Y., and Lim, K.-S. (2008). A new method for representing mixed-phase particle fall speeds in bulk microphysics parameterizations. *Journal of the Meteorological Society of Japan. Ser. II*, 86A:33–44.

- Fan, F., Dong, X., Fang, X., Xue, F., Zheng, F., and Zhu, J. (2017). Revisiting the relationship between the South Asian summer monsoon drought and El Niño warming pattern. *Atmospheric Science Letters*, 18(4):175–182.
- Guhathakurta, P., Sreejith, O. P., and Menon, P. A. (2011). Impact of climate change on extreme rainfall events and flood risk in India. *Journal of Earth System Science*, 120(3):359.
- Hasson, S., Lucarini, V., and Pascale, S. (2013). Hydrological cycle over south and southeast asian river basins as simulated by PCMDI/CMIP3 experiments. *Earth System Dynamics*, 4(2):199–217.
- Hasson, S., Pascale, S., Lucarini, V., and Bhner, J. (2016). Seasonal cycle of precipitation over major river basins in South and Southeast Asia: A review of the CMIP5 climate models data for present climate and future climate projections. *Atmospheric Research*, 180:42 – 63.
- Holton, J. R. (1992). *An Introduction to Dynamical Meteorology*. Academic Press.
- Hong, S.-Y., Dudhia, J., and Chen, S.-H. (2004). A revised approach to ice microphysical processes for the bulk parameterization of clouds and precipitation. *Monthly Weather Review*, 132(1):103–120.
- Houze Jr., R. A., Wilton, D. C., and Smull, B. F. (2007). Monsoon convection in the Himalayan region as seen by the TRMM precipitation radar. *Quarterly Journal of the Royal Meteorological Society*, 133(627):1389–1411.
- Huffman, G. J., Adler, R. F., Bolvin, D. T., and Nelkin, E. J. (2010). *The TRMM Multi-Satellite Precipitation Analysis (TMPA)*, pages 3–22. Springer Netherlands, Dordrecht.
- Huffman, G., Bolvin, D., Braithwaite, D., Hus, K., Joyce, R., and Xie, P. (2014). Integrated multi-satellite retrievals for GPM (IMERG), version 4.4. *NASA's Precipitation Processing Center*.
- Hunt, K. M. R., Turner, A. G., Inness, P. M., Parker, D. E., and Levine, R. C. (2016). On the structure and dynamics of Indian monsoon depressions. *Monthly Weather Review*, 144(9):3391–3416.
- Hunt, K. M. R., Turner, A. G., and Shaffrey, L. C. (2018). Extreme daily rainfall in Pakistan and North India: Scale interactions, mechanisms, and precursors. *Monthly Weather Review*, 146(4):1005–1022.
- Ichiyanagi, K., Yamanaka, M. D., Muraji, Y., and Vaidya, B. K. (2007). Precipitation in Nepal between 1987 and 1996. *International Journal of Climatology*, 27(13):1753–1762.
- Immerzeel, W. W., Pellicciotti, F., and Bierkens, M. F. P. (2013). Rising river flows throughout the twenty-first century in two Himalayan glacierized watersheds. *Nature Geoscience*, 6(742).
- IPCC (2012). Managing the risks of extreme events and disasters to advance climate change adaptation. a special report of working group I and II of the Intergovernmental Panel on Climate Change. Technical report, IPCC.

- Jang, Y. and Straus, D. M. (2012). The Indian monsoon circulation response to El niño diabatic heating. *Journal of Climate*, 25(21):7487–7508.
- Jiménez, P. A., Dudhia, J., Gonzalez-Rouco, J. F., Navarro, J., Montvez, J. P., and Garca-Bustamante, E. (2012). A revised scheme for the WRF surface layer formulation. *Monthly Weather Review*, 140(3):898–918.
- Joshi, S. and Kar, S. C. (2018). Mechanism of ENSO influence on the South Asian monsoon rainfall in global model simulations. *Theoretical and Applied Climatology*, 131(3):1449–1464.
- Kain, J. S. (2004). The KainFritsch convective parameterization: An update. *Journal of Applied Meteorology*, 43(1):170–181.
- Kansakar, S. R., Hannah, D. M., Gerrard, J., and Rees, G. (2004). Spatial pattern in the precipitation regime in Nepal. *International Journal of Climatology*, 24(13):1645–1659.
- Karki, R., Ul Hasson, S., Gerlitz, L., Schickhoff, U., Scholten, T., and Bøhner, J. (2017). Quantifying the added value of convection-permitting climate simulations in complex terrain: A systematic evaluation of WRF over the Himalayas. *Earth System Dynamics*, 8(3):507–528.
- Karki, R., ul Hasson, S., Gerlitz, L., Talchabhadel, R., Schenk, E., Schickhoff, U., Scholten, T., and Böhner, J. (2018). WRF-based simulation of an extreme precipitation event over the Central Himalayas: Atmospheric mechanisms and their representation by microphysics parameterization schemes. *Atmospheric Research*, 214(July):21–35.
- Kotroni, V. and Lagouvardos, K. (2004). Evaluation of MM5 high-resolution real-time forecasts over the urban area of Athens, Greece. *Journal of Applied Meteorology*, 43(11):1666–1678.
- Lang, S. E., Tao, W.-K., Chern, J.-D., Wu, D., and Li, X. (2014). Benefits of a fourth ice class in the simulated radar reflectivities of convective systems using a bulk microphysics scheme. *Journal of the Atmospheric Sciences*, 71(10):3583–3612.
- Lang, T. J. and Barros, A. P. (2002). An investigation of the onsets of the 1999 and 2000 monsoons in Central Nepal. *Monthly Weather Review*, 130(5):1299–1316.
- LANG, T. J. and BARROS, A. P. (2004). Winter Storms in the Central Himalayas. *Journal of the Meteorological Society of Japan*, 82(3):829–844.
- Lau, W. K. M. and Kim, K.-M. (2012). The 2010 Pakistan flood and Russian heat wave: Teleconnection of hydrometeorological extremes. *Journal of Hydrometeorology*, 13(1):392–403.

- Lejenäs, H. and Økland, H. (1983). Characteristics of northern hemisphere blocking as determined from a long time series of observational data. *Tellus A*, 35A(5):350–362.
- Lim, K.-S. S. and Hong, S.-Y. (2010). Development of an effective double-moment cloud microphysics scheme with prognostic cloud condensation nuclei (CCN) for weather and climate models. *Monthly Weather Review*, 138(5):1587–1612.
- Lin, Y.-L., Farley, R. D., and Orville, H. D. (1983). Bulk parameterization of the snow field in a cloud model. *Journal of Climate and Applied Meteorology*, 22(6):1065–1092.
- Liu, L., Ma, Y., Menenti, M., Zhang, X., and Ma, W. (2019). Evaluation of WRF modeling in relation to different land surface schemes and initial and boundary conditions: A snow event simulation over the Tibetan plateau. *Journal of Geophysical Research: Atmospheres*, 124(1):209–226.
- Maharjan, S., Mool, P., Lizong, W., Xiao, G., Shrestha, F., Shrestha, R., Khanal, N., Bajracharya, S., Joshi, S., Shai, S., and Baral, P. (2018). The status of glacial lakes in the Hindu Kush Himalaya. Technical report, ICIMOD, ICIMOD, Kathmandu.
- Maussion, F., Scherer, D., Finkelnburg, R., Richters, J., Yang, W., and Yao, T. (2011). WRF simulation of a precipitation event over the Tibetan Plateau, China - An assessment using remote sensing and ground observations. *Hydrology and Earth System Sciences*, 15(6):1795–1817.
- Medina, S., Houze, R. A., Kumar, A., and Niyogi, D. (2010). Summer monsoon convection in the Himalayan region: Terrain and land cover effects. *Quarterly Journal of the Royal Meteorological Society*, 136(648):593–616.
- Milbrandt, J. A. and Yau, M. K. (2005). A multimoment bulk microphysics parameterization. part I: Analysis of the role of the spectral shape parameter. *Journal of the Atmospheric Sciences*, 62(9):3051–3064.
- MoHA (2018). *Nepal Disaster Report, 2017: The Road to Sendai*. Kathmandu: Government of Nepal.
- Molinari, J. and Dudek, M. (1992). Parameterization of convective precipitation in mesoscale numerical models: A critical review. *Monthly Weather Review*, 120(2):326–344.
- Morrison, H. and Gettelman, A. (2008). A new two-moment bulk stratiform cloud microphysics scheme in the community atmosphere model, version 3 (cam3). part I: Description and numerical tests. *Journal of Climate*, 21(15):3642–3659.
- Mishra, V. (2015). Climatic uncertainty in Himalayan water towers. *Journal of Geophysical Research: Atmospheres*, 120(7):2689–2705.

- Mooley, D. A. and Parthasarathy, B. (1983). Indian summer monsoon and El Niño. *pure and applied geophysics*, 121(2):339–352.
- Mujumdar, M., Preethi, B., Sabin, T. P., Ashok, K., Saeed, S., Pai, D. S., and Krishnan, R. (2012). The Asian summer monsoon response to the La Niña event of 2010. *Meteorological Applications*, 19(2):216–225.
- Murali Krishna, U. V., Das, S. K., Deshpande, S. M., Doiphode, S. L., and Pandithurai, G. (2017). The assessment of global precipitation measurement estimates over the Indian subcontinent. *Earth and Space Science*, 4(8):540–553.
- Nakanishi, M. and Niino, H. (2006). An improved Mellor - Yamada level-3 model: Its numerical stability and application to a regional prediction of advection fog. *Boundary-Layer Meteorology*, 119(2):397–407.
- Nakanishi, M. and Niino, H. (2009). Development of an improved turbulence closure model for the atmospheric boundary layer. *Journal of the Meteorological Society of Japan. Ser. II*, 87(5):895–912.
- Niu, G.-Y., Yang, Z.-L., Mitchell, K. E., Chen, F., Ek, M. B., Barlage, M., Kumar, A., Manning, K., Niyogi, D., Rosero, E., Tewari, M., and Xia, Y. (2011). The community NOAA land surface model with multiparameterization options (NOAH-MP): 1. model description and evaluation with local-scale measurements. *Journal of Geophysical Research: Atmospheres*, 116(D12).
- Norris, J., Carvalho, L. M., Jones, C., and Cannon, F. (2015). WRF simulations of two extreme snowfall events associated with contrasting extratropical cyclones over the western and central Himalaya. *Journal of Geophysical Research*, 120(8):3114–3138.
- Norris, J., Carvalho, L. M., Jones, C., and Cannon, F. (2019). Deciphering the contrasting climatic trends between the central Himalaya and Karakoram with 36 years of WRF simulations. *Climate Dynamics*, 52(1-2):159–180.
- NPC (2017c). *Nepal Flood 2017: Post flood recovery needs assessment*. Kathmandu: National Planning Commission (NPC), Government of Nepal.
- Ojha, N., Pozzer, A., Akritidis, D., and Lelieveld, J. (2017). Secondary ozone peaks in the troposphere over the Himalayas. *Atmospheric Chemistry and Physics*, 17(11):6743–6757.
- Orr, A., Listowski, C., Couttet, M., Collier, E., Immerzeel, W., Deb, P., and Bannister, D. (2017). Sensitivity of simulated summer monsoonal precipitation in Langtang Valley, Himalaya, to cloud microphysics schemes in WRF. *Journal of Geophysical Research: Atmospheres*, 122(12):6298–6318.

- Park, H. S., Chiang, J. C., and Bordoni, S. (2012). The mechanical impact of the Tibetan Plateau on the seasonal evolution of the South Asian monsoon. *Journal of Climate*, 25(7):2394–2407.
- Park, Y.-J. and An, J.-B. (2014). Characteristics of atmospheric circulation over East Asia associated with summer blocking. *Journal of Geophysical Research Atmospheres*, 119(2):726–738.
- Patil, R. and Pradeep Kumar, P. (2016). WRF model sensitivity for simulating intense western disturbances over North West India. *Modeling Earth Systems and Environment*, 2(2):82.
- Pelly, J. L. and Hoskins, B. J. (2003). A New Perspective on Blocking. *Journal of the Atmospheric Sciences*, 60(5):743–755.
- Pokhrel, D., Bhandari, B., and Viraraghavan, T. (2009). Natural hazards and environmental implications in Nepal. *Disaster Prevention and Management: An International Journal*, 18(5):478–489.
- Pook, M. J., Risbey, J. S., McIntosh, P. C., Ummenhofer, C. C., Marshall, A. G., and Meyers, G. A. (2013). The Seasonal Cycle of Blocking and Associated Physical Mechanisms in the Australian Region and Relationship with Rainfall. *American Meteorological Society*, 141(12):4534–4553.
- Postel, G. A. and Hitchman, M. H. (1999). A climatology of Rossby wave breaking along the subtropical tropopause. *Journal of the Atmospheric Sciences*, 56(3):359–373.
- Prasad, V. S. and Hayashi, T. (2005). Onset and withdrawal of Indian summer monsoon. *Geophysical Research Letters*, 32(L20715).
- Rajeevan, M., De, U. S., and Prasad, R. K. (2000). Decadal variation of sea surface temperatures, cloudiness and monsoon depression in the North Indian ocean. *Current Science*, 9:283–285.
- Regmi, R. P., Kitada, T., Dudhia, J., and Maharjan, S. (2017). Large-scale gravity current over the middle hills of the Nepal Himalaya: Implications for aircraft accidents. *Journal of Applied Meteorology and Climatology*, 56(2):371–390.
- Ren, Y.-Y., Ren, G.-Y., Sun, X.-B., Shrestha, A. B., You, Q.-L., Zhan, Y.-J., Rajbhandari, R., Zhang, P.-F., and Wen, K.-M. (2017). Observed changes in surface air temperature and precipitation in the Hindu Kush Himalayan region over the last 100-plus years. *Advances in Climate Change Research*, 8(3):148 – 156. Including special issue on climate change in the Hindu Kush Himalaya.
- Revadekar, J. V., Hameed, S., Collins, D., Manton, M., Sheikh, M., Borgaonkar, H. P., Kothawale, D. R., Adnan, M., Ahmed, A. U., Ashraf, J., Baidya, S., Islam, N., Jayasinghearachchi, D., Manzoor, N., Premalal, K. H.

- M. S., and Shrestha, M. L. (2013). Impact of altitude and latitude on changes in temperature extremes over South Asia during 1971-2000. *International Journal of Climatology*, 33(1):199–209.
- Rex, D. F. (1950). Blocking action in the middle troposphere and its effect upon regional climate. *Tellus*, 2(3):196–211.
- Romatschke, U. and Houze, R. A. (2011). Characteristics of precipitating convective systems in the South Asian monsoon. *Journal of Hydrometeorology*, 12(1):3–26.
- Rutledge, S. A. and Hobbs, P. V. (1984). The mesoscale and microscale structure and organization of clouds and precipitation in midlatitude cyclones. XII: A diagnostic modeling study of precipitation development in narrow cold-frontal rainbands. *Journal of the Atmospheric Sciences*, 41(20):2949–2972.
- S.-Y., H. and J.-O., J. (2006). The WRF single-moment 6-class microphysics scheme (WSM6). *J. Korean Meteor. Soc.*, 42:129–151.
- Sato, T. and Kimura, F. (2007). How does the Tibetan Plateau affect the transition of Indian monsoon rainfall? *Monthly Weather Review*, 135(5):2006–2015.
- Shea, J. M., Immerzeel, W. W., Wagnon, P., Vincent, C., and Bajracharya, S. (2015). Modelling glacier change in the Everest region, Nepal Himalaya. *Cryosphere*, 9(3):1105–1128.
- Shrestha, D., Singh, P., and Nakamura, K. (2012). Spatiotemporal variation of rainfall over the Central Himalayan region revealed by TRMM precipitation radar. *Journal of Geophysical Research: Atmospheres*, 117(D22).
- Shrestha, P., Dimri, A. P., Schomburg, A., and Simmer, C. (2015). Improved understanding of an extreme rainfall event at the Himalayan foothills: a case study using COSMO. *Tellus A: Dynamic Meteorology and Oceanography*, 67(1):26031.
- Shrestha, M. L. (2000). Interannual variation of summer monsoon rainfall over Nepal and its relation to Southern Oscillation Index. *Meteorology and Atmospheric Physics*, 75(1-2):21–28.
- Shrestha, R. K., Gallagher, M. W., and Connolly, P. J. (2016). Diurnal and seasonal variations of meteorology and aerosol concentrations in the foothills of the Nepal Himalayas (Nagarkot: 1,900 m asl). *Asia-Pacific Journal of Atmospheric Sciences*, 52(1):63–75.
- Singh, D., Jain, S. K., and Gupta, R. D. (2015). Trend in observed and projected maximum and minimum temperature over N-W Himalayan basin. *Journal of Mountain Science*, 12(2):417–433.

- Singh, D., Tsiang, M., Rajaratnam, B., and Diffenbaugh, N. S. (2014). Observed changes in extreme wet and dry spells during the South Asian summer monsoon season. *Nature Climate Change*, 4:456–461.
- Stigter, E. E., Litt, M., Steiner, J. F., Bonekamp, P. N. J., Shea, J. M., Bierkens, M. F. P., and Immerzeel, W. W. (2018). The Importance of Snow Sublimation on a Himalayan Glacier. *Frontiers in Earth Science*, 6(August):1–16.
- Takaya, K. and Nakamura, H. (2005). Geographical dependence of upper-level blocking formation associated with intraseasonal amplification of the Siberian high. *Journal of the atmospheric sciences*, pages 4441–4449.
- Tao, W.-K., Wu, D., Lang, S., Chern, J.-D., Peters-Lidard, C., Fridlind, A., and Matsui, T. (2016). High-resolution nu-WRF simulations of a deep convective-precipitation system during MC3E: Further improvements and comparisons between Goddard microphysics schemes and observations. *Journal of Geophysical Research: Atmospheres*, 121(3):1278–1305.
- Thompson, G., Field, P. R., Rasmussen, R. M., and Hall, W. D. (2008). Explicit forecasts of winter precipitation using an improved bulk microphysics scheme. part II: Implementation of a new snow parameterization. *Monthly Weather Review*, 136(12):5095–5115.
- Thompson, S., Benn, D. I., Mertes, J., and Luckman, A. (2016). Stagnation and mass loss on a Himalayan debris-covered glacier: processes, patterns and rates. *Journal of Glaciology*, 62(233):467485.
- Tibaldi, S. and Molteni, F. (1990). On the operational predictability of blocking. *Tellus A*, 42(3):343–365.
- Tiwari, S., Kar, S. C., and Bhatla, R. (2018). Dynamic downscaling over western Himalayas: Impact of cloud microphysics schemes. *Atmospheric Research*, 201(October 2017):1–16.
- Tyrlis, E. and Hoskins, B. J. (2008). The Morphology of Northern Hemisphere Blocking. *Journal of the Atmospheric Sciences*, 65(5):1653–1665.
- van, Vuuren, D. P., Edmonds, J., Kainuma, M., Riahi, K., Thomson, A., Hibbard, K., Hurtt, G. C., Kram, T., Krey, V., Lamarque, J.-F., Masui, T., Meinshausen, M., Nakicenovic, N., Smith, S. J., and Rose, S. K. (2011). The Representative Concentration Pathways: an overview. *Climatic Change*, 109(1):5.
- Vellore, R. K., Kaplan, M. L., Krishnan, R., Lewis, J. M., Sabade, S., Deshpande, N., Singh, B. B., Madhura, R. K., and Rama Rao, M. V. (2016). Monsoon-extratropical circulation interactions in Himalayan extreme rainfall. *Climate Dynamics*, 46(11-12):3517–3546.

- Vellore, R. K., Krishnan, R., Pendharkar, J., Choudhury, A. D., and Sabin, T. P. (2014). On the anomalous precipitation enhancement over the Himalayan foothills during monsoon breaks. *Climate Dynamics*, 43(7-8):2009–2031.
- Vincent, C., Wagnon, P., Shea, J. M., Immerzeel, W. W., Kraaijenbrink, P., Shrestha, D., Soruco, A., Arnaud, Y., Brun, F., Berthier, E., and Sherpa, S. F. (2016). Reduced melt on debris-covered glaciers: Investigations from Changri Nup glacier, Nepal. *Cryosphere*, 10(4):1845–1858.
- Virts, K. S. and Houze, R. A. (2016). Seasonal and Intraseasonal Variability of Mesoscale Convective Systems over the South Asian Monsoon Region. *Journal of the Atmospheric Sciences*, 73(12):4753–4774.
- Wester, P., A., M., A., M., and A. B., S., editors (2019). *The Hindu kush Himalaya Assessment - Mountains, Climate Change, Sustainability, and People*. Springer Nature, Switzerland AG, Cham.
- Weisman, M. L., Skamarock, W. C., and Klemp, J. B. (1997). The resolution dependence of explicitly modeled convective systems. *Monthly Weather Review*, 125(4):527–548.
- Xie, A., Ren, J., Qin, X., and Kang, S. (2007). Reliability of NCEP/NCAR reanalysis data in the Himalayas/Tibetan Plateau. *Journal of Geographical Sciences*, 17(4):421–430.
- Yang, Z.-L., Niu, G.-Y., Mitchell, K. E., Chen, F., Ek, M. B., Barlage, M., Longuevergne, L., Manning, K., Niyogi, D., Tewari, M., and Xia, Y. (2011). The community NOAA land surface model with multiparameterization options (NOAH-MP): 2. evaluation over global river basins. *Journal of Geophysical Research: Atmospheres*, 116(D12).
- Yatagai, A., Kamiguchi, K., Arakawa, O., Hamada, A., Yasutomi, N., and Kitoh, A. (2012). Aphrodite: Constructing a long-term daily gridded precipitation dataset for Asia based on a dense network of rain gauges. *Bulletin of the American Meteorological Society*, 93(9):1401–1415.
- Zhou, W., Chan, J. C. L., Chen, W., Ling, J., Pinto, J. G., and Shao, Y. (2009). Synoptic-Scale Controls of Persistent Low Temperature and Icy Weather over Southern China in January 2008. *Monthly Weather Review*, 137(11):3978–3991.